Università degli Studi di Genova - Istituto Italiano di Tecnologia

Doctorate School in Sciences and Technologies of Chemistry and Materials
Curriculum: Nanochemistry - XXXIV cycle

Metal oxide nanocrystals for light-driven energy storage

Michele Ghini

Supervisor IIT:

Dr. Ilka Kriegel

Prof. Liberato Manna

Supervisor UNIGE:

Prof. Francesco Buatier de Mongeot

A.A. 2021/2022

Abstract

In a world struggling to face the disruptive consequences of global warming, developing new energy conversion and storage solutions is of fundamental importance. This PhD thesis focuses on emerging heterostructures based on Indium Tin Oxide nanocrystals (ITO NCs) and two-dimensional Transition Metal Dichalcogenides (2D TMDs) for innovative light-driven optoelectronic nanodevices and energy storage solutions, combining the harvesting, conversion and storage aspects into a unique hybrid nanomaterial. Doped Metal Oxide (MO) NCs are attracting growing interest as nano-supercapacitors due to their ability to store extra charges in their electronic structure with record-high values of capacitance. Remarkably, these materials can be charged with light (*i.e.*, photodoping), a process at the core of this project and so far not understood electronically. Here, the fundamental features involved in the charge accumulation process are investigated and the physics of photodoping explained. Complete control over energetic band bending and depletion layer engineering is demonstrated, exposing the key role of electronically depleted layers in core-shell NCs. Light-induced depletion layer modulation and band bending is the main mechanism responsible for the storage of extra charges in doped MO supercapacitors. Moreover, multi-electron transfer reversible reactions were observed in photodoped NCs when exposed to a frequently used electron acceptor. The coupling between ITO NCs and 2D TMDs allowed the implementation of a novel all-optical localized charge injection scheme for the manipulation of unperturbed 2D materials. Hybrid 0D-2D heterostructures proved all-solid-state photodoping possible, with promising charging dynamics and capacitance values. Theoretical modeling tools were developed, leading to the optimization of the charge storage capacity of 0D NCs. This work is of particular interest for the fabrication of the next-generation of nanostructured light-driven supercapacitors.

List of publications

This PhD thesis is based on the following publications:

Light-Driven Permanent Charge Separation across a Hybrid Zero-Dimensional/Two-Dimensional Interface

Kriegel, I., Ghini, M., Bellani, S., Zhang, K., Jansons, A. W., Crockett,B. M., Koskela, K. M., Barnard, E. S., Penzo, E., Hutchison, J. E., Robinson, J. A., Manna, L., Borys, N. J., and Schuck, P. J., Journal of Physical Chemistry C (2020). https://doi.org/10.1021/acs.jpcc.0c01147

0D Nanocrystals as Light-Driven, Localized Charge-Injection Sources for the Contactless Manipulation of Atomically Thin 2D Materials

Ghini, M., Yanev, E. S., Kastl, C., Zhang, K., Jansons, A. W., Crockett, B. M., Koskela, K. M., Barnard, E. S., Penzo, E., Hutchison, J. E., Robinson, J. A., Manna, L., Borys, N. J., Schuck, P. J., and Kriegel, I., Advanced Photonic Research (2021). https://doi.org/10.1002/adpr.202000151

Photodoping of metal oxide nanocrystals for multi-charge accumulation and light-driven energy storage

Ghini, M., Curreli, N., Camellini, A., Wang, M., Asaithambi A., and Kriegel, I., Nanoscale (2021). https://doi.org/10.1039/D0NR09163D

Multi-charge Transfer from Photodoped ITO Nanocrystals

Ghini, M., Rubino, A., Camellini, A., and Kriegel, I., Nanoscale Advances (2021). https://doi.org/10.1039/D1NA00656H

Control of Energetic Band Profiles through Depletion Layer Engineering in Core-Shell Nanocrystals

Ghini, M., Curreli, N., Lodi, M. B., Petrini, N., Brescia, R., Wang, M., Fanti, A., Prato, M., Manna, L. and Kriegel, I., Nature Communications (2022). https://doi.org/10.1038/s41467-022-28140-y

Multi-Modal Plasmonic Dynamic Splitting in Doped Metal Oxide Nanocrystals
Ghini, M., Petrini, N., Rebecchi, L., Curreli, M., Manna, L. and Kriegel, I., *in preparation.*

Further scientific publications:

Colloidal Bi-Doped Cs2Ag1- xNaxInCl6 Nanocrystals: Undercoordinated Surface Cl Ions Limit their Light Emission Efficiency
Zhang, B., Wang, M., Ghini, M., Melcherts, A., Zito, J., Goldoni, L., Infante, I., Guizzardi, M., Scotognella, F., Kriegel, I., De Trizio, L., and Manna, L., ACS Materials Letters (2020). https://doi.org/10.1021/acsmaterialslett.0c00359

Strain tuning of nematicity and superconductivity in single crystals of FeSe
Ghini, M., Bristow, M., Prentice, J. C. A., Sutherland, S., Sanna, S., Haghighirad, A. A., and Coldea, A. I., Physical Review B (2021). https://doi.org/10.1103/PhysRevB.103.205139

Isolated [SbCl6]3- Octahedra are the Only Active Emitters in Rb7Sb3Cl16 Nanocrystals
Zhang, B., Pinchetti, V., Zito, J., Ray, A., Melcherts, A., Ghini, M., Pianetti, A., Infante, I., Brovelli, S., De Trizio, L., and Manna, L., ACS Energy Letters (2021). https://doi.org/10.1021/acsenergylett.1c01662

Two-dimensional (2D) indium selenide (InSe)/indium tin oxide (ITO) hybrid films for solution-processed photoelectrochemical (PEC)-type photodetectors in aqueous media
Bianca, G., A., Zappia, M., Bellani, S., M., Ghini, Curreli, N., Buha, J., Galli, V., Prato, M., Sofer, Z., Kriegel, I., and Bonaccorso F., *under revision.*

Structural and optical characterization of liquid-phase exfoliated bismuth telluride iodide (BiTeI)
Bianca, G., Trovatello, C., Zilli, A., Zappia, M., Bellani, S., Curreli, N., Conticello, I., Buha, J., Piccinni, M., Ghini, M., Celebrano, M., Finazzi, M., Kriegel, I., Antonatos, N., Sofer, Z., and Bonaccorso F., *under revision.*

Contents

I. Emergent light-driven nanostructures

I. 1 Introduction

A fast-changing climate is one of the most critical challenges our societies have to face, with enormous impact all over the globe in terms of human lives, economic damages, political stability, and with threatening consequences on the safety of ecosystems and the availability of primary resources.[1,2] The transition towards clean and renewable energy sources is essential to mitigate the worst aspects of global warming. While the production costs of green energy (for example, with solar cells or wind turbines) have significantly dropped in the last decade, reaching grid parity in many parts of the planet and systematically over-performing predictions year after year, there are still many non-trivial challenges on the way.[3–5] On one side, the electrification of the energy consumption, in sectors ranging from transport to heating and manufacturing, would significantly increase the electricity needs of nowadays' Nations while the perspective of a growing and wealthier population will fuel the demand for electrically powered devices in the incoming years, with the fundamental requirement of off-grid energy autonomy over extended periods of time.[1,6] On the other side, current technologies are not fully capable of coping with this growing demand. For the development of innovative and sustainable technologies, the realization of microdevices with ever-smaller dimensions and the decrease of the cost and power consumption of electronic components are critical criteria.[7] Renewable sources intrinsically have an intermittent nature with significant fluctuations, both daily and seasonal, and they require a separate unit where the harvested energy is stored, which increases complexity and introduces conversion losses.[8–10] Moreover, the state-of-the-art technologies for electronic devices and electric vehicles rely primarily on lithium-ion batteries, with strong limitations due to the cycle life, safety hazards, temperature conditions, and they present slow charge/discharge cycles and low power capacities.[11,12] In this context, it is clear the importance of developing new energy conversion and storage solutions. Nanostructured supercapacitors have the potential to change the world of energy storage, accelerating the transition towards renewable sources. Supercapacitors (SC) present several advantages in terms of power, speed of charging and discharging, and cycle lives with respect to rechargeable batteries. Furthermore, they can be integrated together with traditional batteries. SCs are being exploited for the improvement of the grid quality, to overcome power peaks, and are widely used for low-power electronics, such as smart portable devices and medical devices, in the automotive and rail industry, for start/stop and energy recovery functions and to

provide fast charge/discharge energy bursts.[11–13] The need for solar cells or batteries as separated units from the energy converter introduces several disadvantages in terms of size, energy losses, energy level mismatch, higher materials and maintenance costs, etc. A material system that is capable of both solar energy conversion and storage represents a unique opportunity for the integration of both functionalities into a single device.

Within this doctoral thesis, I investigate the potential of a specific materials system to fulfill this purpose, namely doped metal oxide nanocrystals (MO NCs). Pioneering studies reported values of areal and volumetric capacitance higher than those of commercially available solutions by using highly-doped metal oxide nanocrystals as soluble supercapacitors.[14] Remarkably, those colloidal doped MO NCs (such as iron-doped FeO NCs or tin-doped In_2O_3 NCs) can be charged in a contactless way, directly converting the light energy into extra photocharges.[14–16] The main mechanism is the so-called photodoping process, *i.e.*, the possibility to add quasi-permanently or permanently extra charges into the electronic structure of metal oxide NCs in a contactless way, by using light beyond the band-gap energy. Light absorption promotes electrons from the valence band (VB) to the conduction band (CB) and generates electron-hole pairs inside the nanoparticle. In the presence of a hole-scavenger, the holes are rapidly quenched at the surface of the semiconductor, leading to the photodoping of the material. Multiple electrons (up to hundreds of electrons in NCs of 5 nm of radius) can be thus stored inside the nanocrystal, which behaves as a light-driven supercapacitor.[15] Initial works, to which I contributed, demonstrated also photodoping in all-solid-state architectures, thanks to the coupling between MO NCs and monolayers of transition metal dichalcogenides (2D TMDs), a class of bidimensional semiconducting materials.[17] In the hybrid, MO NCs act as active elements in which light absorption and carriers separation occur, while the TMD single layer collects photo-generated carriers and facilitates the charge extraction process. The heterostructure can be photodoped (photocharged) to extents comparable to electrostatic gating and in a permanent and contactless way, indicating that the 0D-2D hybrid SC geometry displays promising volumetric and areal capacitances around F/cm^3 and $\mu F/cm^2$.[17,18] The photodoping process of optimized indium tin oxide (ITO) NCs, coupled with other nanostructured materials, could allow radical advances in the development of innovative light-driven, contactless applications. Multifunctional devices and light-powered energy storage solutions represent a fast-developing field with promising outcomes.[19] However, for the proper use of this process for solar energy storage, first, fundamental understanding of the photophysical mechanisms of photodoping is needed. Recent works have reported the formation of superficial depletion layers, which have a profound impact on the optoelectronic properties of MO NCs

and hence on the performance of MO-based devices.[20–22] Nonetheless, their role in the photodoping process has not yet been considered.[15] These aspects are investigated in detail in this doctoral work, unveiling the key importance of depletion layers modulation in the photodoping process of doped MO NC supercapacitors (**Figure 1a**).

Most of this doctoral project focused on the development of an innovative nanostructured material to accumulate, store and release solar energy. The work of these three years of Ph.D. analyzed the

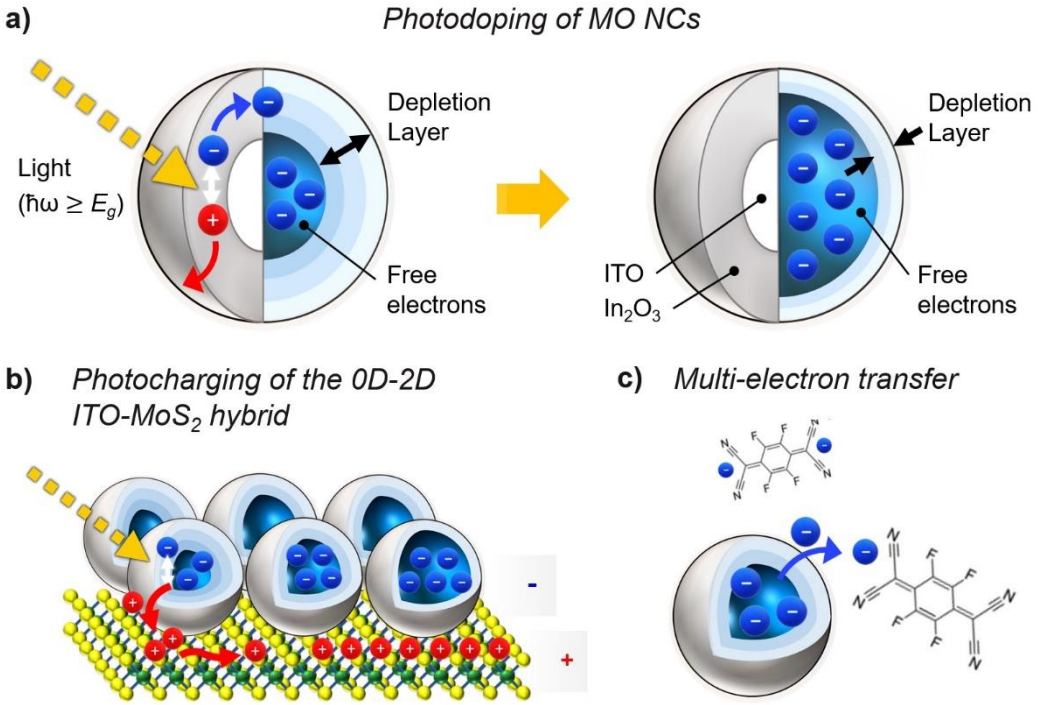

Figure 1 – Emerging light-driven nanostructures based on doped metal oxide nanocrystals (MO NCs). ***a)*** *Illustration of the photodoping process and storage of multiple electrons in a core-shell ITO-In_2O_3 nanocrystal. The left side of the sphere represents the physical structure of the NC; the right side depicts a simplified picture of the NC's electronic structure. Photons with energy (ħω) above the bandgap (Eg) generate electron-hole pairs in the MO NC. The photogenerated holes are quenched at the surface of the NC, while the photoelectrons are stored within the NC volume. The tuning of superficial depletion regions plays a key role in the accumulation of extra charges. This process can be facilitated with suitable hole-acceptors (panel b) or reversed with electron-acceptors that discharge the photoexcited NCs (panel c).* ***b)*** *Photocharging of a 0D-2D ITO-MoS_2 hybrid structure. The photogenerated holes are collected from the bidimensional material, that positively charges, while the electrons negatively charge the NCs.* ***c)*** *Transfer of multiple electrons between a photocharged MO NC and electron-acceptor molecules.*

fundamental features and limiting factors involved in the accumulation photodoping process, explaining the physical mechanism and electronic dynamics at its core.[15,23] It allowed the optimization of the 0D nanocapacitors in terms of optical responses and charge storage capabilities, as well as the tuning of biplasmonic optical features.[23,24] The manipulation of 0D-2D heterostructures via photodoping was investigated, proving the long-range diffusion of the photoinjected carriers in the 2D layers (**Figure 1b**).[17,18] Moreover, reversible multiple charge transfer reactions were observed and implemented as quantitative tool to perform electron counting of the stored photocharges (**Figure 1c**).[25] This work conveyed both theoretical modeling tools and experimental techniques of particular interest for the fabrication of nanostructured light-driven supercapacitors. Thanks to the progress achieved by our team we established milestones in the field of photodoping of MO nanocrystals and we are currently working on the development of the first fully-operating light-driven supercapacitor.

I. 2 Thesis outline

The structure of this Ph.D. dissertation is the following.

In **Chapter II**, the main concepts and materials of interest are introduced. A brief overview of the state of the art and the photodoping process is provided, as well as the main structural and optoelectronic properties of metal oxide nanocrystals and 2D transition metal dichalcogenides. Fundamental aspects such as the optical response of plasmonic NCs and depletion layer formation are discussed.

In **Chapter III**, the experimental techniques employed for the nanofabrication, the characterization, and for the dynamical modulation of the nanosystems analyzed are reported. Methods regarding spectral analysis of optical absorbance and photoluminescence, as well as simulations details, are described.

The following chapters (IV-VII) contain experimental results based on the research work conducted during the three years of Ph.D. (the related scientific publications can be found at page 5).

In **Chapter IV**, the photodoping process of ITO NCs is discussed. Experimental results on the photodoping of homogeneous particles and core-shell particles are presented, focusing on the modulation of their plasmonic response. Biplasmonic features are observed in core-shell NCs.

Chapter V investigates the electronic structure of MO NCs and the band bending induced by Fermi level pinning, both in the static case and under dynamic modulation after light excitation. The key role of depletion layers in photodoped MO NCs is analyzed and a new explanation for the photodoping process is proposed.

Chapter VI reports multi-charge transfer reactions from photodoped ITO NCs to widely-used organic electron acceptor molecules. The predicted charge storage enhancement of core-shell NCs is tested via oxidative titration.

Chapter VII reports the solid-state photodoping of the heterostructure based on 2D TMDs and core-shell ITO NCs. The capacitive behavior of the hybrid, with the permanent separation of charges in the structure, is confirmed. Spatial analysis of the emission spectrum of the 2D layer reveals the propagation of the photoinjected carriers and the driving force of the process is investigated.

Chapter VIII delineates perspectives for future liquid-phase and solid-state applications based on the photodoping of MO NCs, towards innovative implementations and light-driven energy storage solutions. Open questions and indications for future work are discussed.

Finally, **Chapter IX** summarizes the main finding of this work in a conclusive discussion.

II. Metal oxide nanocrystals and 2D transition metal dichalcogenides

During the last decades, nanoscience and nanotechnologies attracted the growing interest of the scientific community and became one of the most active fields of modern times, holding exceptional opportunities for the investigation of fundamental phenomena and promising perspectives for technological applications. At the nanoscale, quantum confinement effects become predominant and materials exhibit exotic states, as well as unique physical and chemical properties that are often superior to their bulk counterparts.[26–28] Currently, nanotechnologies have been exploited in almost every field from micro- and nano-electronics, to optoelectronics devices and photonics.[26,27,29] Their high surface-to-volume ratio is beneficial for catalysis and manufacturing, while quantum communication and quantum computing heavily rely on nanofabrication techniques.[30–33] The field of nanomedicine is emerging, with functionalized nanomaterials being studied for biomedical applications such as drug delivery, vaccines, diagnostic and therapeutic tools.[34–39] Nanomaterials have the potential to revolutionize present energy harvesting (*e.g.*, third-generation solar cells) and energy storage technologies, going beyond what is possible to achieve with traditional systems.[9,15,40–43] These features are a direct consequence of the reduced dimensionality in at least one spatial axis. Nanomaterials can be categorized in zero-dimensional (0D) (nanoparticles), 1D (nanotubes), and 2D (bidimensional materials), depending on the number of unconfined dimensions of the system. In this dissertation, I will explore the light-matter interaction in doped metal oxide nanocrystals (MO NCs) and layered transition metal dichalcogenides (2D TMDs). The coupling between these two semiconducting nanomaterials is investigated in a hybrid heterostructure for the future development of an innovative material system able to accumulate, store and release solar energy.

II. 1 Doped metal oxide nanocrystals

Metal oxides (MOs) are inorganic semiconducting materials composed of a metal cation and an oxide anion. MOs present an ideal combination of multiple properties and desirable features, including environmental stability, chemical tunability[44], optical transparency, and good carrier mobility,[45] making them very attractive materials for optoelectronics and energy-related technologies.[15,46] Currently, doped

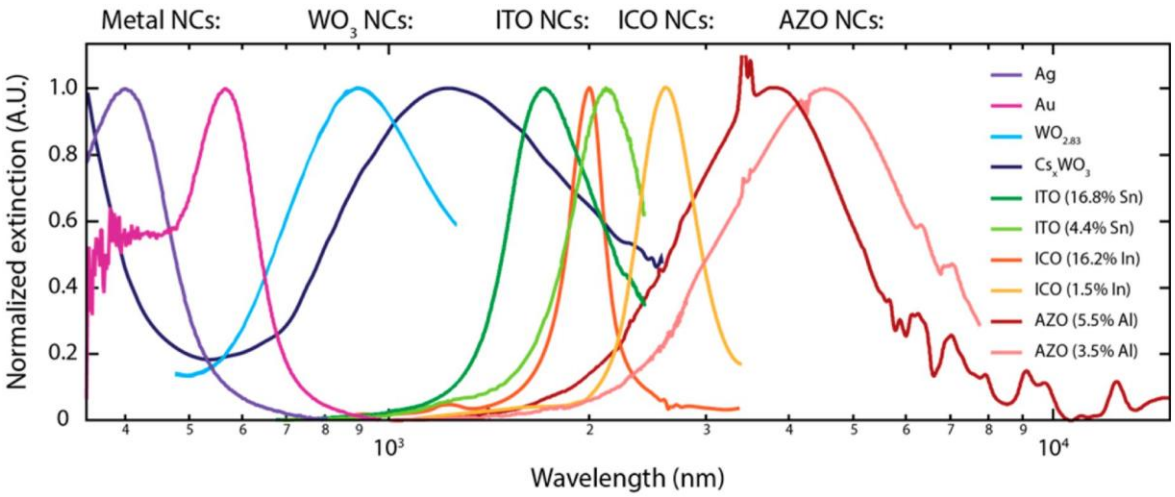

Figure 2 – Plasmonic resonances in metal and metal oxide nanocrystals. *Doped metal oxide NCs exhibit tuneable surface localized plasmon resonances that cover the near-infrared and infrared regions of the electromagnetic spectrum. Reproduced from Ref.*[56] *with permission from American Chemical Society.*

MO are widely used in research and industry as transparent conductive oxides (TCO), being simultaneously transparent in the VIS region (with greater than 80% transmittance of incident light) and electrically conductive (with conductivity values higher than 10^3 S/cm).[47–49] TCOs, of which Indium Tin Oxide (ITO) is a standard, are a fundamental component of many modern optoelectronic applications, such as inorganic and organic flat-panel displays, touch screens, organic light-emitting devices (OLED), and thin fin photovoltaics, including dye-sensitized solar cells.[47,48,50–53] Metal oxides can be synthesized in the form of nanocrystals (NCs), reaching sizes as small as a few nanometers.[54,55] Nanocrystals are nanoparticles with a regular crystalline structure and size comparable to the exciton radius, whose behavior is strongly influenced by quantum confinement effects. Doped metal oxide NCs are plasmonic materials characterized by strong and tunable localized surface plasmon resonances (LSPRs).[56–58] LSPRs in bulk metals like gold or silver, with carrier densities in the range of 10^{23} cm^{-3}, fall in the UV-visible range. On the contrary, doped metal oxides are transparent in the visible range due to the significantly lower carrier concentration level (two orders of magnitude lower), and their LSPRs cover the NIR-IR region of the electromagnetic spectrum. By carefully designing the structure, elemental composition, and placement of dopants within the NC volume, it is possible to control the shape and width of the resonance and tune its position over a large window of energies, as illustrated in **Figure 2**. Due to the presence of LSPRs, a large number of plasmonic applications have been developed or proposed in recent times.[59] Nanostructures with localized surface plasmon resonances have been investigated for sensing of single

molecules, signal enhancement, surface-enhanced infrared spectroscopy, optical coatings, smart window technologies, and biomedical applications such as plasmon photothermal therapy (PPTT), among many others.[57,59–63] The modulation of their charge carrier density can be efficiently achieved through aliovalent substitutional doping and post-synthesis techniques, further boosting the implementation of doped MO NCs of targeted features.[15,57,64,65] In particular, doped MO NCs incorporate the ability to store hundreds of capacitive charges in nanometric volumes and the possibility to efficiently harvest NIR sunlight radiation through size- and doping- dependent LSPRs.[15,17,18,50]

II. 1.1 Synthesis of highly-doped MO NCs

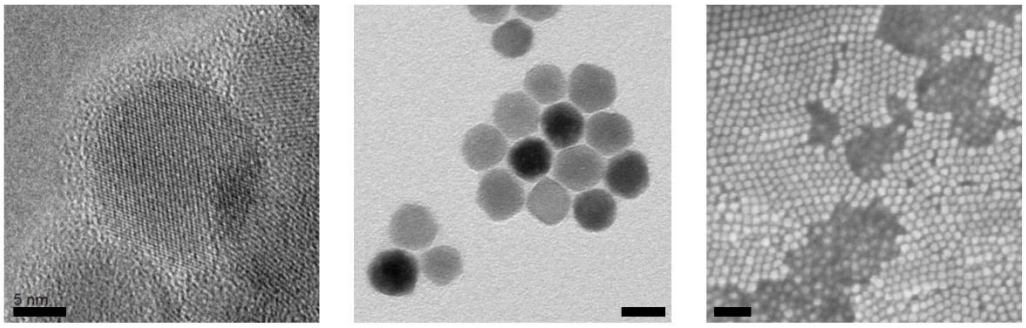

Figure 3 – Electron microscopy images of ITO-In_2O_3 core-shell NCs. *HRTEM image (on the left) and TEM image (center) of ITO NCs employed in this work. On the right, SEM image of a thin film of spin-coated ITO NCs. Scale bar is 5 nm for panel a, 15 nm for panel b and 50 nm for panel c.*

The optical and electrical properties of doped MO NCs are dictated by the concentration levels of free carriers and their spatial profile in the NC volume. Degenerately-doped MO NCs are capable of withstanding extraordinarily high levels of doping without deteriorating their internal morphological structure.[57] Typical electron densities are in the range of 10^{21} cm^{-3} and are determined mostly by the doping levels imposed at the synthesis stage. Degenerately-doped MO NCs present metallic-like character and, in most cases, the behavior of the population of free electrons interacting with incoming radiation can be successfully described as free electron gasses coherently oscillating. The doping level determines the free carrier concentration, allowing the continuous tuning of the optical properties of MO NCs over a wide range of wavelengths. Doping can be achieved both during the synthesis stage, by exploiting different chemical approaches (such as intrinsic doping, aliovalent substitutional doping, extrinsic interstitial doping [54–57,66]), and post-synthetically, by applying an electrochemical potential or by absorbing beyond-bandgap light.[14,67–69] A broad variety of synthesis methods can be employed for the

growth of MO NCs, spanning from solution-based approaches, including solvothermal, sol–gel, microemulsion, microwave-assisted, and solvothermal methods, to vapored state based and biological synthesis methods.[15,70] Advances in non-aqueous sol-gel methods achieved through the use of inert organic solvents allowed to avoid several disadvantages of aqueous systems.[71,72] In recent years, numerous doped MO NCs (such as ITO NCs) have been synthesized employing the so-called living nanocrystal growth methods.[54] This continuous growth approach involves the slow injection of precursors in the reaction flask, allowing precise control over the main parameters of the synthesis. [55,73] Several chemical strategies can be employed for the doping of MO NCs at the synthesis stage, ranging from intrinsic doping due to lattice point vacancies (*e.g.*, oxygen vacancies contributing with two additional electrons) to extrinsic interstitial doping (*e.g.*, Cs doping in WO_3 NCs), or aliovalent substitutional doping with donor impurities (*e.g.*, Fe doped ZnO NCs, Sn doped In_2O_3 NCs).[56,57,74,75]Further information on the synthesis technique employed for the nanofabrication of doped metal NCs and core-shell NCs investigated in this work can be found in **Chapter III**. Doped MO nanocrystals manifest an extreme tunability of their optoelectronic properties. Their optical response change as a function of size, shape, doping levels, and the radial distribution of dopants (together with damping and dopants activation).[55,76] As discussed in **Chapter IV**, these nanoparticles can be synthesized in a core-shell configuration, with the core of the nanocrystal made of ITO and the shell of In_2O_3 or vice versa. With this design, the fine-tuning of the shell thicknesses allows controlling the resonance frequency of the surface plasmons.[55,76] Furthermore, it is known that charge carriers levels in ITO nanocrystals are sensitive to vacancies generation, aliovalent doping, electrochemical doping and, most importantly for the purpose of this project, to photodoping.[15,16] High-resolution transmission electron microscope (HR-TEM) and X-Ray Diffraction (XRD) studies confirm the crystalline structure of these NCs. Soluble doped MO NCs can be employed for the fabrication of thin films, with thickness ranging from a single layer of nanoparticles to several hundreds of microns, with spray deposition processes or simple spin-coating techniques. Thin films of MO NCs have been recently investigated both in solid-state structures and in solution environments for electrochromics and the above-mentioned applications.[63,77] **Figure 3** shows electron microscopy images of the ITO NCs employed in this dissertation. Moreover, doped metal oxide NCs can be dispersed in polar and non-polar solves, and the functionalization of the NC surface can be achieved with ligand stripping and ligand exchange procedures.[77]

II. 1.2 Fermi level pinning and depletion layer formation

Undoped metal oxides are intrinsic semiconductors and the Fermi level lies at the center of the bandgap. Through doping, the energy of the Fermi level rises above the conduction band minimum and, consequently, the transport and optoelectronic properties of metal oxides dramatically change. This simple description well depicts the behavior of bulk materials. This effect becomes more important on the nanoscale due to the high surface-to-volume ratios.

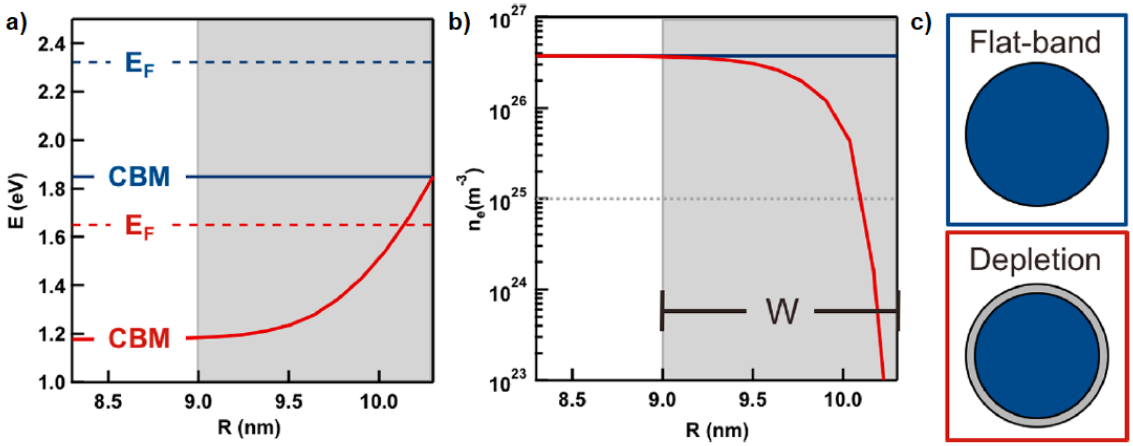

Figure 4 – Depletion layer formation due to Fermi level pinning in MO NCs. ***a)*** *Simulated intra-NC radial potential profiles for the conduction-band minimum (CBM) (solid lines) and the Fermi level (E_F) (dashed lines) for a 20.6 nm diameter ITO NC containing 3 atom % Sn when the surface potential dictates flatband conditions (blue) and depletion conditions (red).* ***b)*** *n_e profiles under flat-band (blue) and depletion (red) conditions. The dashed gray line denotes the Mott criterion for metallic conductivity in ITO.* ***c)*** *Two-dimensional cross sections of the n_e profiles in (b) under (top) flat-band and (bottom) depletion conditions. Adapted from Ref.* [27] *and Ref.*[28] *with permission from American Chemical Society.*

The energetic structure of metal oxide NCs is significantly altered by space charge effects, owing to the abrupt interruption in lattice periodicity and the formation of electronic states at the NC surface. These surface states originate from the presence of superficial trap states, vacancies, and defects. Their energies are affected by the interplay between the uncoordinated surface atoms and surrounding bound molecules, such as ligands. Space charge layers cause local variations in the electronic structure of the nanocrystal and, as predicted by Poisson's equation, ultimately result in the Fermi level pinning of the bands. The conduction band of the semiconductor pins to the surface potential and curved either up or down, depending on the surface state energies. In doped metal oxides, surface states' energies naturally lie below

the Fermi level energy (for ITO NCs, surface hydroxyls have been suggested as surface states)[69], causing an upward bending of the conduction band at the NC surface with significant deviations from the flat-band case. The radial dependence of the conduction band translates into a gradient in the carrier density (n_e), with the consequent formation of electronically depleted layers.[20,76,78] The suppression of carrier density in the superficial region of the NC can reach such an extent that the metallic character is completely suppressed.[21,22] Apart from native surface states, similar band bendings can be achieved under the effect of an oxidizing potential (upward bending) or reducing potential (downward bending), with the application of an external bias, resulting in the formation of depletion or accumulation layers of width W.[69] **Figure 4** reports typical conduction band bending of ITO NCs.

The effects of surface perturbations extend into the system over several nanometers. These deviations cover a substantial fraction of the NC volume (the typical diameter of an ITO NC is ~10 nm) and exert a significant influence on the optoelectronic features of nanostructured doped metal oxides.[20–22,79] Models based on a flat-band assumption neglect Fermi level pinning effects and, hence, are not precise descriptors of the free carriers' behavior in MO NCs. The formation of native depletion layers in MO NCs was firstly proposed in 2018 by Zandi and Agrawal *et al.* to explain the optical absorption of ITO NCs.[20] Since then, their presence has been confirmed by several works and their impact on transport and plasmonic properties have been experimentally investigated.[21,69,80–83] To precisely calculate the space-dependent energy band profile of semiconducting NCs, Poisson's equation has to be solved in spherical coordinates.[84] Recently, Staller *et al.* numerically calculated the Poisson's solutions for ITO NCs, delineating the radial profile of conduction bands and carrier densities (**Figure 4**).[22] The formation of depletion layers directly affects the electric field enhancement of metal oxide NCs (which decay exponentially with the width W), the plasmonic resonance and its sensitivity to the surroundings.[20–22] Fermi level pinning reduces the conductivity of thin films, constituting a potential barrier at the surface of the NC that isolates the free carriers within each particle and hinders the hopping mechanism. The net results of depleted layers is a detrimental effect on the performances of TCOs based on MO NCs. Furthermore, Fermi level pinning considerably modifies the dielectric function of the nanoparticle and its spatial dependency, with the electronically depleted region acting as a dielectric layer.[20]

II. 1.3 Plasmon resonances in MO NCs

In a conductive medium, the interaction between electromagnetic waves and a population of free electrons results in the formation of plasma oscillations (*i.e.*, Langmuir waves). In a classical picture, the

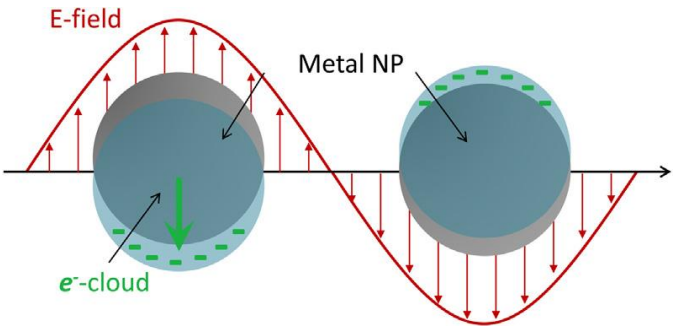

Figure 5 - Schematic of plasmon oscillation for a spherical metallic nanoparticle*, showing the displacement of the conduction electron charge cloud relative to the core in an oscillating electric field. Reproduced from Ref.* [57] *with permission from Elsevier.*

electric field drives the displacement of the free electrons, which are pushed to follow the incoming radiation frequency while the positive ions of the crystal lattice act as restoring forces (**Figure 5**). The oscillation of the carrier density can be described with a model harmonic oscillator subject to energy loss. From the quantization of these plasma oscillations, it arises the plasmon, the fundamental unit of the coherent collective excitation. Other quasiparticles can emerge depending on the interaction with additional quasiparticles (*e.g.*, a polariton from the coupling of a plasmon and a photon). For metals and systems with metallic character, the Drude-Lorentz model of electron gasses is widely used. The Drude complex dielectric permittivity is given by:

$$\varepsilon(\omega) = \varepsilon_\infty - \frac{\omega_P^2}{\omega^2 + i\omega\Gamma} \quad (1)$$

where ω_p is the bulk plasma frequency:

$$\omega_p = \sqrt{n_e e^2/\varepsilon_0 m^*} \quad (2)$$

with n_e being the free carrier density, m^* the effective electron mass, e the unit of elementary charge, and Γ the damping parameter. In this picture, plasma resonances originate as instabilities of the complex dielectric function. Plasma oscillations can be localized at the surface of bulk materials, leading to the formation of surface plasmons. In nanoparticles, the oscillation of the free carriers is confined at the nanoscale level, generating the so-called localized surface plasmon resonances (LSPRs). The nanostructure's morphological shape strongly affects the field's distribution, leading to the formation of various localized resonances and significant field enhancement in the correspondence of tips and sharp curvatures.

In order to characterize the plasmonic behavior of MO NCs, optical models established for conventional plasmonic materials have been adapted.[57,62,69] The propagation of light in a solution of nanoparticles can be described with the Lambert-Beer equation:

$$I = I_0 \cdot e^{-(\sigma_{ext})\rho L} \tag{3}$$

where I is the transmitted light intensity, I_0 is the intensity of the incident light, σ_{ext} is the far-field extinction cross-section, ρ is the volumetric density of particles, L is the light pathlength. With the assumption that the only possible interactions between the photon and the NCs are absorption and scattering, it is possible to write the extinction cross-section as $\sigma_{ext} = \sigma_{abs} + \sigma_{scat}$. A commonly used description relies on the Mie solution of Maxwell's equations, valid for the scattering of radiation by spherical particles,[85] and the quasi-static (dipole) approximation.[86] This approximation holds when the particle size is small compared to the electromagnetic wavelength, so that the electric field interacts almost instantaneously with the entire volume of the NC. Given the nanometric size of MO NCs, only dipolar excitations are considered, neglecting higher-order oscillations.[87] Therefore, the absorption and scattering cross-section can be written as:

$$\sigma_{abs}(\omega) = 4\pi k_H R^3 Im\left\{\frac{\varepsilon(\omega)-\varepsilon_H}{\varepsilon(\omega)+2\varepsilon_H}\right\} \tag{4}$$

$$\sigma_{scat}(\omega) = \frac{8\pi}{3} k_H^4 R^6 \left|\frac{\varepsilon(\omega)-\varepsilon_H}{\varepsilon(\omega)+2\varepsilon_H}\right|^2 \tag{5}$$

Here, R is the radius of NC, $k_H = \omega\sqrt{\varepsilon_H}/c$ is the wavevector for the host medium (of dielectric permittivity ε_H), and $\varepsilon(\omega)$ the NC Drude-like dielectric permittivity. By applying the so-called Fröhlich condition, $\mathrm{Re}\big(\varepsilon(\omega)\big) = -2\varepsilon_H$, to equation (4) and (5), it is possible to write the LSPR frequency (ω_{LSPR}) as:

$$\omega_{LSPR} = \sqrt{\frac{\omega_P^2}{\varepsilon_\infty+2\varepsilon_H} - \Gamma^2} \tag{6}$$

The LSPR is influenced by the surrounding medium in which the NCs are immersed. As a consequence of equation (6), a high (low) dielectric of the host medium results in a decrease (increase) of the plasmon resonance.[57] The oscillating carriers of the LSPR amplify the impinging electromagnetic wave generating a field several orders of magnitude stronger. This phenomenon is called near-field enhancement (NFE). The plasmonic field expands outside the NC volume following an exponential decay law and is the origin of the extreme sensitivity of the LSPR to its surrounding (justifying applications for sensing). The

damping coefficient Γ accounts for the energy losses of the collective oscillations of carriers due to electron scattering with electrons, phonons, lattice defects, and impurities.[88,89] Ultimately, the energy of the LSPR gets released as heat, heating the medium and the NC surrounding (hence, the plasmon photothermal effect). Γ can be written as the sum of independent contributions $\Gamma = \Gamma_{e-e} + \Gamma_{e-phonon} + \Gamma_{e-defect} + \Gamma_{e-surface}$ and is indirectly linked to the width and lineshape of the localized surface plasmon resonance.[57,90] In the case of ITO NCs, an empirical frequency-dependent damping function can be employed to describe the damping parameter as a function of ω:

$$\Gamma(\omega) = \Gamma_L - \frac{\Gamma_L - \Gamma_H}{\pi}\left[tan^{-1}\left(\frac{\Gamma_X}{\Gamma_W}\right) + \frac{\pi}{2}\right] \quad (7)$$

Here, Γ_L and Γ_H are the damping constants for the low- and high-frequency regimes, Γ_X is the crossover frequency describing the mixed regime, and Γ_W is the crossover region width. The asymmetry empirically observed in the LSPR of ITO NCs can be correctly modeled with this frequency-dependent damping function.[76,91] Finally, the extinction, $EXT = \log(I_0/I)$, is the physical observable that is experimentally accessible. For ITO NCs analyzed in this Thesis, the contribution of the scattering cross section is negligible and extinction and absorption can be used interchangeably:[86]

$$EXT = \frac{\sigma_{ext}\,\rho L}{ln(10)} = \frac{\sigma_{abs}\,\rho L}{ln(10)} \quad (8)$$

As explicated by eq. (2), carrier density levels determine the frequency of the plasmon resonance and, hence, by observing the absorption spectrum of plasmonic materials is possible to extract useful insights on their electronic structure. This aspect is particularly important for doped semiconductors, where small variations in the number of free carriers can be easily detected due to the relatively low carrier densities.

II. 2 Dynamic modulation of MO NCs

The plasmonic response of MO NCs can be modified by post-synthetic modulations of the carrier density level. Dynamic control over the optoelectronic properties of doped metal oxides can be achieved by applying an external bias (*i.e.*, electrochemical tuning) or via the optical absorption of light beyond bandgap (*i.e.*, photodoping). Owing to the extreme sensitivity of the plasmonic resonances to the carrier concentration (as well as to size, shape, and dielectric surrounding), the spectroscopic analysis of LSPR modulations is a valuable source of information for the doping processes occurring in MO NCs.[57,62,92–95]

Here, I introduce the dynamic modulations of the optoelectronic properties of MO NCs, together with an overview of LSPR modulations in colloidal NCs. In particular, I summarize the recent developments of the light-driven charging process of photodoped MO NCs for multi-charge accumulation. Theoretical background on the photodoping process of doped metal oxide NCs is provided and the main concepts, unresolved open questions, spectroscopic and theoretical tools to characterize the light-driven charging process are discussed.

II. 2.1 Post-synthetic electro-modulation of LSPR

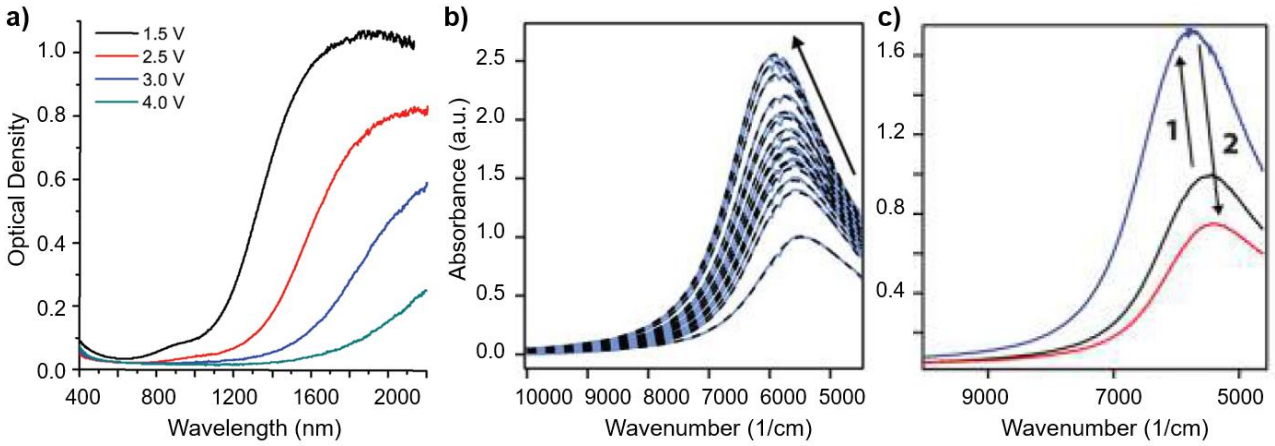

Figure 6 – LSPR modulations induced with electrochemical potential. ***a)*** *Variations in the absorption of a MO NC thin film induced by an external bias.* ***b)*** *Results of a typical reduction experiment for colloidal NCs in an electrochemical cell (−1.5 V), for time intervals of approximately 1 min over a total time of 2 h/1 h.* ***c)*** *The process of reduction and oxidation in a sequential manner: the initial blue-shift and increase in intensity, when applying a negative potential (black to blue curve), is completely reversed when switching to a positive potential, finally surpassing to a red-shifted and intensity decreased LSPR (red spectrum). Panel a adapted from Ref.* [96]*, panel b and c adapted from Ref.* [69] *with permission from American Chemical Society.*

Recent works demonstrated the possibility of tuning the LSPR frequency over a wide portion of the spectrum. In a notable work, Garcia *et al.* reported an electronically-induced shift greater than 1200 nm in the LSPR peak energy of MO NCs (**Figure 6a**).[96] Control over the optical response was achieved by immerging a thin film composed of ITO NCs in a $LiClO_4$ electrolyte solution and applying a negative and positive bias (with potential ranging between 1.5 and 4 V) to the electrochemical cell. The external bias induces modulation in the carrier density of ITO without affecting the morphological structure of

the NCs and without inducing degradation effects. Remarkably, charge and discharge cycles were repeated several times in a reversible way. As predicted by eq. (2), an increase in carrier density increases the plasmon absorption and induces a blueshift of its peak position, while a positive bias results in a redshift of the LSPR energy. The extent of the modulation of carrier density was in the order of $\sim 1 \cdot 10^{21}$ cm^{-3}, as calculated with optical modeling. Interestingly, the extent of the LSPR modulation under the applied bias is a function of the NC size.[96] A series of NCs of diameter ranging from 4.1 to 12.6 nm were analyzed and the greater variations in the optical density of the plasmon were observed in the smallest particles. In a similar study, Agrawal *et al.* reported the modulation of LSPR intensity and frequency of a colloidal solution of ITO NCs.[69] Starting from an optical density close to the unit, by applying a negative bias (-1.5 V) to the electrochemical cell, the peak intensity of the LSPR reached values as high as ~2.5 optical densities (**Figure 6b**). Control over the LSPR was demonstrated with cycles of negative and positive electrochemical potential, showing the reversibility of the process in solution (**Figure 6c**).[69]

Post-synthetic modulation of the plasmonic properties of MO thin films has been demonstrated in all-solid-state architectures too. In their work, Feigenbaum *et al.* reported control of carrier populations and refractive index in a metal-oxide-semiconductor heterostructure (Au-ITO-SiO_2-Au).[97] By applying an external electric field, carrier density variations in the orders of $\sim 1 \cdot 10^{22}$ cm^{-3} were achieved, as well as unity-order localized change in the index of refraction at visible frequencies. The authors indicated the formation of an accumulation layer at the SiO_2-ITO interface as the origin of the optical variations.[97] Similarly, the electrochemically-induced capacitive charging of ITO NCs solutions and thin films can be explained with the tuning of accumulation and depletion layers.[69,96] Surface effects are expected to be relevant for devices based on NCs networks; thus, externally-induced carrier density modulations could significantly affect the transport properties of similar nanostructures. Furthermore, the ability to tailor the LSPR of MO NCs and dynamically control it could open interesting perspectives for the development of dynamic sensors for the targeting of specific molecules.

II. 2.2 Photodoping and multi-charge accumulation of MO NCs

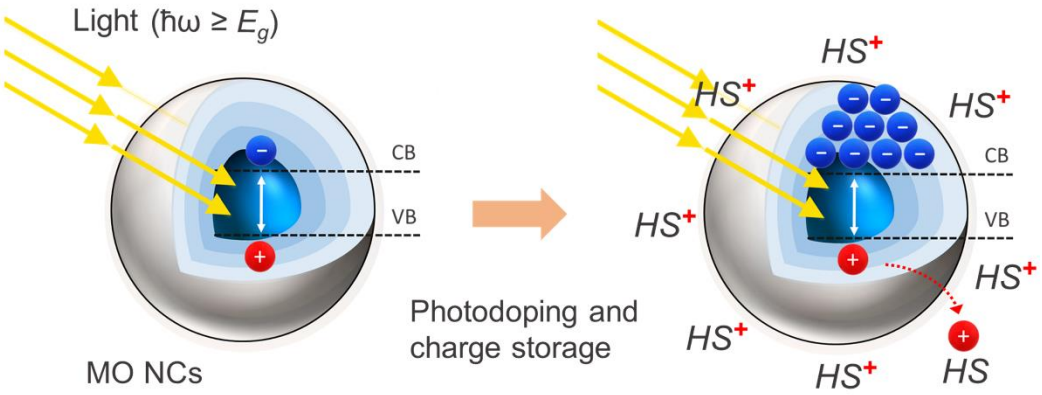

Figure 7 – Photodoping and multiple charge accumulation in doped MO NCs. *Light absorption with energy (ħω) above the bandgap (Eg) promotes an electron from the valence band (VB) to the conduction band (CB). By removing the photo-generated hole with a hole-scavenger (HS), the electron-hole pair recombination is suppressed and the extra electron is stored in the nanocrystal. The absorption of several photons results in the accumulation of multiple photoelectrons in the NC and leads to the overall photodoping of the material. Reproduced from Ref.* [15] *with permission from the Royal Society of Chemistry.*

The photodoping process of MO NCs, *i.e.*, the contactless variation of the number of conduction band electrons after absorption of photons, is depicted in **Figure 7**. Light beyond the bandgap energy of the MO NC promotes electrons from the valence band (VB) to the conduction band (CB), generating electron-hole pairs inside the nanocrystal. In the presence of hole-scavengers (*HS*), the photogenerated holes are rapidly quenched at the surface of the semiconductor, suppressing electron-hole pair recombination (radiative and non-radiative). In inert environments, this stabilizes the photogenerated electrons within the NC, leading to the overall negative doping of the material.[14,16,98] This light-driven process can be repeated several times upon exposure to light, resulting in the accumulation of multiple electrons. For nanoparticles with a size of ~10 nm in diameter, hundreds of extra charges can be (quasi-) permanently stored. Time-resolved analyses of the photodoping process indicate capacitive-like charging dynamics, showing that MO NCs behave as light-driven supercapacitors.[67,68] In solution environments, the negative photocharging of the nanoparticle is compensated by the formation of cations layers in the proximity of the NC surface, preserving a neutral electrostatic equilibrium.[14] Photodoping

was described by Haase *et al.* for zinc oxide nanocrystals (ZnO NCs), and, up to date, it has been observed in several MO NCs ranging from titanium oxide (TiO_2) to tin-doped indium oxide (ITO) NCs.[16,99,100]

The suppression of the recombination process is crucial to trigger the photodoping process. The photogenerated charges are prone to two competing mechanisms. The extra holes can recombine with their electron counterparts without altering the NC carrier density (*i.e.*, recombination) or, as in the case of stored carriers, lead to the photo-oxidation of hole scavengers at the NC surface (hole-capture). The accumulation of multiple photoelectrons in the CB of MO NCs is made possible by the different rates of the two mechanisms. Auger recombination (~150ps) is typically an order of magnitude slower than the hole-capture process (<15ps). However, multicarrier recombination rates increase with the number of excess charges introduced in the system.[78] The resulting kinetic equilibrium between Auger recombination and hole-capture processes ultimately determines the maximum number of extra electrons stored per NC. Hence, the outcome of the photodoping process is strongly affected by the nature of the hole-capture process.[78] As a matter of fact, when alternative hole scavenger molecules such as alcohols, organic acids, hydrocarbons, or even organometallic compounds are used, the (average) maximum number of extra charges that can be stored in each NC changes dramatically.[78] By coupling MO NCs to strong hole scavengers, such as $Li[Et_3BH]$ or $K[Et_3BH]$ instead of ethanol (EtOH), the number of stored charges has been quadrupled. However, in those cases, the photodoping process appears to be irreversible.[101,102] The photo-oxidation of the hole scavengers at the NC surface can happen directly or indirectly. In the latter case, the hole acceptor undergoes indirect oxidative reactions by interacting with interfacial OH radicals formed as a consequence of the holes trapping at −OH surface groups.[78,102–105] In the case of ZnO NCs, the photodoping process results in the oxidation of two molecules of ethanol, when employed as hole scavenger, and the consequent formation of acetaldehyde ($ZnO + ½CH_3CH_2OH \rightarrow ZnO^- + H^+ + ½CH_3CHO$). In this example, however, the inverse reaction limits the number of electrons accumulated in the NC ($ZnO^- + H^+ + ½CH_3CHO \rightarrow ZnO + ½CH_3CH_2OH$).[103] The thermodynamic equilibrium between ethanol oxidation and acetaldehyde hydrogenation determines the maximum number of extra charges stored in ZnO NCs. Moreover, it has been reported that the accumulation of acetal acetaldehyde and proton-driven surface reactions deform the band structure of the NC due to Fermi level pinning.[103] Apart from the hole-capture processes, numerous other factors influence the photodoping process of MO NCs. [16,103] For example, it is known that electrostatic interactions and surface reactions can alter the photodoping dynamics.[78,106] Notably, the maximum number of additional photoelectrons is found to be independent from the initial carrier density of the NC. It has been shown

that the maximum carrier density level that can be achieved via photodoping is a fixed value independent from the NC size. Thus, the maximum number of stored carriers grows together with the radius of the NC with a cubic law ~R^3, with bigger particles storing more electrons proportionally to their volume.[78]

Charge storage in photodoped MO NCs

The photodoping process in MO NCs is reversible and can be repeated multiple times, exhibiting a capacitor-like behavior.[14,100,107] As mentioned before, the photodoping mechanism requires anaerobic conditions to accumulate charges in a stable way in solution environments. The interaction with air molecules leads to the oxidation of photodoped MO NCs, providing a first example of the reversibility of the charging process.[107] In solutions of photodoped MO NCs, the oxidized hole scavenger molecules get electrostatically drawn to the surface of the NC due to their positive charge, ensuring the system's overall neutrality. The charge-compensation mechanism results in significant variations of the electric properties of the NC, with a generalized shift of the Fermi level energy (E_F).[108] Moreover, the interaction between the extra photoelectrons and the charged cations attached to the NC surface affects its chemical reactivity.[106,109] The accumulation of these positive charges at the surface of the negatively charged NC resemble an electric double-layer. More generally, photodoped NCs can be effectively described as soluble nanosized supercapacitors, with capacitive and pseudocapacitive charging dynamics.[14,17,67,68,78,108] The double-layer electrostatic capacitance and the electrochemical pseudo-capacitance are distinctive traits of supercapacitor systems.[110] Thanks to the reduced separation between opposite charges, unachievable with conventional electrostatic capacitors, both high storage capacity and high power can be simultaneously attained.[13,111] The behavior of electric double-layer capacitors (EDLC) can be depicted similarly to those of traditional capacitors. EDLCs store electrons at the so-called double-layer, which generates at the interface between the surface of a conductor material and an electrolytic solution.[112] As for conventional capacitors, the electrostatic attraction between the opposite charges of the bi-layer forms a static electric field accounting for the intensity of the voltage. In the analogy, the double-layer corresponds to the dielectric layer of a traditional capacitor.[113–115] It is then possible to rewrite the classic equation for traditional capacitors (*i.e.*, $C = (A\varepsilon_0\varepsilon_r)/d$, with d being the separation of the plates) by taking into account the thickness *t* of the double-layer.[26] In EDLCs, the charge separation is in the orders of the Angstroms.[116] The equation for the for the double-layer capacitance (C_{dl}) is given by: [26]

$$C_{dl} = \frac{A\varepsilon_0\varepsilon_r}{R} \cdot \frac{R+t}{t} \quad (9)$$

where *A* is the sphere's surface area, *R* is the NC radius, ε_0 and ε_r are the permittivity of free space and the dielectric constant of the solvent, respectively. However, solutions of photodoped MO NCs include charge transfer processes across the solid-liquid interface, which is more akin to pseudo-capacitance phenomena. Pseudo-capacitance systems store energy with reversible faradaic redox reactions and electron-charge-transfer processes occurring on the surface of the material.[117] These faradaic charge transfer events are often followed by a very rapid series of reversible redox, intercalation, or electrosorption processes, without inducing corresponding chemical reactions.[117,118] The determination of the physical capacitive phenomenon occurring at the surface of photodoped MO NCs is still under debate and is currently an open question. Further studies are required to accurately describe the charging dynamics of MO NCs at the microscale. A comprehensive understanding of the photodoped NCs both at the nanoscale, on the thermodynamics of charge transfer reactions, and at the NC level, on the charge storage scheme (pseudocapacitive vs. double-layer capacitive), is needed. Control over the surface chemistry of the NC (*e.g.*, functionalizing the surface ligands) could help clarify this matter.[15]

In the case of Fe-doped ZnO NCs ($Zn_{0.99}Fe_{0.01}O$), the number of extra charges is significantly enhanced by the Fe-doping, which provides an extra acceptor state immediately below the CB minimum. As a result, the extra charges can be easily stored and removed from these highly localized states owing to the equilibrium between Fe levels and the MO conduction band.[14] Moreover, electron paramagnetic resonance (EPR) spectroscopy highlighted the presence of unpaired free electrons in ZnO NCs upon charging, with g^* values in the range of 1.960-1.968 (depending on the NC size).[107] These studies further confirm that the extra electrons introduced via photodoping in MO NCs are free charges delocalized in the conduction band. Charge and discharge cycles, performed with light-induced reduction and oxidation reactions, showed the cyclical appearance and disappearance of the EPR signal. Photodoping can be exploited as a mean to control the magnetic properties of MO NCs, with possible implications for spintronic technologies and related applications.[57] Ochsenbein *et al.* reported charge-controlled magnetism in colloidal Mn^{2+}-doped ZnO nanocrystals.[119] When doped with Mn^{2+} ions, these NCs exhibit a large magnetic momentum stable at room temperature. The light-induced accumulation of extra free electrons in the CB disrupts the magnetic coupling of Mn ions, as marked by the disappearance of the original EPR signal. Similar studies on Fe-doped ZnO NCs showed reversible switching of the oxidation state of Fe^{3+} ions via photodoping.[120] Several means have been implemented to induce reductive

(charging) and oxidative (discharging) reactions of MO NCs, including absorption of light, electrical fields, and chemical reactions.[25,69,96,97,100]

II. 2.3 Photodoping effects on the optical properties and deviations from the flat-band picture

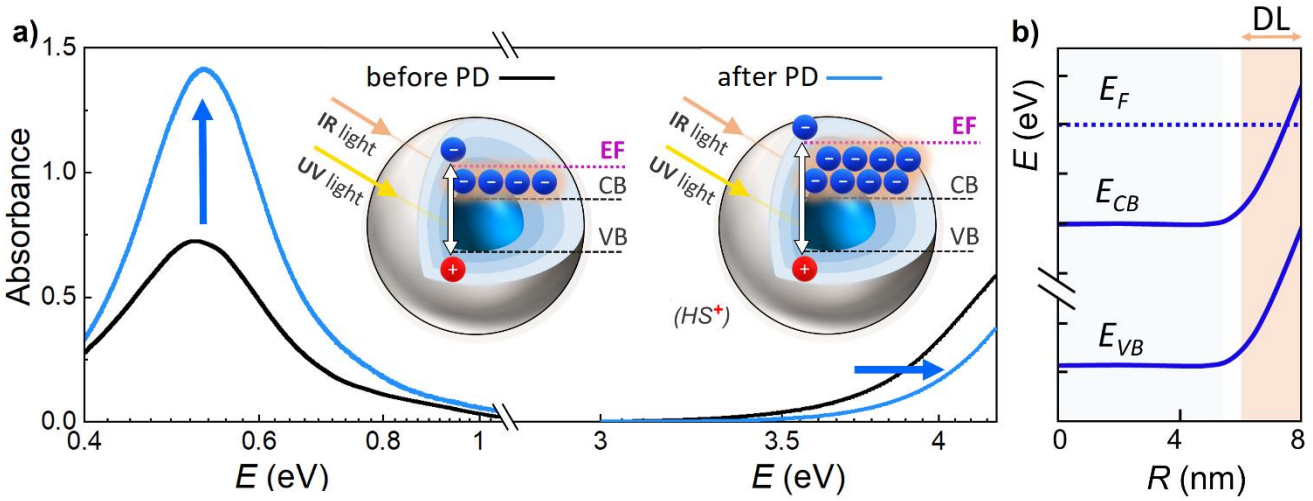

Figure 8 - Photodoping of colloidal MO NCs. a) *Photodoping effects on the optical spectrum of doped MO NCs. Typical localized surface plasmonic resonance (LSPR) of ITO NCs before (black line) and after (blue line) the photodoping process peaking at around 0.5 eV. With UV exposure the peak position of the plasmon resonance slightly blue shifts and its absorption significantly increases. The Moss–Burstein effect after photodoping results in the blue-shift of the absorption onset in the UV spectral range. Inset shows an illustration of the Fermi energy shift within the flat-band picture, before and after the photodoping process with UV light, and the resonant absorption of IR light by the free electrons.* ***b)*** *Illustration of the electronic structure of a MO NCs with the Fermi level pinning and the consequent formation of an electronically depleted layer (DL). Figure reproduced from Ref.[15] with permission from the Royal Society of Chemistry.*

Theoretical calculations and EPR spectroscopy measurements demonstrated the delocalized nature of the extra electrons introduced via photodoping.[100,121,122] Hence, after light absorption, these free electrons increase the initial carrier density of doped MO NCs and actively contribute to the formation of localized surface plasmon resonances (LSPRs) in the NIR (**Figure 8a**).[57,92,93,123] As introduced in this chapter, the plasmonic resonances of MO NCs are extremely sensitive to carrier density variations, as well as to modulations in size or dielectric surrounding. For these reasons, the spectroscopic analysis of LSPRs is

a precious tool to monitor the photodoping process of MO NCs and extract information on their electronic structure.[15,23,57,62,92–95] In particular, the proportionality between the LSPR frequency (ω_{LSPR}^2) and the carrier density (n_e), can provide useful insights for homogeneous NC, while for more complex architectures, such as core-shell MO NCs, the spatial distribution of n_e within the NC volume has to take into account.[22,23,55,58,92,124–126] As a matter of fact, real-time quantitative analysis of the photodoping process can be achieved by monitoring the LSPR spectral modulations. In the case of ITO NCs, UV exposure in anaerobic conditions leads to a significant increase in the plasmon peak intensity and a blueshift of its energy (**Figure 8a**).[16] In first approximation, the increase in absorption of the LSPR feature is due to a larger number of free carriers that can freely oscillate with (and absorb) the incoming radiation and the blueshift of the peak position is linked to the carrier density level. Furthermore, spectral signatures of the photodoping process are visible in the bandgap region too, as shown in **Figure 8a**. The photocharging of MO NCs results in an increase of the optical bandgap, due to the (apparent) rise in the energy needed to promote electrons up to the Fermi level after the filling of CB states. This phenomenon, which is detectable as a blueshift of the absorption edge, is the so-called Moss–Burstein effect[127]. The spectroscopic analysis of plasmon resonances in photodoped MO NCs can be exploited as feedback parameter during potentiometric titration experiments. By monitoring the LSPR (for example, by integrating the intensity of the LSPR or following its peak energy) upon the addition of oxidative molecules is possible to identify the amount of titrants needed to recover the initial (*i.e.,* before photodoping) conditions. With similar techniques is possible to calculate the number of equivalents corresponding to the extra photocharges stored.[16] Further information on the optical modeling of LSPR modulations can be found in **Chapter V**.

The Drude model of bulk materials is widely employed in the description of the plasmonic response of MO NCs and supports well the experiments on homogeneous NCs.[16] Moreover, the energetic band structure of MO NCs is typically assumed to have a flat-band configuration. However, this framework contains strong assumptions that introduce significant limitations relevant at the nanoscale. For example, it is known that inhomogeneous dopant distributions (such as dopant segregation effects) affect the optoelectronic properties of MO NCs in the near-surface region. [20,22] Additionally, Fermi level pinning has been confirmed in tin-doped indium oxide NCs. Surface states (*e.g.,* surface trap states, defects, vacancies, surface ligands, and other bound molecules) which are located energetically below the Fermi level induce an upward bending of the conduction and valence band that extends over several nanometers into the material (**Figure 8b**).[15,20,21,56,76,78,80,103,128] The radial dependency of the conduction band induce

a radial gradient in the carrier density (n_e), with the formation of electronically depleted regions at the NC surface (further details on depletion layers in MO NCs can be found in this chapter). The suppression in carrier density is so intense that the depletion region effectively acts as a dielectric.[20–22,80] Recent studies have linked the electrochemical introduction of extra electrons to a decrease of the electronically depleted layer width.[20,69,96] Surface effects such as depletion layers are expected to be relevant for devices based on NCs networks (*e.g.*, TCO thin films). Due to the high surface-to-volume ratio, the transport properties of similar nanostructures could be significantly affected by externally-induced modulations of carrier density levels. Along this line, Morfa *et al.* reported a conductivity enhancement after UV illumination by a factor greater than two in thin films based on MO nanocrystals.[129] This light-induced modulation could be exploited as a last-stage technique to optimize device performances whenever depletion layers are detrimental for the application needed. By looking at the general picture, the evidence accumulated in recent years suggests that modulations in superficial depletion layers play a key role in the photodoping and energy storage processes. The impact of electronically depleted layers in photodoped MO NCs will be analyzed in detail in **Chapter V**. Furthermore, Fermi energies and band edges are concepts rigorously defined for bulk materials, whose definitions can get blurred at the nanoscale.[130] For example, a variation of a single electron can have significant effects in small systems, causing the nuclear reorganization of the NC structure. This reorganization can trigger a series of concatenated additional effects, such as ion transfer and ion intercalation, surface binding, as well as reorganization effects on the outside of the NC, in the double-layer.[130] Similar ion movements and the interactions between the extra electrons and the charged cations are usually neglected effects in the energy balance of the photocharging, while they could introduce relevant additions.[130] Further investigations of thermochemistry effects and redox reactions at the nanoscale might help unveil important dynamics of photodoped supercapacitors composed of MO NCs.[20] Moreover, carriers introduced by chemical doping are distinguishable from carriers introduced by photodoping and might display a different dielectric response.[131] This is due to the delocalized nature of the excess photoelectrons opposed to the localization of chemical dopants electrons to lattice sites. This aspect might be relevant for applications which rely on the precise determination of stored carriers.[132]

II. 3 Two-dimensional materials

Since the discovery of the thinnest material, Graphene (isolated in 2004, Nobel prize in 2010), layered materials have been the center of a massive research campaign to fabricate novel two-dimensional (2D) materials. In this class of materials, atoms are arranged in flat layers and the layers are stacked on top of each other as paper sheets in a pile. The individual atomically thin layers are weakly bonded together with electrostatic (van der Waals) or hydrogen-bonding interactions.[133] For this reason, it is possible to isolate single layers via mechanical or chemical exfoliation, physically separating individual layers from a bulk crystal (top-down approach). The bottom-up growth of single layers via chemical vapour deposition (CVD) techniques has also been established (further details can be found in **Chapter III**). The systematic nanofabrication of large-area high quality monolayer 2D crystals in a controlled and predictable way is not a trivial task. Nevertheless, recent progress in the mechanical exfoliation of 2D TMDs with gold-mediated techniques significantly improved the monolayers' size, going from the micrometric scale to the centimetre scale.[134]

Bidimensional materials are single layers (1L) that have the thickness of a single atom (*i.e.*, graphene) or a few atoms (*e.g.*, MoS_2, WSe_2, InSe, GaSe, black phosphorus, hexagonal boron-nitride, h-BN). The effort of the scientific community was motivated by the unique physical features they host, often radically different from the three-dimensional version of the same crystal, and whose investigation is of great interest for science and innovation. 2D materials represent a rich playground for studies of novel physical phenomena, such as the propagation of massless Dirac fermions in graphene or the formation of 2D topological insulators.[42,135,136] Moreover, the discovery of superconductivity in twisted bilayers of graphene, when the two monolayers are twisted at a specific angle, inspired the development of a new field of electronics, the so-called twistronics.[137,138] The mechanical, electrical, and thermic properties that 2D materials display are highly diverse and can dramatically outperform those of traditional bulk crystals, opening promising prospects for the development of next-generation devices and advanced functional materials. Depending on the composition, single layers can be conductive (graphene), isolating (h-BN), or semiconducting, as for some of the most studied transition metal dichalcogenides (TMDs). In this Thesis, 2D TMDs have been investigated and coupled with MO NCs.

II. 3.1 2D Transition Metal Dichalcogenides

Transition metal dichalcogenides (TMDs) is a family of layered materials characterized by the formula MX_2, where M is a transition metal atom and X is a chalcogen atom. 2D TMDs have been intensively investigated as bidimensional semiconductors, when composed of molybdenum or tungsten (M = Mo,

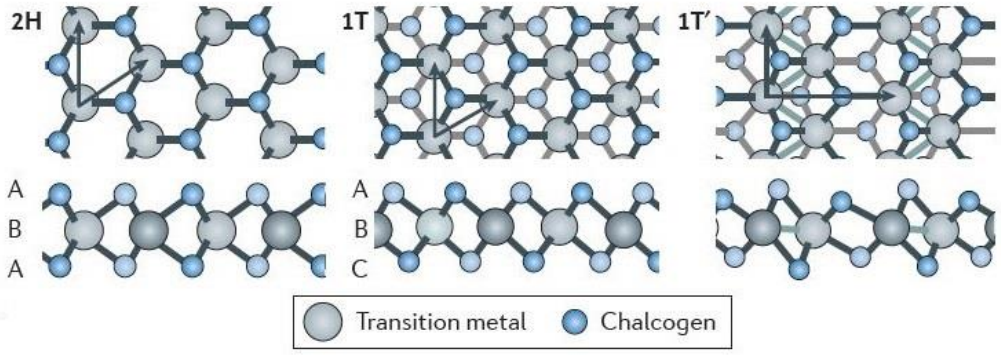

Figure 9 – Typical crystalline structure of TMD single layers. *Based on the atomic configurations, the lattice arrangement of 2D TMDs can be trigonal prismatic (2H), distorted octahedral (1T) and dimerized (1T′). Lattice vectors and the stacking of atomic planes are indicated. Reproduced from Ref.*[26] *with permission from Springer Nature.*

W) and chalcogens such as X = S, Se, Te. In this structure, they present bandgap energies covering the visible and the near-infrared spectral region (1.0–2.1 eV). Some of the most studied 2D materials have bandgaps, which are not suitable for certain optoelectronic applications, such as gapless graphene (Eg = 0 eV) or h-BN monolayer (Eg = 6 eV). The above-mentioned 1L-TMDs, instead, combine the properties of two-dimensional materials, such as the extreme sensitivity to the local environment, mechanical strength, transparency, and flexibility, to the well-known and valuable characteristics of direct-bandgap semiconducting materials.[139–141] In particular, single layer TMDs are extraordinarily sensitive to the surrounding and external stimuli.[142,143] Variations in their electronic structure and optoelectronic properties (*e.g.,* emission spectra) can be locally induced by strain,[144,145] doping,[146] defects,[147–149] vacancies,[150] as well as from the interaction with the substrate.[143]

Single layers of TMDs are formed by three atomic planes vertically stacked as chalcogen-metal-chalcogen. **Figure 9** shows the crystalline structure of 2D TMDs. The thermodynamically stable trigonal prismatic (2H) and distorted octahedral (1T) phases are the most common lattice configurations. In these cases, the atomic arrangement corresponds to an ABA or ABC staking of atomic planes, with the metal atom being at the center (-B-) and chalcogenides located on top and bottom. Distortion can significantly

alter the lattice periodicity, leading to the formation of metal-metal bonds, as in the case of dimerized 1T′ phase. Depending on the structure and the combination of elements employed, the family of 2D TMDs contains a wide variety of optoelectronic features. For example, transport properties can vary from semiconducting, such as for 1L-MoS2, to metallic and semimetallic behaviors (*e.g.*, $NbSe_2$ and WTe_2, respectively).[151,152] A vast number of promising applications in the fields of nanoelectronics, photonics, energy storage, catalysis, sensing, and quantum communications.[29,94,153–159] Several optoelectronic devices have been proposed to exploit the photoluminescence emission of 2D-TMDs, including photodiodes and detectors, photo-transistors, and solar cells.[157,158,160–162]

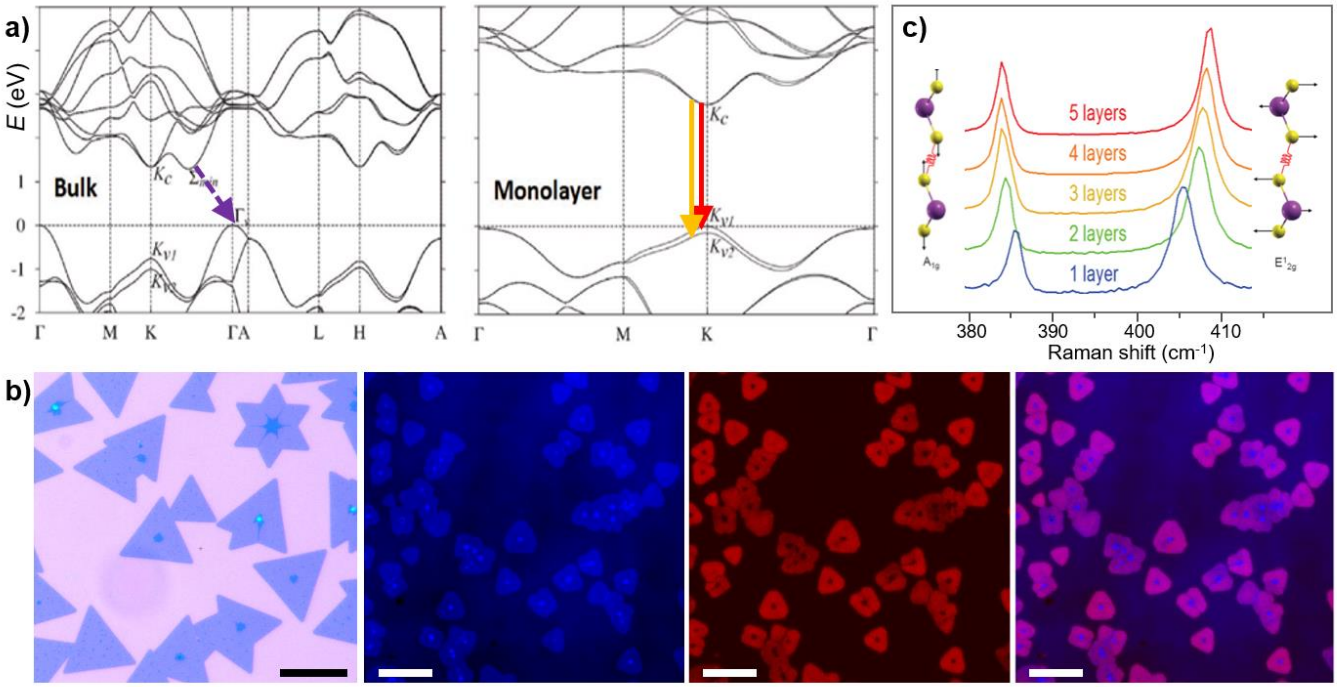

Figure 10 – Single layers of molybdenum disulphide (1L-MoS_2). a) *Variation in the electronic band structure of MoS_2 from bulk (left) to monolayer (right). The indirect band-gap of 3D MoS_2 is depicted in purple while the two direct-bandgap transitions at the K point are highlighted in orange and red. Reproduced with permission.*[163] *Copyright 2012, American Physical Society.* ***b)*** *Evolution of the shape and position of the Raman peaks corresponding to the two modes E^1_{2g} and A_{1g} from 1 to 5 MoS_2 layers. Reproduced with permissions from Ref.* [166]. ***c)*** *From left to right: optical image; reflection map; photoluminescence map; and combined reflection and PL map of two-dimensional CVD MoS_2 flakes. The scale bar is 20 nm.*

In this work, MoS_2 single layers grown via Chemical Vapour Deposition (CVD) were chosen for the assembly of 0D-2D heterostructures. Molybdenum disulfide can be taken as a case-study for 2D

semiconducting TMDs. Reductions in the dimensionality affect the band structure of layered MoS_2 due to different screening and quantum effects (see **Figure 10**). [29,163] Thinning down from bilayer to monolayer, the conduction band minimum moves to the K point of the hexagonal Brillouin zone and the bandgap of MoS_2 transitions from being indirect (as for multi-layer and bulk MoS_2) to direct.[29,163] Spin-orbit coupling effects induce the splitting of the valence band at the K point, generating two bands containing electrons with opposite spins. Because of this, photoluminescence recombination can occur through two channels. Single layer MoS_2 exhibits a strong photoluminescence (PL) emission at ~ 1.8 eV (A emission) and a second weaker emission at ~ 1.96 eV (B emission).[153,164] Remarkably, the optical transitions at the K points are valley selective. Owing to the inversion symmetry breaking, electrons at the K+ and K- band extrema have opposite spin directions and the VB valleys are time-reversal. Hence, the absorption of σ+ and σ- circularly polarized light occurs selectively at the K+ and K- valleys, respectively. The unique combinations of spin and valley degree of freedoms hosted by 2D TMD is employed in the recently-proposed field of valleytronics.[153] Apart from the intense photoluminescence and strong light-matter interactions, single layers of MoS_2 display a long series of advantageous features for optoelectonics applications, such as good mobility values (~ 700 $cm^2 V^{-1} s^{-1}$), tunable bandgap energies, large optical absorption in the visible range (up to 20% per monolayer at specific resonances) and rich excitonic features[157,165]. The indirect-to-direct bandgap transition occurring from bilayer to monolayer can be conveniently exploited to detect and distinguish a single layer from a multi-layered (ML) flake, as the 1L PL is more than 100 times stronger than bilayers' emission. CVD-grown TMDs often present a multi-layer region at the center of the flake, in correspondence with the nucleation site. This translates into a PL drop in this ML fraction of the flake visible with PL mapping, as shown in **Figure 10b** and **Figure 11c**. Another common strategy to characterize 2D TMDs is through AFM thickness measurements or Raman spectroscopy. It is possible to count the number of layers in MoS_2 flakes by looking at the relative position and shape of the Raman peaks corresponding to the two modes E^1_{2g} and A_{1g},[166] as reported in **Figure 10c**.

II. 3.2 Excitonic quasiparticles in MoS_2 monolayers

In a crystal structure, the light-induced promotion of an electron from the valence band to the conduction band leads to the creation of exotic quasiparticles called excitons. An exciton is a bound state formed by an excited electron and the corresponding electron vacancy, electrostatically attracted to each other. Due to Coulomb interactions in the many-body system (*i.e.*, electron-electron repulsive forces), the exciton

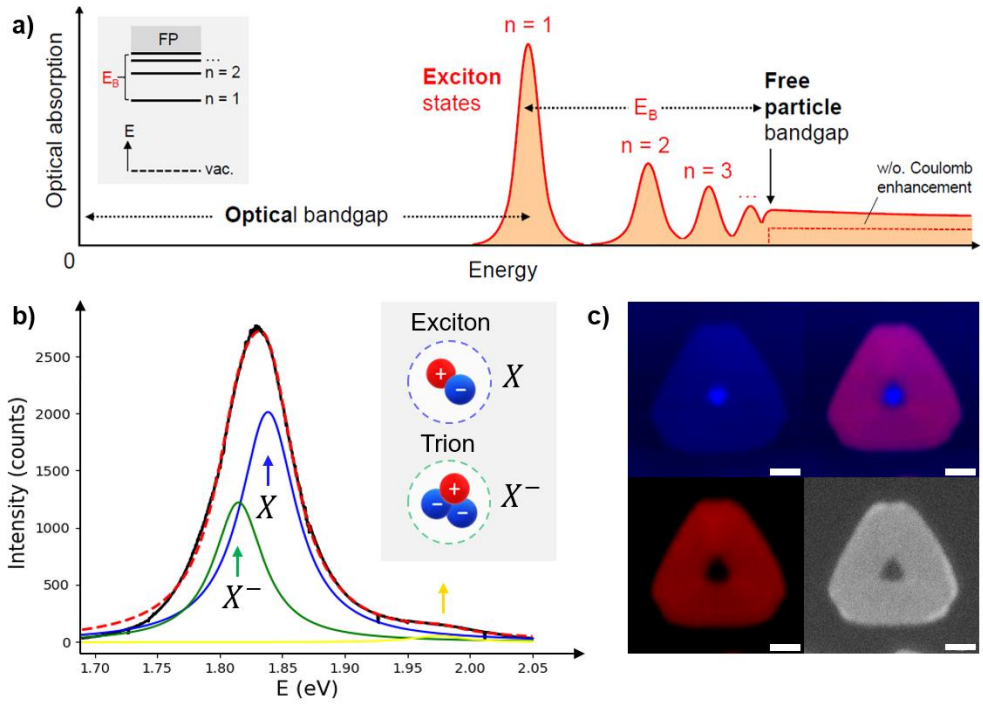

Figure 11 – Photoluminescence emission of single layers of MoS_2. a) *Schematic illustration of the optical absorption of an ideal 2D semiconductor including the series of bright exciton transitions below the renormalized quasiparticle band gap. In addition, the Coulomb interaction leads to the enhancement of the continuum absorption in the energy range exceeding E_B, the exciton binding energy. The inset shows the atom-like energy level scheme of the exciton states, designated by their principal quantum number n with the binding energy of the exciton ground state (n = 1) denoted by EB below the free particle bandgap (FP). Reproduced from Ref.*[153] *with permissions from American Physical Society.* ***b)*** *Photoluminescence spectrum of 1L-MoS_2 deconvoluted with Lorentzian fits corresponding to the A exciton and A trion (in blue and green) and the B exciton (in yellow). The red dashed line shows the resulting fit of the PL spectrum. Inset illustrates a representation of the exciton (X) and negatively charged exciton (trion X^-) quasiparticles.* ***c)*** *Reflection image (top-left) and photoluminescence images (bottom left) of a CVD MoS_2 flake. By overlapping the two images (top-right) it is evident that the center of the flake, composed by multi-layers, does not emit light as strongly as single layer portions on the flake. The bottom-right image reports the PL emission intensity at 1.85 eV, showing inhomogeneities at the edges of the flake. Scale bar is 2.5 µm.*

has lower energy with respect to the corresponding unbound electron and hole. Hence, the formation of an exciton resonance is energetically favorable and strongly influences the optical absorption of ideal 2D semiconductors, lowering their optical bandgap energy (**Figure 11a**). The hole-electron bound pair is an

elementary excitation that behaves like a hydrogen atom confined in the crystal lattice, with net-zero charge and characteristic binding energies, and can be conveniently described as an independent quasiparticle. In condensed matter physics, excitons are typically categorized in Frenkel and Wannier types, based on the binding energy and radius of the hydrogenic resonance. Frenkel excitons are tightly-bound electron-hole pairs, characterized by large binding energies and small excitonic radii (in the order of the Armstrongs). Typically, they originate in systems with low dielectric constants and intense columbic interactions. Frenkel excitons are highly localized, strongly interact with phonons and exhibit low transport properties. On the other hand, Wannier excitons are loosely-bound excitons (~0.01 eV) with large electron and hole orbits in the nanometric order. Wannier excitons are typical of semiconductors with high dielectric screening and small electron effective masses. In 2D-TMDs, features traditionally associated to Frenkel and Wannier excitations coexist, owing to the weak dielectric screening and 2D quantum confinement effects. Excitons in single layer TMDs have large Bohr radii (9.3 Å in the case of 1L-MoS_2), with a wavefunction that can extend over several lattice constants, and large binding energies, in the order of 0.5 eV. Due to significantly strengthened Coulomb interaction in the 2D environment, exceptional excitonic phenomena are observed in 2D TMDs. Single layers of MoS_2 are populated by neutral excitons and excitons bound to other particles such as charged excitons (*i.e.*, trions) and bi-excitons. The resulting formation of excited quasiparticles dominates the fundamental optical properties of 2D TMDs even at room temperature.

In MoS_2 monolayers, the photoluminescence emission spectrum is determined by the recombination of excitons and trions (see **Figure 11b**). Excitons can couple with other free electrons and holes in the lattice, leading to the formation of negatively charged trions (X^-) and positively charged trions (X^+). The binding energies of quasiparticles depend on the effective masses of electrons and holes and are heavily affected by the thickness of the layered crystal. By increasing the number of layers from single layer to bulk, the dielectric screening intensifies and binding energies heavily decrease. In 1L-MoS_2, trions have binding energies of the order of tens of meV. A pronounced trion contribution lowers the average energy of the emission and can be detected by analyzing the PL lineshape. The relative trion and exciton contributions to the photoluminescence spectrum can be measured from the deconvolution of the main peak into two Lorentzian fits, one at higher energies accounting for the neutral exciton and one at lower energies taking into account the negative trion. The thermal equilibrium between excitons, trions and free carriers (with densities of n_X, n_{X-} and n_e, respectively) can be expressed as $n_X + n_e \leftrightarrow n_{X-}$. For low carrier density values, the dynamic equilibrium of free electrons is governed by a Bolzmann

distribution. Mass action models have been developed to calculate the exciton-to-trion ratio in bidimensional materials.[146,167,168] This aspect will be further discussed in **Chapter III** and employed in **Chapter VII**, as a powerful tool to monitor variations in the carrier density of 2D TMDs with spectroscopic analysis.

Manipulation of 1L-TMDs

Many of the main parameters of two-dimensional TMDs, as the interlayer bandgap, exciton energies and populations, are controlled with an external electrical bias. Thus, electrical tuning is a powerful technique to manipulate the optoelectronic properties of these layered materials.[29] Electrostatic gating is the most common design to achieve this goal, with a source and a drain contact on the top of the monolayer and usually collected together to the ground, a dielectric layer immediately underneath the two-dimensional TMDs (*e.g.*, SiO_2, h-BN) and a third contact below the sample and the dielectric, connected to a voltage source. In this architecture, MOS-FET-like, the bias (V_g) is applied from below the sample, as shown in **Figure 12a**. Devices built in this way have shown tunable photoluminescence and control over the excitonic populations in MoS_2 monolayers[139,169] and $MoSe_2$ monolayers[168]. (**Figure 12b**). More advanced possibilities arise from the splitting of the back gate into two separately controllable pads. With a similar architecture, it is possible to induce a p-n junction into the TMD monolayer by applying two different potentials V_{g1} and V_{g2}. As shown in **Figure 12**, photocurrents and localized photoemissions at the junction line have been reported. 2D p-n junctions exhibit an extreme tunability of the optical properties, combined with promising values of light–power conversion and electroluminescence efficiencies. Several studies demonstrated that good control over p-n junctions, fundamental unit of most optoelectronic applications, can be achieved with competitive results, proving that 2D TMDs are promising candidates for the development of the next-generation photodetectors, photodiodes, and solar cells.[170–172]

In recent years, bidimensional materials have been locally manipulated to design innovative devices architectures of particular interest for quantum optics and solar energy conversion, with the proposed creation of solar 'energy funnels'.[142,145,173,174] As introduced before, the optoelectronic properties of 2D TMDs are dramatically affected by local perturbations. Given the extent of modern treatments involved in the assembly of nanodevices (*e.g.*, chemical treatments, high temperatures, electron beam exposure, ion-bombardment), is virtually impossible to avoid the introduction of structural and chemical disorder in 2D materials during the fabrication steps. Local perturbations impact, often negatively, the

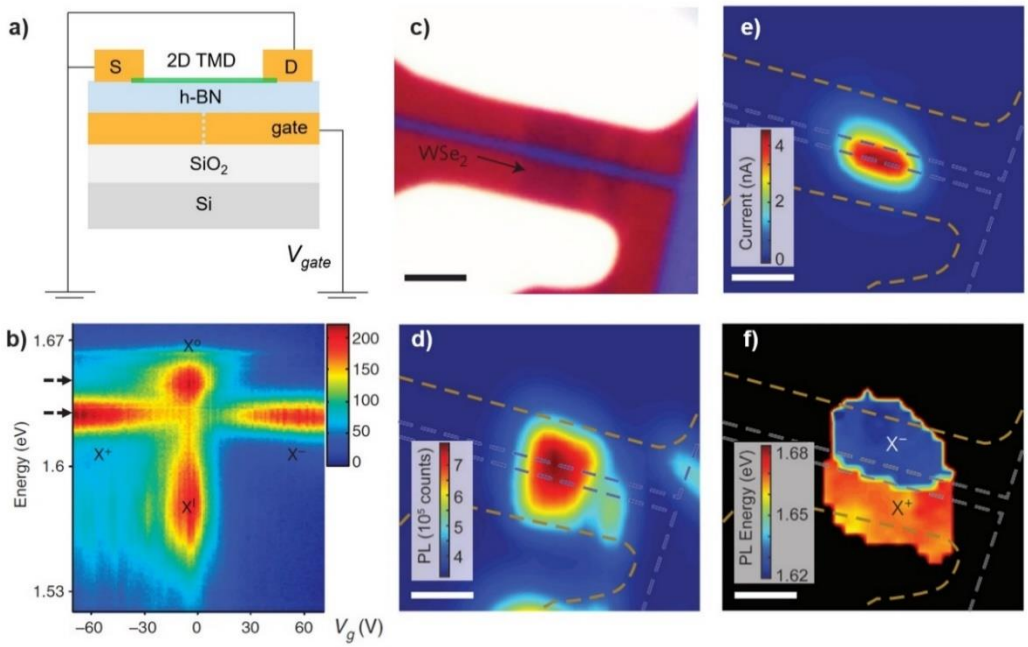

Figure 12 – Electrostatic control of devices based on 2D-TMDs. a) Illustration of a typical gating configuration for electrostatic control of 2D-TMDs. **b)** $MoSe_2$ PL (colour scale in counts) is plotted as a function of back-gate voltage. Near zero doping, we observe mostly neutral and impurity-trapped excitons. With large electron (hole) doping, negatively (positively) charged excitons dominate the spectrum. **c)** Photoresponse of monolayer p–n junction at 100 K. Microscope image of a monolayer p–n junction 1L-WSe2 device. The source and drain contacts are white, the two bottom gates are red, and the BN is blue. **d)** Corresponding Integrated photoluminescence map. The orange dashed lines outline the source and drain contacts whereas the blue dashed lines outline the backgates. **e)** scanning photocurrent image showing pronounced photocurrent generation localized to the junction. **f**) Peak photoluminescence energy map showing p and n regions as a result of the different energies of oppositely charged excitons. X- (X+) represents the negatively (positively) charged exciton found in the n (p) region. Panel b readapted from Ref. [168] with permission and panels c-f readapted from Ref. [170] with permission from Springer Nature.

morphological (*e.g.*, strain) and electronic structure of TMDs.[175] Hence, the investigation of the unperturbed physical and chemical properties of nanomaterials is a topic of scientific and technological relevance. Contactless techniques, such as all-optical techniques, are promising candidates to address this task. Light can be employed to actively manipulate the 2D material, with local modulations including the generation of photocurrents, conductance modulations,[176,177] excitonic Mott transitions[178,179], and negative photoconductivity.[180] To overcome the transient nature of these methods, often circumscribed on ultrafast timescales, photoactive molecules and graphene quantum dots have been recently employed as charge injection sources. Upon illumination, light is absorbed and ~1 photocarrier per molecule is

injected into the TMD layer.[167,181] In **Chapter VII**, I will report the implementation of metal oxide NCs as charge injection sources capable of multi-charges transfers, going beyond the state of the art, and stable long-distance charge separation.

III. Experimental techniques and methods

I report here the techniques employed for the nanofabrication of the materials used in this work and for their morphological and optical characterization. Dynamic modulations were induced via photodoping and via oxidative reactions, under the experimental conditions detailed below. The analysis of the experimental data was supported by a combination of optical modeling (for both absorption and photoluminescence) and numerical simulations. Technical details of the methods utilized in this work are listed below.

III. 1 Fabrication of nanomaterials

Oleic acid (90%), Oleyl alcohol (85%), Tin(IV) acetate (99.99%), In(III) acetate (99.99%), Ethanol (99.8%), Hexane (95%), Toluene (99.8%), Acetonitrile (99.8%), Dimethylformamide (99.8%), $NOBF_4$ (95%) were purchased from Sigma Aldrich.

III. 1.1 Continuous growth of $Sn:In_2O_3$ nanocrystals

Tin-doped indium oxide nanocrystals have been synthesized with a continuous growth approach.[22,55,58] The so-called living nanocrystal growth methods allow determining the radial composition of the NC with nanometric precision, with control over dopants distribution, size dispersions, and the formation of core-shell structures with tailored features.[54] In principle, several precursors with different doping levels can be introduced in the reaction, as no purification of the nanocrystals is required (**Figure 13**). I describe here the step-by-step procedure followed. First, tin(IV) acetate and indium(III) acetate were mixed in a 1:9 Sn:In ratio. Then, oleic acid was added in a 1:6 metal to acid ratio in the same flask, yielding to a 10% Sn-doped ITO precursor solution. Degassing was performed by leaving the flask for 3 hours at 150 ^{0}C under N_2. The nanocrystals were synthesized by slowly injecting the ITO precursor solution via a syringe pump (drop-by-drop at a rate of 0.35 mL/min) to 13.0 mL of oleyl alcohol kept at 290 ^{0}C. The slow-injection procedure was accompanied by a constant flow of N_2 gas in the reaction flask (130 mL/min), washing the reactor from water vapor. The removal of water is necessary to avoid precipitation and allow the growth of spherical NCs. Oleic acid ligands stabilize the nanocrystals during the continuous growth. ITO cores, grown to a radius size of 5.5 nm, were isolated by precipitating with 12 mL of ethanol and centrifuging at 7300 rounds per minute (equivalent to an acceleration of 5540g) for 10 min. The

precipitate was then washed twice more with ethanol and dispersed in hexane to form stable stock solution.

For shelling, the core NCs were reintroduced in fresh oleyl alcohol, after keeping a part of the NC solution for analysis. Analogously with what was described before, a second precursor solution was prepared. For the Sn:In_2O_3-In_2O_3 core-shell NCs analyzed in this work, an (undoped) indium oleate precursor solution was formed by mixing indium(III) acetate with oleic acid in a 1:6 molar ratio. The same slow-injection procedure was implemented to add the precursor to the reaction flask. Core-shell NCs were then washed with ethanol and stored for experiments. The shelling process was repeated several times until a final size of ~10 nm was reached. Nanocrystal core-shell samples used in this work were collected at different stages of the shell growth, they present various shell thicknesses but they all share the very same ITO core.

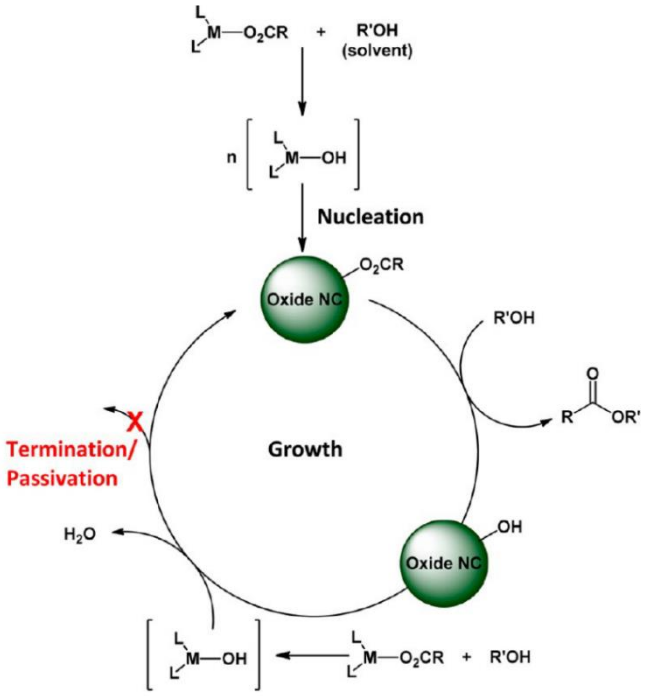

Figure 13 – Schematic illustration of the continuous growth synthesis of metal oxide nanocrystals. *Slow addition of metal oleate promotes metal hydroxide formation leading to initiation of nanocrystal growth. Nanocrystals continue to grow during propagation as additional monomer is added. Metal hydroxyls on the nanocrystal surface support a living growth mechanism. Reproduced with permission from Ref* [55]*. Copyright 2016 American Chemical Society.*

III. 1.2 Chemical vapor deposition of 2D TMDs

Single layers of MoS_2 were prepared employing chemical vapor deposition (CVD) techniques.[17,182] Preliminary cleaning of the chamber from contaminations was performed by base pressure (18mTorr) for 5 mins. Then, in two hot zones of the horizontal furnace (2'' tube diameter) were collocated 2 mg of MoO_3 powder (Sigma Aldrich, 99.97%) and 200 mg of sulfur powder (Sigma Aldrich, 99.998%). Argon (100sccm) was used as carrier gas during the material growth. For nucleation, the MoO_3 and the substrate in the chamber are heated up to 550 °C for 2 mins. The S powder is heated at 130 °C by a heat tape enveloped outside the furnace. Finally, the chamber temperature is raised to 725 °C for 15 mins, and the powders are kept at 130 °C. The as-prepared sample is composed of single layers of MoS_2 distributed over a SiO_2/Si standard wafer. The dielectric layer of silicon oxide, with a thickness of ~280 nm, provides optical contrast.

III. 1.3 Nanofabrication of 0D-2D hybrid heterostructures

The 0D-2D hybrid heterostructure was fabricated by spin-coating a single layer of ITO-In_2O_3 nanocrystals on top of the 2D MoS_2 sample. Spin-coating was performed by depositing 20 μL of a 10mg/mL NC/toluene solution at 2000 rounds per minute (rpm) for 45 seconds, with a ramping time of 10 seconds. Subsequently, a thin protective layer of polymethyl methacrylate was deposited to encapsulate the heterostructure. 50 μL of a 5mg/mL stock solution were spin-coated at 2000rpm for 45 seconds, resulting in a polymer protection layer of approximately 50-100 nm. SEM imaging confirmed the presence of a single layer (or a bilayer) of NCs covering the 2D flakes. The characterization of the MoS2 monolayers via Raman spectroscopy and micro-PL mapping, before and after the deposition of MO NCs, showed no significant variations in the optical properties nor the morphological structure of the single layers.[17,18]

III. 2 Characterization techniques

For the structural and optical characterization of the nanomaterials involved in this work, several techniques were implemented, mostly involving microscopy (*e.g.*, optical microscopy, electron microscopy) and spectroscopy (*e.g.*, Raman, photoluminescence, absorbance).

III. 2.1 X-Ray diffraction (XRD) and X-Ray photoemission spectroscopy (XPS)

X-ray Diffraction (XRD) measurements were performed with a PANanalytical Empyrean X-ray diffractometer equipped with a 1.8 kW Cu Kα ceramic X-ray tube and a PIXcel3D 2x2 area detector, operating at 45 kV and 40 mA. Samples were prepared by depositing a concentrated NCs solution onto a zero-diffraction silicon substrate and letting the solvent evaporates. XRD diffraction patterns were collected in a parallel beam geometry with symmetric reflection mode, working under ambient conditions. Data analysis of the XRD data was implemented with the HighScore 4.1 software from PANalytical. XRD measurements confirmed the crystalline structure of ITO NCs.

X-ray Photoemission Spectroscopy (XPS) measurements were carried out on a Kratos Axis Ultra^{DLD} spectrometer equipped with a monochromatic Al Kα source (15 kV, 20 mA). Samples were prepared by dropping a concentrated NCs solution onto a highly ordered pyrolytic graphite (HOPG, ZYA grade) substrate and letting the solvent evaporates. To collect high-resolution spectra (energy step = 0.1 eV) of the Sn *3d* and In *3d* regions a 10 eV pass energy was employed over a 300 x 700 microns area. Photo-emitted electrons were collected at a take-off angle of $\phi = 0°$ with respect to the surface normal and the analysis chamber pressure was kept below 7×10^{-9} Torr for data acquisition. XPS data were converted to VAMAS format and data processing was performed with the CasaXPS software, version 2.3.24. The C *1s* peak was used as internal reference for the binding energy scale (BE for C–C = 284.8 eV). Quantitative analysis of the tin and indium contributions was performed by calculating the areas of In *3d* and Sn *3d* peaks, following the implementation of background correction methods across the spectral range analyzed. Relative sensitivity factors (RSF) were used to scale the peaks areas and estimate the relative atomic concentration of indium and tin, as provided by Kratos ($RSF_{In\ 3d}$ = 7.265, $RSF_{Sn\ 3d}$ = 7.875).

III. 2.2 Inductively-coupled plasma mass spectrometry (ICP-OES)

Inductively coupled plasma mass spectrometry (ICP-OES) was employed to estimate the doping levels and the NC concentrations for all core-shell ITO samples. The elemental analysis was performed on an iCAP 6000 Series ICP–OES spectrometer (Thermo Scientific). The sample preparation process employed is the following. To completely digest the NCs, the samples were dissolved in aqua regia [HCl/HNO_3 3:1 (v/v)] in a volumetric flask left overnight at room temperature. Milli-Q grade water (18.3

MΩ cm) was then added to the flask and the obtained solution was filtered with a polytetrafluorethylene membrane (0.45 μm pore size) filter. For the ICP-OES analysis reported, a systematic error of about 5% can be expected.

III. 2.3 Optical absorbance measurements

Absorbance measurements were carried out on a UV−vis−NIR Spectrometer (Agilent Cary 5000) in the spectral range 280-3200 nm with a scan resolution of 1 nm. For both photodoping and titration experiments reported in this work, sample preparation required the drying of the solvent (hexane) and the transfer to ITO NCs into anhydrous toluene in a nitrogen-filled glove box. Optical measurements were performed in transmission using an anaerobic rectangular cuvette with a sealed screw cap (Starna Scientific), with an optical path of 5 mm and a volume of 1.4 mL. As reference spectrum, the same cuvette was measured when filled only with the solvent.

III. 2.4 Electron microscopy (TEM and SEM)

Transmission electron microscopy (TEM) was employed with a JEOL JEM-1400Plus operating at 120 kV to morphologically characterize the samples of varying shell thicknesses, estimate the particles size, and validate the successful formation of nanocrystals. Samples were deposited on lacey carbon grids supported by a copper mesh. Size distribution analysis was performed using ImageJ tools on the images acquired. High-resolution TEM (HR-TEM) was performed with an image-Cs-corrected JEOL JEM-2200FS TEM (Schottky emitter) operating at 200 kV, with an in-column image filter. For sample preparation, NCs were deposited onto double amorphous carbon film -ultrathin on holey- coating Cu grid. High-resolution images were collected in electron-counting mode with a direct electron detection camera (K2 Summit, Gatan), further confirming the crystalline NC morphology.

Scanning electron microscopy (SEM) was employed to characterize the ITO NC thin film covering the MoS_2 layer in the hybrid heterostructure and estimate the NC areal density. The SEM imaging was carried out with a Helios Nanolab 600 (FEI Company) combined with an X-Max detector, using an accelerating voltage of 10 kV and beam current of 0.2 nA.

III. 2.5 Hyperspectral imaging (micro-PL and micro-Raman spectroscopy)

Hyperspectral imaging was achieved by collecting the photoluminescence (PL) spectrum and Raman spectrum of 1L-MoS_2 in each spatial point of the map, raster-scanning the 2D flake with high-precision piezo stages (Mad City Labs). The sample was probed with a 500 nm pulsed laser excitation source (2.48 eV; 80 MHz repetition rate) by using a scanning confocal microscope equipped with a 50×0.6 NA objective. The same objective collected the emission spectrum of the sample, filtering out the excitation light reflected from the laser with a 600 nm long-pass filter and a 532 nm long-pass dichroic mirror. Then, the output signal was dispersed with a spectrometer (Princeton Instruments) and acquired by a cooled charge coupled device (CCD) camera (Andor). Emission data were acquired with custom-made microscopy software.[183] The laser power employed was kept, for all measurements, low enough to remain in the linear regime response of the sample and avoid non-linear optics effects. For Raman measurements, a specific microscope system (NTMDT) and an excitation wavelength of 532 nm (2.33 eV) were implemented analogously as above.

III. 3 Post-synthetic modulation techniques

III. 3.1 Photodoping of colloidal NCs

For the photodoping of colloidal NCs in solution, the following procedure was followed. ITO nanocrystals were prepared by collecting an aliquot of the stock solution in hexane, letting the nanoparticles dry and transferring them into an argon-filled glovebox. Then, the NCs were dispersed in toluene anhydrous, forming a colloidally stable solution of concentration. The use of anhydrous solvent is motivated by the need for inert atmosphere conditions of the photodoping process occurring in a liquid environment. Photodoping is achieved by illuminating the quartz cuvette containing the NC solution with a UV LED (Thorlabs M300L4, central wavelength: 300 nm, bandwidth: 20 nm). The cuvette was kept at 12 mm of distance from the UV source, receiving a power density of 36.8 mW cm^{-2} at the cuvette surface. In the case of the solid-state heterostructure, contactless photodoping of the ITO NCs was performed by focusing a 350 nm (3.54 eV) pulsed laser onto a precisely located spot of the hybrid for a few minutes (*e.g.*, 5 or 10 minutes, depending on the specific experiment).

III. 3.2 F4TCNQ titration

Powder (97%) of 2,3,5,6-tetrafluoro-7,7,8,8-tetracyanoquinodimethane (F4TCNQ) was purchased from Sigma-Aldrich. The titrant solution was prepared inside an argon-filled glovebox by dissolving 0.34 mg of F4TCNQ in 40 mL of anhydrous toluene. Before titration, the ITO-In_2O_3 NCs were dispersed in anhydrous toluene (forming a solution of concentration $\sim 0.1 \cdot 10^{-9}$ mol/L), as described above. To preserve the photocharged state of ITO NCs and avoid air exposure, after photodoping, titration additions steps were performed inside the glovebox environment. The effects of F4TCNQ molecules on as-synthesized ITO-In_2O_3 samples were tested, showing no sign of interaction nor degradation. Electron counting was performed by analyzing the neutral, anion, and dianion spectral features of F4TCNQ molecules after each titration step, as described below.

III. 3.3 Electron counting with F4TCNQ titrants

The number of electrons extracted per photodoped NC was estimated by implementing the following procedure. Knowing the concentration of titrant solution ($c = 0.085$ mg/mL) and the molecular mass of F4TCNQ molecules (276.15 g/mol), the volume of titrant molecules added into the cuvette (V) can be easily converted into moles of F4TCNQ (n_{F4TCNQ}) for each step of the experiment: $n_{F4TCNQ}(V) = cV/276.15$ (see **Table 1** in **Appendix**). The mean weight of ITO NCs, estimated from the volume of the unit cell (1.0355 nm^3), the weight of Sn, In and O atoms and the average radius of the NCs measured with TEM images, was employed to calculate the number of ITO NCs moles (n_{NC}) present in solution. Then, by normalizing n_{F4TCNQ} over n_{NC}, the number of reacted F4TCNQ molecules per NC can be obtained: $n_{reacted}(V) = n_{F4TCNQ}(V)/\, n_{NC}$. Depending on the kind of reaction taking place (identified from dianion or anion peaks), $n_{reacted}$ can be converted in equivalent electrons by multiplying $n_{reacted}$ to a factor two (dianion) or one (anion). The analysis performed in **Chapter VI** indicates that up to $V_1 = 14\ \mu$L (volume of added F4TCNQ molecules) only dianion reactions occur, given the lack of neutral and anion spectral signatures. The next addition, here marked as $V_2 = 17\ \mu$L, is a threshold value in the titration steps in correspondence of which anion and neutral spectral signatures start to appear. The progressive growth of anion and neutral peaks after V_2 indicate that a non-complete reaction of F4TCNQ molecules occurs, making the analysis too complex to be carried on. Nevertheless, the LSPR peak continues to decrease in intensity and its energy redshifts, suggesting that further charge extraction is possible. Here, a transfer of two electrons per F4TCNQ molecule was considered up to the midpoint

between V_1 and V_2 ($Vmid = \frac{V1+V2}{2}$ =15.5 μL). Due to the presence of anion peaks, it is safe to assume that the extraction process of stored electrons continue up to at least V_2. To account for this, one extra electron was then added for each titrant molecule between $Vmid$ and V_2. Hence, the total number of electron extracted from each photodoped NC was estimated as: $2e^- \times n_{reacted}(V_{mid}) + 1e^- \times (n_{reacted}(V_2) - n_{reacted}(V_{mid})) \approx 123$.

III. 4 Optical modelling and numerical simulations

III. 4.1 Numerical calculations of Poisson's equation

Simulations for the energy band and carrier density profiles of MO NCs with spherical symmetry were performed using a finite-element method (FEM). The solution to Poisson's equation was numerically calculated with the software COMSOL Multiphysics v5.0 (Comsol Inc., Burlinghton MA USA), exploiting the built-in *Mathematics module.*

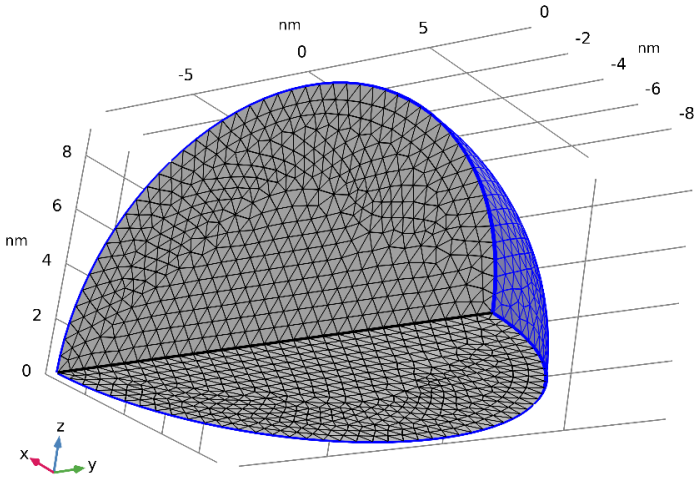

Figure 14 – Meshed geometry of a spherical nanocrystal. *Poisson's equation was solved over this control volume using a finite element method in COMSOL. Reproduced from Ref.*[23] *with permission from Springer Nature.*

The dimensionless form of Poisson's equation was adapted in Cartesian coordinates, as derived by Seiwatz and Green:[20,22,84]

$$\nabla^2 u = -\frac{\rho \cdot e^2}{\varepsilon \varepsilon_0 k_B T} \quad (10)$$

where e is the fundamental electron charge, ε_0 is the vacuum permittivity, ε is the static dielectric constant, k_B is the Boltzmann constant, T is temperature, and ρ is the carrier density. Here, u is the non-dimensional potential describing the difference between the neutral (bulk) and the surface potentials, defined as:[84]

$$u = u_{bulk} - u_{surface} = \frac{E_F - E_I}{k_B T} \tag{11}$$

with E_F being the bulk Fermi energy level and $E_I = \frac{E_{CB}+E_{VB}}{2}$ the band gap midpoint (E_{CB} and E_{VB} represent the conduction band and valence band profile, respectively). Poisson's equation can be rewritten by explicating the contributions to the carrier density profile $\rho = \rho(r)$:

$$\rho = \rho_D(r) + p - n \tag{12}$$

Here, $\rho_D(r)$ is the radially-dependent donor dopant density, and p and n are the hole and electron density contributions, respectively. By employing an auxiliary function $w_{x,y} = \frac{E_x - E_y}{k_B T}$, it is possible to further define the donor carrier density profile, expressing the activated dopant concentration as:

$$\rho_D(r) = \frac{N_D(r)}{1+2e^{(u-w_{D,I}(r))}} \tag{13}$$

where $w_{D,I} = \frac{E_D - E_I}{k_B T}$ and E_D is the donor energy level.

Furthermore, by assuming a parabolic CB and Fermi-Dirac distributions ($F_{1/2}$) for the carriers, the free hole (p) and free electron (n) densities are given by:

$$p = 4\pi \left[\frac{2m_h k_B T}{h^2}\right]^{3/2} F_{1/2}\big(w_{V,I}(r) - u\big);$$

$$n = 4\pi \left[\frac{2m_e k_B T}{h^2}\right]^{3/2} F_{1/2}\big(u - w_{C,I}(r)\big) \tag{14}$$

with h being the Planck's constant, $w_{V,I} = \frac{E_{VB} - E_I}{k_B T}$, $w_{C,I} = \frac{E_{CB} - E_I}{k_B T}$, and $F_{\frac{1}{2}}(\eta) = \int_0^\infty \frac{x^{1/2} dx}{1+e^{x-\eta}}$, where x is the dummy variable. Theoretically, the upper limit of the integral is set to ∞ to account the exponential decay of the integrand at high energies. In the numerical calculation performed, the upper bound was set to a finite number great enough to ensure the solution convergence and maintain an accuracy within the 1% limit.

Considering all of the above, Poisson's equation becomes:

$$\nabla^2 u = -\frac{e^2}{\varepsilon\varepsilon_0 k_B T}\left\{\frac{N_D(r)}{1+2e^{(u-w_{D,I}(r))}} + 4\pi\left[\frac{2\ {}_h k_B T}{h^2}\right]^{3/2} F_{1/2}\left(w_{V,I}(r)-u\right) - 4\pi\left[\frac{2m_e k_B T}{h^2}\right]^{3/2} F_{1/2}\left(u - w_{C,I}(r)\right)\right\} \quad (15)$$

where m_h is the effective hole mass (0.6 times greater than the electron mass) and m_e is the effective electron mass (0.4 times greater than the electron mass).

Introduction of extra charges

Equation (15) was then extended to study the photodoping process of MO NCs. By considering additional generation and recombination mechanisms the Poisson's equation becomes:[184]

$$\nabla^2 u = -\frac{\rho\cdot e^2}{\varepsilon\varepsilon_0 k_B T} + G(r) - R(r) \quad (16)$$

Recombination effects are neglected and $R(r)$ is set to zero. The generation term $G(r)$ represents the spatial distribution of the extra photogenerated carriers introduced into the system and is here modeled by the Gaussian function:

$$G(r) = \frac{N_{max}}{V}\frac{1}{\sigma\sqrt{2\pi}} e^{\frac{r-R_{NC}}{\sigma}} \quad (17)$$

where N_{max} is the maximum (peak) number of extra electrons introduced via photodoping and σ is the shape factor determining the spatial distribution into the nanocrystal. Variations in σ offer the possibility to model different effects of the additional electrons on the energy profile.

Calculations of the number of stored electrons

By integrating the electron density over the NC volume (V), the total number of free electrons can be obtained:

$$N_E = \int_V n(r)dV \quad (18)$$

The number of stored electrons via photodoping (ΔN) is then given by the difference in N_E after photodoping and N_E of the as-synthesized case. I report here that numerical simulations tend to underestimate ΔN for small values of t_s in core-shell systems. However, the error is within uncertainties

expected for this model and the general trend is found to be consistent with experimental findings, as reported in **Chapter VI.**

Optical simulations

To numerically simulate the absorption spectra of ITO-In_2O_3 NCs (shown in **Chapter V**), the radially-dependent solution of Poisson's equation for the carrier density profile was coupled with the high-frequency formulation of Maxwell's equations, linking the simulated electronic density of the NC to its plasmonic response. Optical simulations were performed in Comsol with the *Electromagnetic Waves, Frequency Domain* module. To compute far-field contributions, a background medium box with a size 10 times larger than the nanoparticle radius was added.

III. 4.2 Carrier density analysis from 2D MoS_2 photoluminescence emission

Quantitative analyses of the emission response of 1L-MoS_2 were performed by fitting the PL spectrum with Voigt functions based on a Lorentzian and Gaussian convolution:

$$\mathcal{V}(E,\sigma,\gamma) = \frac{Re[w(\frac{E+i\gamma}{\sigma\sqrt{2}})]}{\sigma\sqrt{2\pi}} \tag{19}$$

where w is the Faddeeva function, γ is the half-width at half-maximum (HWHM) of the Lorentzian, and σ is the Gaussian standard deviation. The PL emission was modeled as the sum of two oscillators, representing the exciton and the trion contributions:

$$I(E) = I_X \cdot \mathcal{V}(E - E_X, \sigma_X, \gamma_X) + I_T \cdot \mathcal{V}(E - E_T, \sigma_T, \gamma_T).$$

$$I(E) = I_X \cdot \frac{Re\left[w\left(\frac{E-E_X+i\gamma_X}{\sigma_X\sqrt{2}}\right)\right]}{\sigma_X\sqrt{2\pi}} + I_T \cdot \frac{Re\left[w\left(\frac{E-E_T+i\gamma_T}{\sigma_T\sqrt{2}}\right)\right]}{\sigma_T\sqrt{2\pi}} \tag{20}$$

where γ_X and γ_T are the HWHM of the Lorentzian peaks, σ_X and σ_T the standard deviations of the Gaussian peaks, I_X and I_T are scaling factors for the overall intensity, and E_X and E_T are related to the center position of the two oscillators. Here, the labels X and T refer to the exciton and trion contributions, respectively, for all the parameters listed above. Importantly, the initial undoped 1L-MoS_2 spectrum was fitted to extract the above fitting parameters used as restrained in the fitting procedure of photodoped spectra, as summarized in the **Appendix**.

The spatial-dependent spectral fit performed for the hyperspectral mapping was performed in an analogous way, keeping the parameters of each pixel fixed from before and after photodoping cases. Finally, Raman peaks were fitted with a Lorentzian function for each peak.

Mass Action Model for quasiparticles

As reported, the emission intensity of the low-energy trion relative to the neutral exciton is acutely sensitive to the density of free carriers in the 1L-MoS_2.[139,146,167,168] Hence, quantitative analyses of the relative populations of tightly bound excitons and trions deliver a non-invasive tool to identify carrier density variations. A modified mass action model was employed to link the free carrier density to the ratio between the spectral weight of the exciton and the trion at room temperature. For low excitation densities, the thermal equilibrium between excitons, trions and free carriers (of densities n_X, n_{X-} and n_e, respectively) can be expressed as $n_X + n_e \leftrightarrow n_{X-}$ and is governed by a Bolzmann distribution. Such model was originally developed to describe carrier density variations in conventional epitaxial quantum well structures[185,186] and was recently adapted to estimate the exciton-to-trion ratio of 2D TMDs (e.g. 1L-MoS_2 and 1L-$MoSe_2$).[146,167,168] In this work, the mass action model describes temporal evolutions in carrier density induced by photodoping. Precisely, the temporal evolution of carrier density, n_e (*t*), can be is described as:

$$n_e(t) = \frac{n_{X-}(t)}{n_X(t)} \cdot \frac{4M_{X_0} m_e}{\pi\hbar^2 M_{X-}} \cdot k_B T \cdot e^{\left(-\frac{E_B^{X-}}{k_B T}\right)} \quad (21)$$

where m_e is the electron effective mass, M_{X_0} and M_{X-} are the exciton and trion effective masses, respectively, and E_B^{X-} is the intrinsic trion binding energy (taken from Ref.[139]).

III. 4.3 Drude-Mie fitting model for plasmonic NCs

An optical model based on Drude theory and Mie scattering theory was intensively employed in this work for the analysis of plasmonic NCs and their modulations upon photodoping. Here, I report details of the fitting procedure. As introduced in **Chapter I**, the Drude-Lorentz complex dielectric permittivity is given by:

$$\varepsilon(\omega) = \varepsilon_\infty - \frac{\omega_P^2}{\omega^2 + i\omega\Gamma} \quad (22)$$

where ω_p is the bulk plasma frequency:

$$\omega_p = \sqrt{n_e e^2/\varepsilon_0 m^*} \tag{23}$$

with n_e being the free carrier density, m^* the effective electron mass, e the unit of elementary charge, and Γ the damping parameter.

For heterogeneous NCs, the expression above is affected by different materials and their geometrical disposition within the particle volume. The Maxwell-Garnett effective medium approximation was successfully applied to model the optical response of core-shell structures through the implementation of an effective dielectric constant, $\varepsilon_{eff}(\omega)$.[187] For core-shell NCs, the formula yields to:

$$\varepsilon_{eff}(\omega) = \varepsilon_{shell}\left(\frac{(\varepsilon_{core}+2\varepsilon_{shell})+2F(\varepsilon_{core}-\varepsilon_{shell})}{(\varepsilon_{core}+2\varepsilon_{shell})-F(\varepsilon_{core}-\varepsilon_{shell})}\right) \tag{24}$$

Where ε_{core} and ε_{shell} are the dielectric permittivity of the core and shell material, respectively, and $F = (R_{core}/R)^3$ is the volume ratio between the volume of the core (V_{core}) and the total volume of the NC (V_{NC}). Both ε_{shell} and ε_{core} are calculated with equation (22). This model was further refined for large core-shell NCs in **Chapter V**, leading to the formulation of the three-layer model. As a matter of fact, recursive applications of equation (22) can lead to the calculation of multiple core-shell structures (*i.e.*, core-multishell systems). In the case of core-shell NCs composed of two materials and a third layer (*DL*) accounting for the depletion layer, the effective dielectric constant can be written as:

$$\varepsilon_{eff1}(\omega) = \varepsilon_{shell}\left(\frac{(\varepsilon_{core}+2\varepsilon_{shell})+2F_1(\varepsilon_{core}-\varepsilon_{shell})}{(\varepsilon_{core}+2\varepsilon_{shell})-F_1(\varepsilon_{core}-\varepsilon_{shell})}\right);$$

$$\varepsilon_{eff}(\omega) = \varepsilon_{DL}\left(\frac{(\varepsilon_{eff_1}+2\varepsilon_{DL})+2F_2(\varepsilon_{eff_1}-\varepsilon_{DL})}{(\varepsilon_{eff_1}+2\varepsilon_{DL})-F_2(\varepsilon_{eff_1}-\varepsilon_{DL})}\right) \tag{25}$$

where $\varepsilon_{eff1}(\omega)$ is the effective dielectric constant considering only the core-shell structure without the depletion layer, $F_1 = (R_{core}/(R_{core}+t_s))^3$ is the volume ratio between V_{core} and $V_{core+shell}$, $F_2 = ((R_{core}+t_s)/R)^3$ is volume ratio between $V_{core+shell}$ and V_{NC}, and ε_{DL} is the dielectric permittivity of the depletion layer. For electronically depleted layers, equation (22) simplifies to $\varepsilon_{DL}(\omega) = \varepsilon_\infty$ being the plasma frequency of the depletion layer null ($\omega_{p,DL} = 0$ since $n_e = 0$). In the **Appendix**, I report the electronic parameters extracted by the fitting of the LSPR resonances, before and after photodoping, with the three-layer model.

LSPR spectra simulated with the optical model

The three-layer model was implemented for simulating the evolution of the LSPR shape of various MO NCs too, as reported in **Chapter V**. In these cases, the structural parameters were chosen to match the core size and shell thickness of the NC under study and the electronic profile systematically tuned to replicate the experimental trends. Several combinations of carrier density levels and spatial extents of the three layers (*L1*, *L2*, *DL*) have been investigated, finding that the modulation of the DL layer is a necessary condition for the observed trends. For each step of the photodoping process, or of the shell growth process, simulations were performed by fixing the total amount of electrons and allowing the redistribution of carriers in the three layers.

IV. Photodoping of metal oxide nanocrystals

A very promising property of doped metal oxide (MO) nanocrystals (NCs) is the ability to store multiple free electrons in their conduction band. Remarkably, this process can be triggered with light in the so-called photodoping process (more details on the accumulation process and related plasmonic modulations of MO NCs can be found in **Chapter II**). Specifically, the term photodoping indicates the light-induced doping process resulting in the variation of the number of conduction band electrons after the absorption of photons. In the n-type doping of NC solutions, the photogenerated holes are quenched at the surface of the NC by electrochemical reactions or transferred to hole acceptors, while the corresponding photogenerated electrons accumulate within the NC volume. Photodoping is a powerful tool that allows the remote non-destructive modulation of carrier density levels in situ, and it has been successfully employed in several semiconductor nanocrystals.[14,15] For example, in order to investigate carrier-dopant interactions, photodoping was efficiently utilized to produce and control electron spins in magnetic semiconductor NCs.[188] In CdSe nanocrystals, n-type photodoping have been exploited to raise the amount of doping and fill quantized energy levels.[14] Photodoping can be employed to alter and control hot electron dynamics in similar NCs.[121] Due to narrow valence bands, cadmium chalcogenide nanocrystals necessitate the employment of highly reactive hole quenchers for efficient photodoping.[14] However, the quantized energy levels of Cd-based chalcogenides significantly restrain the number of electrons that can be introduced via photodoping (*e.g.*, two extra electrons per NC), limiting the implementation of photodoped CdSe NCs for most applications.[14] Instead, metal oxide nanocrystals have been described as soluble supercapacitors due to the ability to accumulate multiple electrons in their conduction bands.[14,15] A number of stored photocharges ranging from tens[16,189] to hundreds[14,78] have been reported for each NC unit. The large capacitance values combined with the possibility of light-induced charging make MO NCs an extremely attractive material for developing light-driven energy storage solutions.[14,15] In fact, in a pioneering work of Brozek *et. al.* on Fe-doped ZnO NCs ($Zn_{0.99}Fe_{0.01}O$) volumetric and areal capacitance values of 233 F cm^3 and 33 μF cm^{-2}, respectively, have been extracted.[14] Those values, achieved via photodoping, compete with those of state-of-the-art supercapacitors commercially available and motivate the research on MO NCs for light-driven energy storage applications.[14] Furthermore, the photodoping of MO NCs has been successfully transferred from solution environments into all-solid-state architectures, with the additional benefit of collecting the photogenerated holes.[17,18] These promising features have been discussed only in recent years and the

photodoping scheme of MO NCs has not been yet transferred to fully-operating technologies, such as light-driven functional devices and energy storage solutions (*e.g.*, MO NCs-based photocapacitors).

Chapter II provided a detailed introduction of the light-driven charging of metal oxide nanocrystals, with a summary of the most important physical and chemical aspects involved in the photodoping process. In this chapter, Indium Tin Oxide (ITO) NCs, synthesized in a core-shell architecture, are taken as a case study and the effects of photodoping are experimentally investigated. A detailed theoretical analysis of the experimental results here introduced will be reported in **Chapter V**, together with new insights on the physics of the photodoping process.

IV. 1 ITO-In_2O_3 core-shell systems

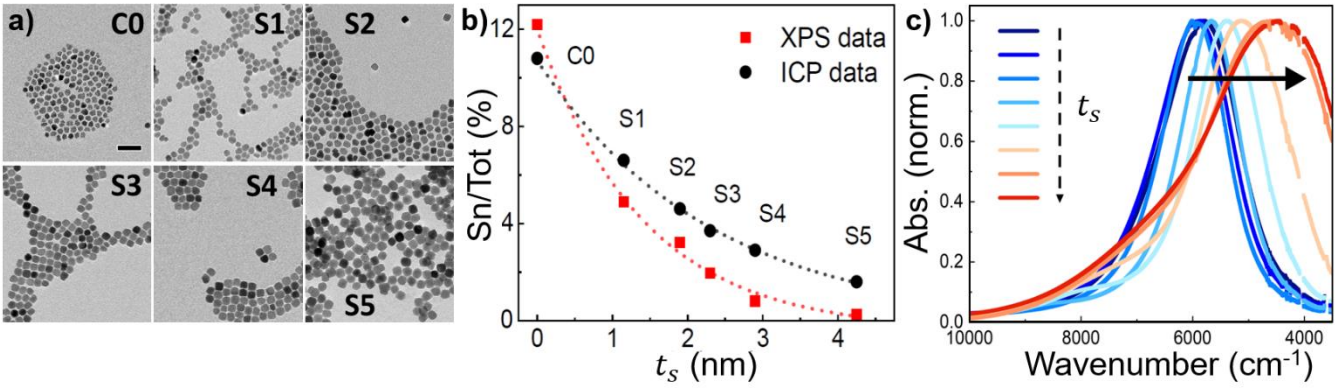

***Figure 15 - ITO-In_2O_3 core-shell colloidal nanocrystals**. **a)** TEM images of the nanocrystals at different stages of the synthesis. Starting from an aliquot of the core (C0) layers of In_2O_3 progressively form a thicker shell around the ITO nuclei (S1-S5). Scale bar is 50 nm for all panels. **b)** Comparison between the Sn-dopant concentrations obtained from inductively coupled plasma mass spectrometry (ICP-OES) and X-ray Photoelectron Spectroscopy (XPS) as a function of shell thickness (t_s). The higher Sn/Tot values of the volume-sensitive ICP-OES measurements with respect to the surface-sensitive XPS measurements indicate that Sn atoms are segregated in the NC core upon shell growth. Dashed lines are to guide the eye. **c)** Normalized absorbance of typical ITO-In_2O_3 core-shell samples with increasing shell size, with a t_s ranging from 0 nm (black line) to 2.3 nm (red line). After an initial blue-shift due to the activation of dopants, growing an undoped shell continuously redshifts the energy of the localized surface plasmon resonance (LSPR) peak in the NIR. Figure adapted from Ref.[23] with permission from Springer Nature.*

The investigation of the photodoping process of MO NCs requires control over many parameters involved, including the NC geometry, size, and doping levels. In this work to experimentally investigate

the photodoping of these system, I synthesized ITO-In_2O_3 core-shell NCs with varying shell thickness t_s (see **Chapter III** for further details on synthesis methods). **Figure 15a** reports the TEM images illustrating the progressive growth of undoped In_2O_3 shell around the ITO core of the samples analyzed in this work. Multiple aliquots were collected at different stages of the synthesis, resulting in a set of samples that share the same physical core (R_C = 5.5 nm - C0) and a range of different shell thicknesses (S1-S5, with t_s = 1.15 nm, 1.9 nm, 2.3 nm, 2.9 nm, 4.25 nm). The formation of core-shell structures was confirmed by probing the Sn-dopant concertation levels with inductively coupled plasma mass spectrometry (ICP-OES) and X-ray Photoelectron Spectroscopy (XPS) techniques (**Figure 15b**). These techniques are a standard for dopant distribution analysis in similar NCs,[58] due the different spatial sensitivity. In fact, ICP-OES is volume sensitive while XPS is a surface-sensitive technique. ICP-OES measurements (black curve in **Figure 15b**) indicate a higher Sn-concentration as compared to XPS measurements (red curve in **Figure 15b**) in all samples with shell, indicating that the Sn atoms are segregated in the NC core. No evidence of a significant diffusion of tin atoms from the core into the shell was found (further analysis on diffusion effects can be found in **Chapter V**). **Figure 15c** reports the (normalized) absorption spectra of representative core-shell samples in the NIR region. The distinctive feature of these plasmonic materials is the localized surface plasmon resonance (LSPR), generated by the oscillation of free electrons in the highly-doped semiconductor.[20,190] The LSPR peak position ω_{LSPR} and its lineshape are influenced by several factors, including structural defects, dopant concentrations, and the dielectric constant of the surrounding medium (ε_m). Importantly, the LSPR is determined by both the NC geometrical features (*e.g.*, R_{core}, t_s) and the electronic features, such as the carrier density level n_e and the depletion layer width (W) to be discussed in detail in **Chapter V**.[16,53,69,191] By fine-tuning the shell thickness of core-shell ITO NCs, it is possible to modulate the LSPR response. Initially, the growth of a sub-nanometric shell induces a small blueshift in the LSPR energy. This effect is due to the activation of donor atoms at the surface of the NC from the growth of the thin In_2O_3 layer, resulting in an increase in carrier density.[58] The subsequential addition of extra In_2O_3 layer continuously redshift the LSPR. The increasing shell thickness t_s modifies the dielectric surrounding of the NC, lowering the average carrier density mediated over the NC volume.[58] Notably, in particles with shell thickness larger than the critical t_s^* = 2.7 nm, a second shoulder appears in the NIR spectrum (see **Figure 16**). This is a signature of a second independent resonating mode with a distinctive carrier density level, generated by a sufficiently high carrier density in the outer parts of the NC.[187] This indicates that a more complex carrier density profile has to be considered for core-shell MO NCs.

In the case of ITO NCs, dopant placement engineering can be easily achieved thanks to the continuous growth approach. Doping engineering allows the placement of dopant ions with nanoscale control within the nanocrystal volume, directly affecting the electronic band profile and depletion layer formation and, ultimately, affecting the optical and electronic response of the material. Diffusion of donor atoms from the core into the shell can have noticeable consequences in ITO-In_2O_3 systems in terms of spectral response, since even a small number of free electrons present in the shell will modulate the optical response. **Figure 16** shows the absorption spectra of two sets of core-shell NCs with progressively thicker shells obtained employing two different synthesis techniques. The second contribution to the plasmonic response appears only in core-shell samples with a thick shell, preferably in samples more affected by diffusion of dopants. A more precise analysis of the electronic structure involving carrier density profiles is required to elucidate these effects, as discussed in **Chapter V**.

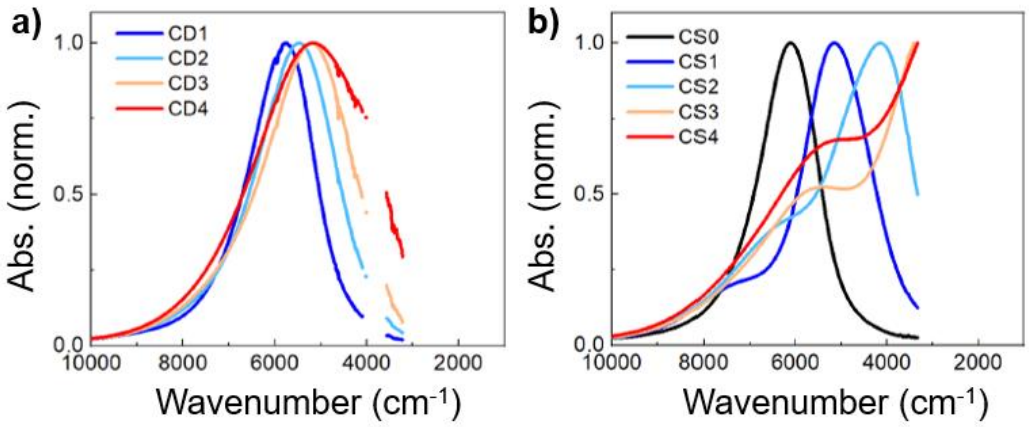

Figure 16 - Effects of dopants diffusion with numerical simulations and different synthesis techniques. a*) Normalized absorption spectra of the two sets of core-shell NCs with progressively thicker shells obtained employing two different synthesis techniques: segregated particles and* ***b****) subject to Sn-atoms diffusion. Respectively, the first set of ITO-In_2O_3 core-shell samples has a shell thickness going from 0 nm up to 4.95 nm (diameters: 10.1, 14.4, 16.1, 19.6, 20.0 nm), while the second set of samples is the already analyzed set C0-S5 with t_s up to 4.25 nm (diameters: 11, 13.3, 14.8, 15.6, 16.8, 19.5 nm). The plasmon peak position shifts to towards the red during the growth of the In_2O_3 layer. A second plasmonic response is present in core-shell samples more affected by dopants diffusion from the ITO core to the shell. Unpublished data from Ref.* [24].

IV. 2 Photodoping of MO NCs

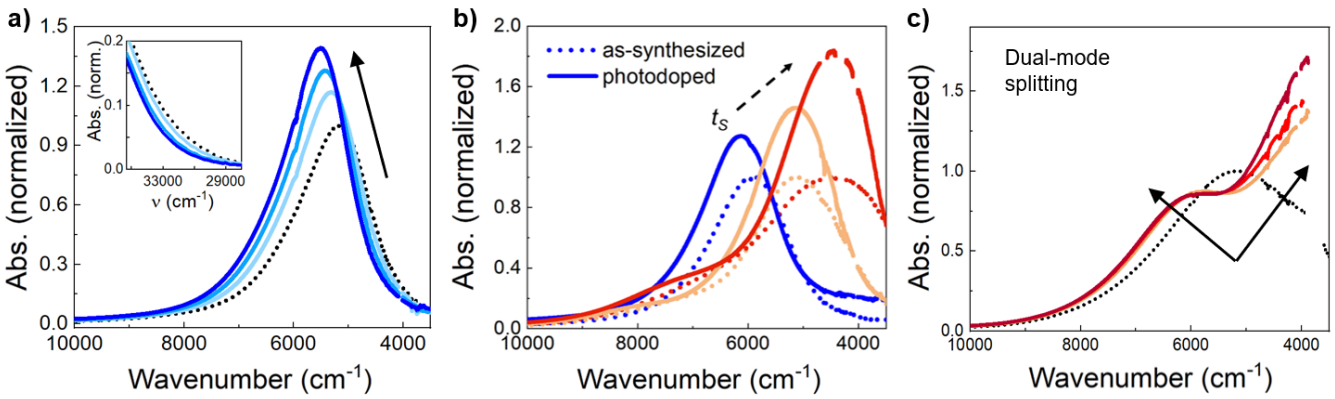

Figure 17 – Photodoping of colloidal ITO NCs. a) *Temporal evolution of the absorption spectrum of ITO NCs (with optical density normalized to the as-synthesized case, here reported as dotted lines) during the exposure of the solution to light beyond the bandgap energy. In uniform ITO particles, the LSPR significantly increases in intensity and blue-shifts due to the light-induced addition of extra carriers. Inset shows the effect of photodoping on the band edge absorption (Moss-Burstein effect).* ***b)*** *Normalized absorbance of typical ITO-In_2O_3 core-shell samples with increasing shell size, in as-synthesized (dotted lines) and photodoped (continues lines) cases, with a t_s of 0.15 nm (blue), 1.85 nm (orange), and 2.3 nm (red). Growing an undoped shell continuously redshifts the energy of the localized surface plasmon resonance (LSPR) peak in the NIR. After 20 min of UV exposure, the intensity of the LSPR peak increases significantly, reaching values up to almost double its initial absorbance.* ***c)*** *Dual-mode frequency splitting of the LSPR induced by photodoping in ITO-In_2O_3 core-shell sample S5. Figure adapted from Ref.*[23] *with permission from Springer Nature.*

To study the electronic structure of core-shell NCs and investigate these systems out of the equilibrium conditions, I post-synthetically alter the number of free carriers via photodoping. Photodoping consists of introducing multiple free charge carriers via light absorption and (quasi-)permanently storing them inside the NC by suppressing carrier recombination.[14,16,98] Here, photodoping was performed in solution to induce a dynamic variation of the ITO NCs' carrier density. Colloidal NCs were exposed to light beyond the ITO bandgap in the ultraviolet (UV) region (300 nm - 4.1 eV, FWHM = 20 nm) and an intensity of 36.8 mW cm^{-2}. Further experimental aspects are reported in **Chapter III**. It is worth underlining a substantial difference with respect to the usual conditions adopted in the doping treatment with ultraviolet light. In order to keep both the overall charge neutrality and stabilize the accumulated

electron density of each nanocrystal, the intervention of a hole-quencher (*e.g.*, ethanol, methanol) is commonly employed. In these experiments, however, the increase in the density of charges and the consequent increase in the plasmonic signal is quite evident without the addition of further compounds to the solution in toluene. Such behavior indicates that the recombination of the photogenerated charges is most likely suppressed thanks to the presence of the ligands and/or surface states, without the addition of alcohols, as already demonstrated in other cases in the literature [99,192–196] albeit the improbable trace of some residual EtOH molecule absorbed after the NCs washing cycles.

Figure 17a shows the typical temporal evolution of the absorption spectrum of colloidal MO NCs under UV exposure in anhydrous solutions. Due to photodoping, the LSPR peak energy of uniform ITO NCs gets progressively blueshifted and the LSPR peak intensity increases. Most of the light-induced variations occur in the first 5-10 minutes. After a few tens of minutes, all the effects saturate, indicating that the NC is fully charged and cannot store further photocarriers under the current conditions. As anticipated, the widening of the optical bandgap results in a bleaching of the band edge absorption (Moss-Burstein effect[127]). These light-induced effects are directly linked to the amount and the localization of extra electrons accumulated within the NC volume, and, hence, they can provide valuable information on the electronic structure of the NC.

Photodoping of core-shell Sn:In_2O_3-In_2O_3 NCs

Photodoping of core-shell MO NCs was performed to post-synthetically alter the carrier density levels and further investigate the optoelectronic properties of those systems out of the equilibrium conditions.[14–16,197] The normalized absorbance of three representative cores-shell samples of various t_s, with no shell (blue curve), small shell (orange curve) and large shell (red curve), are reported in **Figure 17b**. By comparing the spectra before (dotted curves) and after (continuous curves) the exposure to 20 min of UV light, it is possible to quantify the LSPR modulations. Due to photodoping, the intensity of the plasmon significantly increases ($\Delta I = I^{photodoped} - I^{as\ synthesized}$) and its peak energy shifts ($\Delta\omega = \omega_{LSPR}^{photodoped} - \omega_{LSPR}^{as\ synthesized}$). These effects progressively grow with the amount of photons absorbed (*i.e.,* the number of extra electrons accumulated), in agreement with existing literature reports.[15,16,78,100] The light-induced increase in carrier density corresponds to a stronger interaction between the free electrons and the impinging radiation, resulting in increased LSPR absorption. The sensitivity of the LSPR modulations to UV light (*e.g.*, ΔI and $\Delta\omega$) can be controlled by engineering t_s, with values of ΔI almost doubled in the case of the biggest NCs. The fine-tuning of the shell thickness, which can be easily achieved through

continuous synthesis, provides direct control over the plasmon sensitivity to external stimuli such as photodoping. The enhanced sensitivity of the LSPR to photodoping, achieved by increasing t_s, indirectly hint towards an increased number of stored charges, owing to the proportionality of the LSPR absorption with $n_e^{2/3}$.[22] Hence, shell engineering could be exploited for sensitivity and charge storage modulations in MO NCs. Apart from intensity variations, photodoping effects are also visible in terms of frequency variations of the LSPRs. While homogeneous particles are characterized by a blueshift of the absorption peak (**Figure 17a**), a sign of the increased carrier density due to extra photocarriers, core-shell particles exhibit a more complex tuning of LSPR lineshape. Remarkably, the photodoped spectrum of core-shell NCs (such as sample S1 or S2 of the set of NCs introduced in **Figure 15**) does not blueshift even if multiple carriers are introduced and stored into the system. Since the average carrier density is defined as the number of electrons over volume, this strongly indicates that the volume in which the electrons can freely oscillate expands after photodoping. This expansion is wide enough to compensate or even overcompensate (in case of redshifts) the increase of carriers.

Large core-shell particles, with a thick-enough shell exhibit a second absorption resonance due to the different carrier density and dielectric environment. For these NCs, it is possible to induce, post-synthetically with light, the splitting of the LSPR peak into two modes with distinct energies. **Figure 17c** shows the normalized absorption spectra for the core-shell sample S5, with a t_s = 4.25 nm, both before (black dotted line) and after (continue lines) photodoping. The LSPR peak of ITO-In_2O_3 NCs splits into multiple modes with distinctive energies, with the separation between the two modes being post-synthetically and continuously tunable. Multi-modal LSPR absorption can be significantly enhanced and controlled via photodoping, and it is possible to detect light-induced variations in both the high- and low-energy mode. The extent of the LSPR frequency splitting achieved via photodoping is similar to those generated via dopant engineering of large core-shell NCs at the synthesis stage, with the additional property of being dynamically controlled. In order to precisely describe the optoelectronic response of core-shell NCs and properly fit the evolution of absorption spectra under photodoping, a multi-layer optical model for plasmonic nanocrystals based on the Maxwell-Garnett effective medium approximation was applied (more details in **Chapter V**). In the following chapter, it will be shown that the multi-modal optical response is linked to spatially inhomogeneous carrier density profiles and, dynamically, to the tuning of depletion layers (see **Figure 20** for a comparison between simulations, experimental data, and empirical fitting on sample S5). The ability to split the LSPR as a response to the UV light and hence

modulate the IR absorption in intensity and frequency opens the way to several novel applications such as nanoantennas, SEIRS, photocatalysis, and detectors.

IV. 3 Chapter Summary

ITO-In_2O_3 plasmonic NCs were synthesized in a core-shell architecture by systematically tuning the shell thickness. The experimental characterization and the photodoping of ITO NCs is reported. The temporal evolution of the absorption spectrum of ITO NCs exposes a rich variety of light-induced effects that are sensitive to the structure of the NCs. Due to photodoping, the mean LSPR peak blueshifts in homogeneous NCs, it redshifts in core-shell NCs, and undergoes a dual-mode splitting with the formation of bi-plasmonic landscapes in large core-shell segregated NCs. The growth of an undoped shell around the ITO core provides direct control over plasmonic modulations with external stimuli, such as UV exposure, and is an effective tool to significantly alter the LSPR peak intensity. These empirical results display that increasing the shell thickness results in the enhanced sensitivity of the LSPR peak to photodoping and suggest that shell thickness engineering can be exploited to increase the number of stored photocarriers. These findings will be discussed and are preliminary to the analysis presented in **Chapter V**, **VI**, and **VII.**

V. Control of electronic band profiles and depletion layer engineering in metal oxide nanocrystals

The precise understanding of the energy band structure and depletion layers is of fundamental importance to control the optical and electronic properties of doped metal oxide NCs. Here, control over the electronic band profiles of metal oxide nanocrystals is demonstrated both in the static regime (*i.e.*, achieved during the synthesis stage) and in the dynamic regime, with post-synthetic modulations. Depletion layer engineering beyond surface states can be achieved by modulating the materials' composition and structure, such via the fine-tuning of the shell thickness in core-shell systems, as well as via photodoping. In this work, Sn:In_2O_3-In_2O_3 core-shell NCs are taken as a representative case study for MO NCs and their electronic structure is investigated as a function of the shell thickness. The introduction of the shell material with distinctive energy and doping levels induces a double bending of the electronic bands, owing to the formation of two interfaces between core, shell, and surface states. Due to the enhanced band bending, the electronically depleted region extends from the surface into the NC volume in the nanometer regime, allowing a deeper examination of depletion layers' effects in MO NCs. This work investigated the physics of the photodoping process, unveiling the key role of depletion layers and band bending in the photocharging of MO NCs. This experimental campaign involved multiple techniques and the development of ad-hoc approaches, which led to more findings and soon-to-be publications.[23–25] The conclusions reported in this chapter are supported by theory, numerical calculation, optical modeling, and experimental results and can be extended to other core-shell and core-multishell systems.

V. 1 Control of electronic band profiles

This chapter aims to investigate the electronic structure of metal oxide nanocrystals beyond the flat-band picture. Numerical simulations based on the solution of Poisson's equation were performed within the parabolic band approximation, following the procedure reported in **Chapter III**. Here, the depletion layer is defined as the region where the carrier density (n_e) drops below 10^{26} m^{-3} (threshold value at which plasmonic features can be detected)[22] and the active region as the part of the NC volume unaffected by depletion.

V. 1.1 Depletion layer engineering and electronic band bending

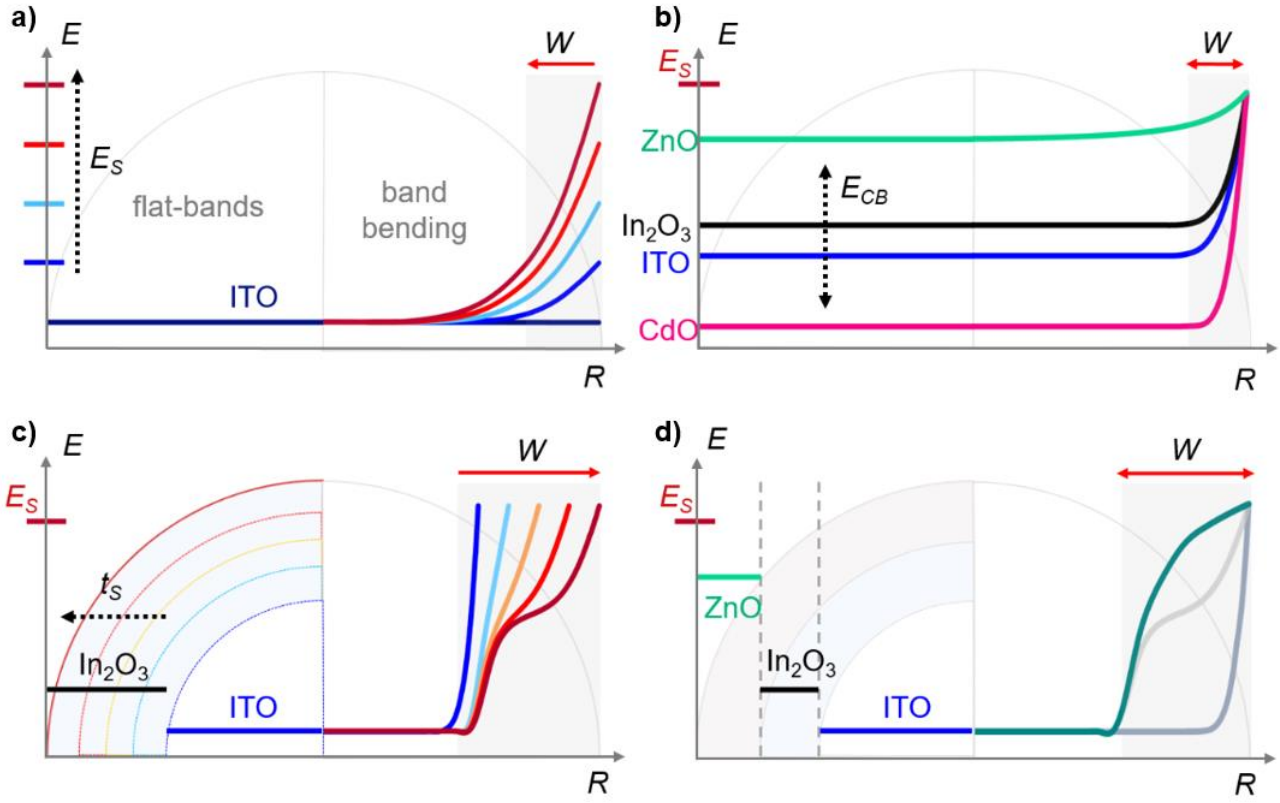

Figure 18 – Depletion layer and band bending engineering in MO NCs. *A semi-circle depicts the morphology of the NC, with the extension* ***R*** *in the abscissa (in nm) and the energy in the ordinate (in eV). The flat-band potentials in non-equilibrium are depicted on the left side of the sphere in each panel, while the band bending owing to Fermi level pinning is depicted on the right side. The Poisson's equation was numerically solved to provide band profiles.* ***a)*** *Surface state potentials (*$\boldsymbol{E_S}$*) tuning. The depletion width* ***W*** *expands as the* $\boldsymbol{E_S}$ *value is increased.* ***b)*** *The effect of various materials on* ***W*** *at a fixed* $\boldsymbol{E_S}$*.* ***c)*** ***W*** *expansion and depletion layer double bending in an ITO-In_2O_3 core-shell structure with a core radius (*$\boldsymbol{R_{core}}$*) of 5.5 nm and changing shell thickness (*$\boldsymbol{t_s}$ *=0,1,2,3,4 nm, i.e. blue, light blue, orange, red, and dark red).* ***d)*** *A multiple shell system made up of an ITO core (*$\boldsymbol{R_{core}}$*=5.5 nm) and an In_2O_3 and ZnO shell with a total radius of* ***R*** *= 9.5 nm. The band has a complicated profile that includes triple bending (green curve). For comparison, the grey curves depict a uniform ITO NC (dark grey) and an ITO- In_2O_3 core-shell NC (light grey) with total radius* ***R*** *= 9.5 nm, respectively. Figure reproduced from Ref.*[23] *with permission from Springer Nature.*

By choosing suitable materials and doping levels and the proper geometrical configuration in terms of structure and shell thickness, a wide variety of electronic band profiles can be targeted in doped metal oxide NCs. As reported in **Figure 18**, the bending of the electronic bands can be tuned and shaped both in the spatial direction (*i.e.*, radial, in the case of spherical particles) and in the energy domain. Fermi level pinning from surface states induces the upward bending of the conduction band of MO NCs, with the formation of spatially dependent profiles and depletion layers**. Figure 18** shows the numerically calculated conduction band profile and the depletion layer width (W) of MO NCs as a function of several parameters, such as surface potentials (E_S), different materials, and the introduction of additional electronic interfaces. In the first case, a fixed surface potential models the effect of Fermi level pinning ($E_S = 0, 0.5, 1, 1.5, 2\ eV$), from which the band bending profile is derived (**Figure 18a**). The precise value of E_S depends on multiple system-specific factors, such as the presence of defects, vacancies, trap states, and surfaces ligands, and can be determined experimentally.[20] The bending of the conduction band is induced by the formation of the ITO/surface electronic interface, highlighting the importance of surface effects in MO NCs. Increasing values of E_S results in the increase of the depletion width W, which extends into the NC volume in the nanoscale regime. The band structure of various MO materials, such as ZnO, In_2O_3, ITO, and CdO, has been simulated in **Figure 18b.** Also with constant E_S, the bending significantly depend on several parameters of the MO NC internal structure, such as the elemental composition of the material, doping levels, permittivity (ε), and bandgap energy (E_g). The band profile and, consequently, the extent of the depletion layer is a unique feature of each system.

Furthermore, the introduction of additional electronic interfaces within the NC volume is a powerful tool to alter the electronic profiles of MO NCs (**Figure 18c**). Core-shell Sn:In_2O_3-In_2O_3 NCs are taken as case study. Due to the presence of the In_2O_3 shell between the core and the surface, two electronic interfaces are formed (ITO/In_2O_3 and In_2O_3/surface). Typical values of E_S reported in literature for these systems are approximately 0.2 eV below the In_2O_3 conduction band minimum.[20] While in uniform NCs (*e.g.*, ITO core only) the band profile is radially determined by the depletion region near the NC surface; in core-shell NCs, the addition of shell layers results in a double bending of the conduction band. The double bending of the conduction band becomes particularly evident for the sizes and materials chosen when the thickness of the shell becomes larger than t_s^* ~3 nm, with the formation of a clear two-levels step gradient in the electronic band structure (more on the implications of this effect in the next subchapters). For ITO-In_2O_3 NCs, increasing the thickness of the shell t_s strongly affects the band's profile with a broader bending of the bands that extends for nanometers into the NC volume and increases the depletion

width ($W(t_s) \sim t_s$). Moreover, since Fermi level pinning anchors the depleted region to the surface of the nanocrystal, the depletion layer is progressively shifted from the ITO core towards the outer region of the NC. The growth of In_2O_3 around the ITO core introduces a tuneable intermediate layer between the core and superficial states. Upon shell growth, even if W increases, Fermi-level pinning affects more intensely the In_2O_3 shell region, which effectively shields the active ITO core from depletion. This effect could be detected as an expansion of the active core region, which is allowed to progressively return to an undeformed flat-band-like condition if far enough from the surface. In fact, R_{active}, *i.e.*, the region of the NC volume not affected by W, is typically larger than R_{core}. I highlight that the spatial extent of these electronic features (*i.e.*, R_{active}, W) does not correspond to the as-synthesized structural parameters (*i.e.*, R_{core}, t_s). The expansion of R_{active} is not due to morphological variations, such as an introduction of extra donor atoms or diffusion effects (more details in **Appendix**). Numerical simulations were performed to assess the impact of diffusion on the double bending of ITO-In_2O_3 core-shell NCs' conduction band. The Poisson's equation was solved and the band diagram was calculated for three different gradients of donors redistributed at the interface between core and shell (*e.g.*, step-function, low and moderate diffusion). The results, reported in **Appendix** (**Figure 37**), indicate that moderate amounts of diffusion of Sn atoms at the interface between the ITO core and the undoped shell do not significantly impact the double bending of the conduction band. Shell tuning is a powerful tool to control energy band profiles and engineer the depletion layer width in core-shell systems. This effect can be further extended in heterostructures composed of multiple materials, such as core-multishell NC architectures (**Figure 18d**). The numerical simulations indicate the importance of the architecture in designing the profile of electronic bands at the nanoscale. For example, a system composed of a core and two concentric shells exhibits three distinct electronic interfaces, generating a non-trivial bending of the conduction band (**Figure 18d**). Several combinations of materials and structures can be exploited, targeting specific electronic profiles at the synthesis stage. Precise tuning of the depletion layer width can be artificially achieved in MO NCs, unlocking a new fundamental degree of freedom to engineer the optoelectronic properties of these plasmonic nanomaterials.

V. 2 Dynamic modulation of electronic band profiles

In this subchapter, I examine the effect of post-synthetic modulations on the electronic structure of MO NCs, exploring the mechanism at the core of the photodoping process and demonstrating dynamic control

over the electronic band bending of ITO NCs. Numerical simulations were performed to calculate the effect of additional free electrons in core-shell systems as a function of t_s, identifying how their presence modifies the energy bands and carrier density distribution of the system. The proposed model was then tested experimentally on a set of core-shell ITO-In_2O_3 NCs of various shell thicknesses (samples S1-S5, with t_s = 1.15 nm, 1.9 nm, 2.3 nm, 2.9 nm, 4.25 nm, grown on the core sample C0 of radius 5.5 nm), monitoring the modulation in their plasmonic response upon the introduction of photogenerated charges. Further details on the synthesized samples and the photodoped spectra are reported in **Chapter IV.**

V. 2.1 Carrier density profiles and electronic band bending

Here, I simulate the electronic structure of core-shell ITO-In_2O_3 NCs of various shell thicknesses (t_s). The structural parameters, such as t_s and the core radius (R_{core}), were chosen to match the synthesized set of six samples experimentally characterized in **Chapter IV.** Numerical calculations were performed both for the as-synthesized and photodoped cases (details on the methods employed can be found in **Chapter III**), going beyond the static results reported in **Figure 18** and assessing the impact of dynamic, post-synthetic modulations on the electronic structure of MO NCs. In particular, the influence of the extra photocharges on the energy band profile and the redistribution of the free carriers in the NC volume are investigated. From the energetic profiles (black curves in **Figure 19a**), the spatially inhomogeneous carrier density distribution of the NCs can be extracted (black curves in **Figure 19b**). The radial gradient of $n_e(R)$ of as-synthesized core-shell samples with various t_s confirms the previously discussed trends of W and bend bending. The concentration drop at the surface of the NC is sufficient to suppress the metallic behavior of carriers entirely, and the region effectively acts as a dielectric. The two electronic interfaces of core-shell systems correspond to a double bending of the carrier density radial profile, which can be linked to leakage of carriers into the shell. Carrier density levels in the In_2O_3 shell can reach values as high as ~$1 \cdot 10^{26}$ m^{-3}. The approximation of the system into a highly-doped core surrounded by a dielectric shell is not valid for ITO-In_2O_3 NCs with $t_s > t_s^*$, characterized by a dual-plasmonic response. These NCs can be modelled as composed of three different regions with distinctive carrier densities: the doped core (n_{core} = $1.1 \cdot 10^{27}$ m^{-3}), the shell with enhanced carrier density ($n_{shell} < n_{core}$), and an electronically depleted region. Numerical methods can be employed to simulate the absorption spectra generated by the carrier density profiles calculated in **Figure 19b**, for NC of various shell thicknesses. As shown in **Figure 20**, simulations based on this simple model correctly reproduce the dual-mode plasmon resonance in the NIR spectrum, in agreement with the experiments.

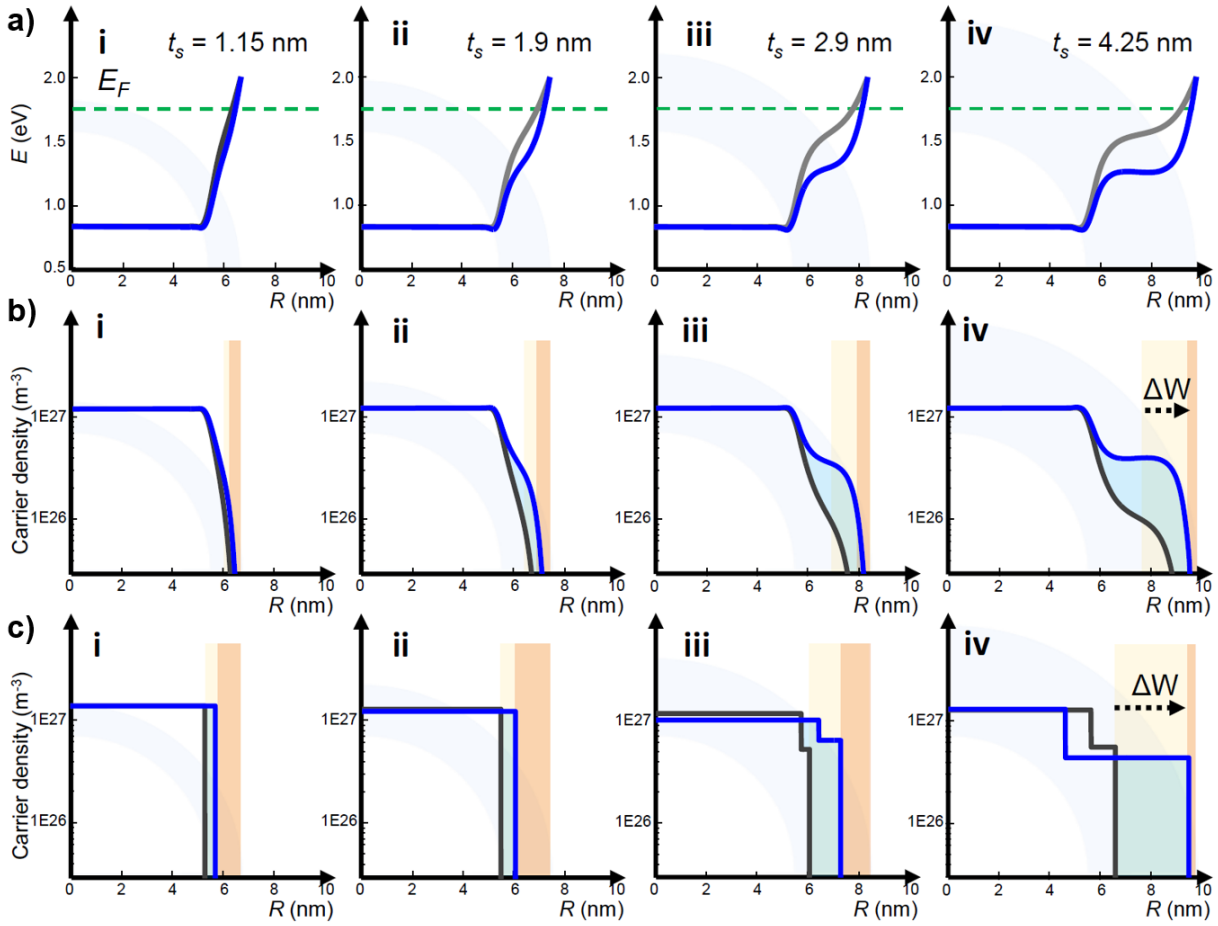

Figure 19 - Band profiles and depletion layer modulation via photodoping. ***a****) Simulated conduction band profiles of core-shell nanocrystals with increasing shell thickness before (black curve) and after (blue curve) the injection of photoelectrons. The light-induced bending of the bands close to the surface of the nanocrystal is the main mechanism responsible for the storage of extra electrons.* ***b****) Calculated electron density profiles of the same nanocrystals. The active region (R_{active}) of the NC is observed as a discrepancy between the carrier density onset and the structural core (R_{core}) and shell (t_s) dimensions (given in white and light blue in the background). The largest variations in n_e after photodoping occur towards the edge region of the nanocrystal with a significant rise of carrier density in the shell region (blue shaded regions). Due to photodoping, the active region expands ($\Delta R_{active} > 0$). Consequently, the depletion layer is progressively suppressed ($\Delta W < 0$) during the storage of electrons with photodoping (from light orange to dark orange).* **c****) The multi-layer optical model was used to fit the experimental data and provide carrier density profiles. The variations in the n_e profiles obtained from numerical simulations agree with the expansion of the active region (R_{active}) and W modulations of core-shell NCs of increasing t_s. Reproduced from Ref.[23] with permission from Springer Nature.*

Figure 19 and **b** summarize the results of the comparison of the electronic structure and carrier density

profile of core-shell MO NCs before (black curves) and after (blue curves) photodoping. For all samples, the accumulation of photoelectrons accentuates the native double bending of the energetic bands (**Figure 19a**). In samples beyond t_s^*, the conduction band profile can be approximated as a step function with two distinct levels: the core level, which remains unvaried upon photodoping, and an energetic level in the shell ~0.45 eV above the previous shell energy level. As a consequence, the distribution of carrier density significantly changes in the near-surface regions while n_e remains nearly constant in the core. In core-shell samples with $t_s > t_s^*$, the carrier density in the shell dramatically rises reaching values of around ~ $4 \cdot 10^{26}$ m^{-3}. After photodoping, R_{active} expands into the NC volume and, consequently, W decreases. As previously mentioned, the electronic features do not have a perfect correspondence with the structural parameters (*i.e.*, R_C, t_s). I highlight here that these electronic features (*i.e.*, R_{active}, W) can be controlled post-synthetically, and their spatial extent dynamically tuned with light absorption. Microscopically, the carrier density increase induced by photodoping fills the regions of the particle that were initially electronically depleted. The light-driven modulation of the depletion layer width ($\Delta W = W^{photodoped} - W^{as\ synthesized}$) depends on the initial value of W and increases with the shell thickness with a $\Delta W \sim {t_s}^3$ law (**Figure 36** from **Appendix**). Greater values of ΔW in samples with larger shells indicates a greater number of extra carriers can be stored within the electronic structure of similar core-shell NCs.

V. 3 Multi-layer optical model for carrier density profiles

To further test the proposed theory, the photodoping process was approached by applying an empirical model to fit the spectra of each sample. As introduced in **Chapter II**, the plasmonic properties of doped MO NCs can be well described within the framework of the Mie scattering theory in the quasi-static (dipolar) approximation. The LSPR response can be modeled by the Drude-Lorentz complex dielectric permittivity, showing that plasmon frequency (ω_{LSPR}) depends on the carrier density level n_e in the material. For homogeneous particles, n_e can be written as the number of free charges over the active volume: $n_e \sim N_e/R_{active}^3$. Hence, it is possible to link absorption measurements, which are a physical observable, to the number of free carriers (N_e) present at any moment in the NC system. During the analysis of the experimental data discussed in **Chapter IV**, the need for a more advanced optical model became evident due to the impossibility of fitting the absorption spectra with previously reported "2-layers" models.[20,187] The nanoparticles analyzed have a clear core-shell structure with nanometric shells,

composed of a core region with a distinct dielectric response from its surrounding shell and an electronically depleted region. Thus, the simple expression written for $\varepsilon(\omega)$ must be corrected. Recently, Zandi *et al.* employed the effective dielectric function given by the Maxwell-Garnett effective medium approximation (EMA) to take into account the effect of depletion layers (further details can be found in **Chapter III**).[20] Initially, I adapted this model by implementing a core-shell-like structure with a core region (here named *L1*) characterized by a frequency-dependent core dielectric function $\varepsilon_{core}(\omega)$ and a constant carrier density n_{core} surrounded by a dielectric shell (*DL* layer) with $\varepsilon_{DL} = 4$ and $\mathrm{n_e} = 0$ which represent the depletion layer. Outside the sphere a dielectric medium with fixed $\varepsilon_m = 2.09$ is present, to take in account the effect of the solvent. By applying this model, the accumulation of extra charges result in the increase LSPR intensity and the shift of its peak energy as a consequence of the varying W. The two-layer L1-DL model accurately describes the plasmonic response of samples with small shells both before and after photodoping (**Figure 19, Figure 20b**, **i** and **ii**). However, for $t_s > t_s^*$ and most photodoping cases, an extension of this model was necessary. To describe the distinct dielectric response of the two materials, another effective dielectric function $\varepsilon_{\mathrm{eff}}(\omega)$ based on the Maxwell-Garnett effective medium approximation (EMA) has been recently reported in literature.[69,187] This second EMA model, here named L1-L2, is particularly advantageous in the case of big core-shell particles,[187] for cases in which the effect of resonating electrons in the shell (the second layer, *L2*) adds to the plasmonic response of the core (the first layer, *L1*), leading to the formation of a dual-mode IR absorption. While this 2-materials 2-layers approach approximately holds in the static case, it fails when extra carriers are introduced into the system via photodoping. As a matter of fact, in order to be able to fit the experimental spectra after photodoping, the two layers (*L1* and *L2*) need to change size and expand into another region, without exceeding the physical boundaries of the NC itself.

For this reason, I developed a more general multi-layer model composed of three concentric layers, *L1*, *L2*, and *DL*, which takes into account the presence of different materials and electronically depleted regions at the surface of the NCs due to Fermi level pinning. Within this picture, the continuous carrier density radial profile $n_e(R)$ is approximated with two discrete regions (*L1* and *L2*) of uniform densities, $n_{core}(R)$ and $n_{shell}(R)$, and a third dielectric region (*DL*) with a defined density of $n_e = 0$ and a fixed $\varepsilon_{DL} = 4$. The entire NC is then immersed in the dielectric medium $\varepsilon_m = 2.09$. The third layer (*DL*) introduced here accounts for the formation of the depletion layer at the electronic interface between shell and surface, going beyond what has been implemented so far to describe capacitive charges in MO NCs.[20,69,187] The proposed multi-layer optical model (L1-L2-DL) is a generalization of the 2-layer model

(L1-DL), and indeed they coincide in the cases of homogeneous NCs or core-shell NCs with thin shells (with the thickness of L2 going to zero). Remarkably, the expansion of the second layer into the depletion layer is found to be fundamental to properly fit the photodoped spectra. The same approach could be further extended to describe the plasmonic response of core-multishell systems, generalizing the 3-layer model with the introduction of extra layers accounting for different materials or carrier density levels. This model allows the approximation of the continuous carrier density profile with a multi-layer step function and is a powerful tool to characterize the optoelectronic properties of plasmonic materials in a relatively simple way. Further information regarding the model, the approximations implemented, and the fitting procedure can be found in **Chapter III.** The multi-layer model is able to reproduce the experimental optical properties of all core-shell samples, both in the static condition and under dynamic modulations of the electronic structure. **Figure 38** (in the **Appendix**) shows the absorption spectra of the samples C0-S5 before and after photodoping with the corresponding fits reported in orange. Thanks to this fitting model, it is possible to resolve the electronic structure at the nanoscale, obtaining information on the carrier density levels at different points of the NC radial distribution.

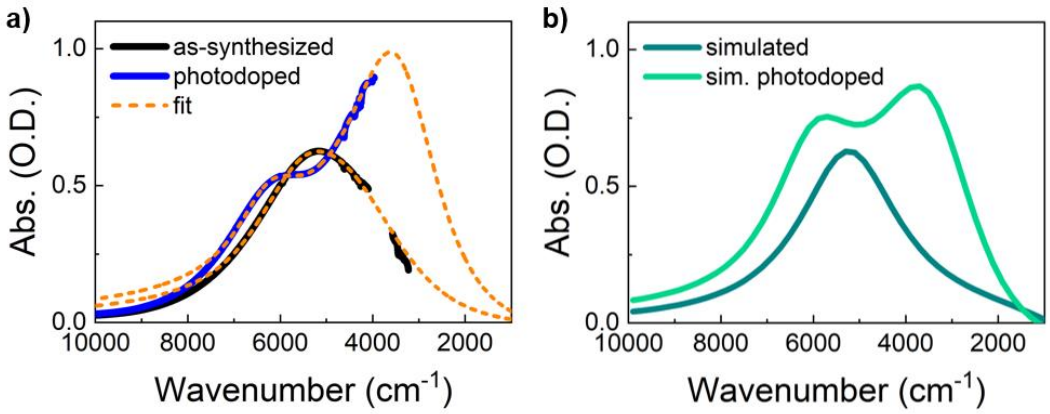

Figure 20 - Comparison of experimental data, optical modeling and numerically calculation. a) *absorbance of core-shell sample S5 (t_s = 4.25 nm), as-synthesized (dotted line) and photodoped (continue line). The fitting of the experimental data using the multi-layer optical model is depicted by the orange lines.* ***b)*** *Numerical simulations of the absorbance of the same ITO-In_2O_3 NC with t_s = 4.25 nm (dotted green lines) and the simulation with extra electrons (i.e., photodoping, solid green line). Figure adapted with permission from Ref.*[23].

The values of carrier density and depletion layer width extracted with the multi-layer optical model from the experimental data, before and after photodoping, are reported in **Figure 19c**. For all samples,

irrespectively of t_s, the primary effect of photodoping is to decrease W, effectively increasing R_{active}.[69] A significant variation in carrier density levels occurs in the outer parts of the NC, with n_{shell} reaching values of $\sim 5.4 \cdot 10^{26}$ m^{-3}, while the core carrier density n_{core} remains nearly constant (with variations of less than 14%). Based on experimental data on core-shell NCs, these results confirm the predictions discussed in **Chapter V.2** and further validate this approach for the analysis of the optoelectronic properties of MO NCs. The combined analysis performed with numerical simulations, experiments, and empirical fitting strongly supports the thesis that dynamic control over the bending of the electronic band profiles can be achieved post-synthetically and highlights the importance of depletion layers in the charging processes of these systems. Furthermore, unreported plasmonic effects, such as the modulation of bi-plasmonic landscapes and the light-induced LSPR splitting, can be understood within the same scheme by a dynamic modulation of the NC electronic structure. **Figure 20** reports a comparison between experimental data, fittings, and numerically calculated spectra for the sample S5 (with t_s = 4.25 nm) characterized by the dual-mode plasmonic splitting induced by photodoping (see **Chapter IV**). More details on the Fermi level rise and photodoping mechanism will be discussed in **Chapter V. 4** .

V. 3.1 Dynamic modulations in the multi-layer model

Thanks to the multi-layer optical model, it was possible to fit all data and explain the physics behind the frequency splitting of the LSPR resonance observed, upon photodoping, in particularly well-segregated core-shell NCs (**Figure 21**). The proposed scheme was further tested and compared to the previously existing model by analyzing two different syntheses of core-shell photodoped NCs: with more and less segregation of the donor atoms in the ITO core (more details on the synthesis procedure can be found in **Chapter III**). The observed evolution of LSPR lineshape and position upon shell growth was reproduced with the 3-layer optical model by keeping the total number of carriers constant (the impact of adding In_2O_3 shell layers on the total number of free carriers of the system was assumed to be negligible), while expanding the NC size to match the samples radii and by tuning the relative sizes and contributions of *L1* and *L2* (see **Figure 39** in **Appendix**). It was possible to reproduce the experimental trend while keeping the core size (*L1*) fixed by progressively expanding the depletion layer and, in the largest NCs, filling the shell with electrons. In particular, the multi-layer model identifies the modulations in the second layer (*L2*), both in terms of physical extension (size) and carrier density, as the principal factor in the evolution of the observed spectra. Moreover, it provides evidence that slightly different synthesis procedures can result in significantly different radial distributions of donor atoms inside the NC and optical responses,

with a spillover of electrons from the core into the shell during shell growth, and the related generation of dual-mode plasmonic response, being the main source of the differences between the two sets of samples.

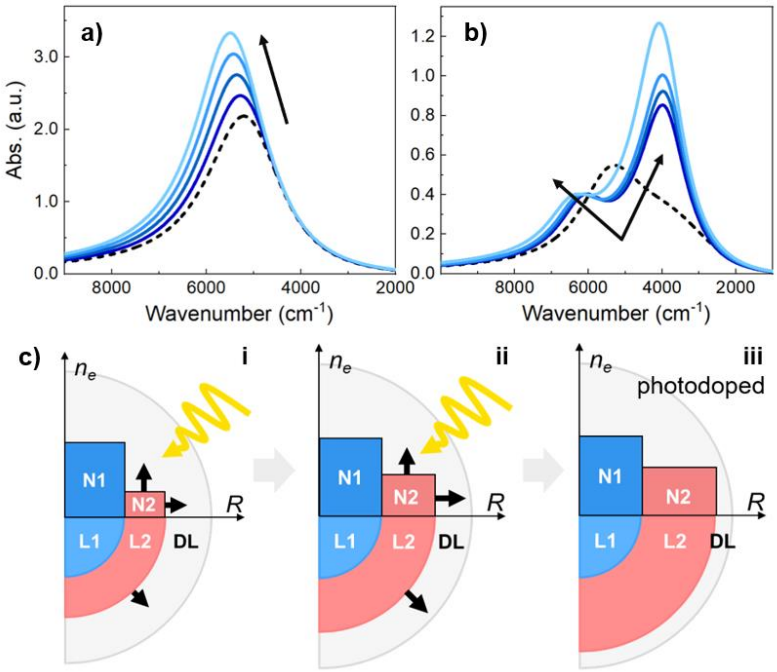

Figure 21 - Photodoping of ITO NCs simulated with multi-layer optical model. *Evolution of the absorption spectrum of ITO NCs under UV exposure for homogeneous particles (**a**) and ITO-In2O3 core-shell segregated NCs (**b**). The simulated spectra of the two samples are obtained with the multi-layer optical model by reducing the depletion layer width (DL) without increasing the carrier density level in the core (N1). **c)** Illustration of the photodoping of core-shell NCs achieved by expanding the second layer (L2) and slightly increasing its concentration (N2). The segregated NCs undergo a two-step process: initially photodoping causes plasmonic splitting by increasing the contribution of the second layer (from **c-i** to **c-ii**); after that, the addition of extra photoelectrons causes the peaks to blueshift and increase in intensity (from **c-ii** to **c-iii**). Unpublished data from Ref.* [24].

By applying the multi-layer optical model to the photodoped spectra, it is possible to gather further information on how the extra carriers redistribute in the electronic structure of MO NCs. **Figure 21** shows The evolution of the absorption spectrum under UV exposure of homogeneous and ITO-In_2O_3 core-shell NCs was replicated with the multi-layer model. The simulated spectra are obtained by reducing the depletion layer width (*DL*) without increasing the carrier density level in the core (*N1*). All kinds of modulations of the three layers, *i.e.*, *L1*, *L2*, and *DL*, has been tested to qualitatively reproduce the trends observed with absorbance measurements in samples with different t_s under photodoping (further

information in the **Appendix**). Modulations in the multi-layer optical model showed that the increase in carrier density of the second layer (L2) for large core-shell NCs and, more generally, the expansion of the active region is a fundamental aspect in the dynamic description of the system. Depletion layer tuning is strictly necessary, and every other kind of variation failed to reproduce the experimental trends, simulations of the Fermi level rise included. By studying the evolution of the second layer, it is possible to deepen the comprehension of the light-induced LSPR dual-mode splitting of sample S5. Segregated NCs undergo a two-step process. Initially, photodoping causes plasmonic splitting by increasing the contribution of the second layer and expanding it to a more superficial region of the NC (**Figure 21e,** from **i** to **ii**). The increase of carrier density and the different electronic environment correlate to a variation in the damping coefficient Γ, depicting electron scattering (more details in **Chapter II**). The variation in electron scattering is fundamental to reproduce the plasmon splitting experimentally observed and cannot be easily justified from a physical point of view without taking into account an expansion of the active region into the NC shell, where Fermi level pinning induces a radial gradient in the energy band profile. Due to this light-induced filling of the shell region, the small plasmonic contribution of the shell moves from the right to the left of the main LSPR peak and the overall spectrum resembles the one of large core-shell NCs affected by diffusion (*e.g.,* **Figure 39c**, **Appendix**). After that, the addition of extra photoelectrons causes the peaks to blueshift and increase in intensity (**Figure 21e,** from **ii** to **iii**), exactly as for more conventional cases.

V. 3.2 The optimal electronic structure for charge storage enhancement

As a final step, I analyze the number of extra photocarriers introduced via photodoping and stored in each NC. **Figure 22b** reports a quantitative comparison between the numerical approach and the optical modeling by plotting the stored photocarriers (ΔN_e) as a function of the shell thickness. ΔN_e is defined as the difference between the number of free carriers of the photodoped NC and of the as-synthesized NC: $\Delta N_e = N_e^{photodoped} - N_e^{as\ synthesized}$. Both approaches agree on the finding that ΔN_e increases with the shell thickness with a $\Delta N_e \sim {t_s}^3$ trend. Values as high as 800 extra electrons per NC are found in large core-shell NCs. Further analysis of the NC stored carriers was conducted using titration on photodoped NCs to count the number of stored electrons, as discussed in **Chapter VI**. Schimpf *et al.* reported the linear dependence of ΔN_e with the volume of the NC and size effects are partially responsible for the enhanced charge storage capability of big MO NCs.[78] However, numerical simulations indicate

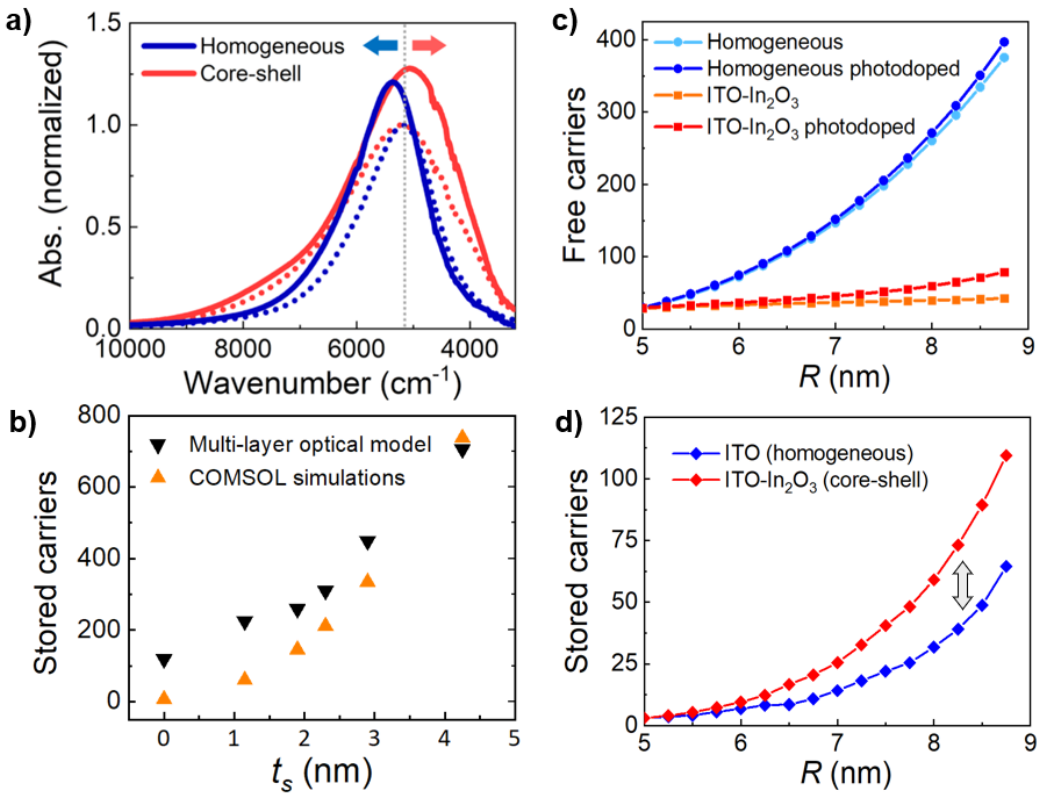

Figure 22 - Comparison between the core-shell architecture and homogeneous particles. ***a)*** *Experimental comparison between the optical response of two samples with same size and doping concentrations but different electronic structure, before (dotted line) and after (continuous line) photodoping (homogeneous ITO in blue, core-shell ITO-In2O3 in red). The sensitivity of the LSPR modulation via photodoping is enhanced in the core-shell case. I highlight that the peak position of the LSPR blueshifts in the homogeneous case while it redshifts in the core-shell case, due to photodoping.* ***b)*** *Photoelectrons stored in the NCs as a function of the shell thickness, showing the* $\Delta N_e \sim t_s^3$ *trend for values extracted from the empirical multi-layer model (black curve) and the numerical simulations (orange curve).* ***c)*** *Numerical calculations of the total number of free carriers in the two cases of a homogeneous NC (ITO – core only) and core-shell NC (ITO-In2O3), as a function of the shell thickness before and after photodoping.* ***d)*** *Number of photocarriers stored in the two cases as a function of the radius. Figure adapted from Ref.*[23] *with permission from Springer Nature.*

that the number of stored carriers in core-shell NCs is significantly larger than in inhomogeneous samples with the same size (**Figure 22d**). In order to confirm this result experimentally and isolate the effect of the depletion layer, two samples of the same size but different electronic structures were synthesized. The core-shell sample S3 (with t_s = 2.3 nm) was compared with a homogeneous NC (pure ITO) by

keeping all other parameters unchanged (*i.e.*, total NC radius R, doping density N_d, experimental conditions). **Figure 22a** reports the comparison between their optical response before and after the photodoping process (homogeneous ITO in blue, core-shell ITO-In_2O_3 in red). Strikingly, upon photodoping, the LSPR peak energy blueshifts in the homogeneous case while it redshifts in the core-shell case. The empirical optical model was employed to calculate ΔN_e in these cases, obtaining that the core-shell sample accumulates ~40% more carriers than its uniform counterpart of the same size. This combined theoretical and experimental approach demonstrates that control over the band bending and depletion layer engineering can improve the charge storage capability of MO NCs. Moreover, numerical simulations predict that the charge storage capability enhancement due to the core-shell architecture increases with the increasing of t_s.

V. 4 The photodoping process: a new explanation

The fundamental importance of depletion layer modulations clearly emerges from the combined investigations of photodoped core-shell NCs with experiments, empirical fitting, and numerical simulations. The two main results of this research work are, first, that the depletion layer plays a key role in the charging and discharging process of the NC upon photodoping dominated by reductions of W (with contractions typically higher than 30% and theoretically up to almost 100% the as-synthesized width) in photodoped NC. In other words, the photodoping process induces a spatial expansion of the active region, *i.e.*, the fraction of the total volume accessible to the free electrons, into the electronically depleted shell. As a matter of fact, the filling of the depletion layer can be considered as the distinctive signature of the photodoping process. Higher ΔW values justify higher charge storage capabilities in core-shell NCs with large shells due to the tendency of the additional photocharges to electronically fill W. Secondly, the light-induced variations in the carrier densities profile are highly inhomogeneous. The NC core density remains unchanged, with no detectable variations in n_e. All variations appear to occur in the shell regions, where the electronic structure is more strongly affected by surface states. The additional charges introduced with light are stored in the more superficial regions, significantly raising the local carrier density level. This effect becomes particularly clear for core-shell NCs with large shells and by analyzing the evolution of dual-mode plasmonic resonances in detail.

Fermi level rising or depletion tuning?

Up to date, the introduction and storage of multiple photocarriers in MO NCs has always been justified within a flat-band picture as the uniform rise of Fermi energy level, with the extra photoelectrons uniformly accumulated on the top of the conduction band. Fermi level rising has been experimentally observed as a result of the light-induced multiple accumulations of electrons in MO NCs.[14,16,78,198] In this work, the photodoping process of core-shell MO NCs is successfully described without changing the Fermi level energy. As a possible explanation for this apparent contradiction, I hypothesize that the experimentally observed uniform rise of the Fermi level results from the averaging over the local carrier densities between near-surface regions and internal regions of the NC. A similar 'averaging' effect would be compatible with the Moss-Burstein effect observed during photodoping, with the optical bandgap of the system getting wider due to the tuned electronic structure in the superficial layers of the NC. Before deepening the analysis with the evidence in support of the new explanation and the differences between the two approaches, I underline here one fundamental reason why the commonly accepted model for the photodoping mechanism has to be rejected. Any explanation based on the flat-band assumption introduces non-negligible approximations. The presence of nanometric depletion layers in MO NCs and their impact on the optoelectronic properties are well-documented. In a flat-band scenario, a uniform rise of Fermi level necessarily imply a blueshift of the plasmon energy (ω_{LSPR}). However, photodoped NCs exhibiting no blueshift or even a splitting of the ω_{LSPR} were observed (**Figure 17**). As previously reported, ω_{LSPR} is proportional to n_e, the number of free charges over the active volume $n_e \sim N_e/R^3_{active}$. Since due to photodoping, by definition, the number of free charges increases ($N_e > 0$), without taking into account depletion layers ($\Delta R_{active} = 0$) the energy of the plasmon can only increase. The fact that the photodoped spectrum of core-shell NCs (such as samples S1 or S2, see **Appendix**) does not get blueshifted, even when multiple carriers are stored, is a strong indication that the volume in which the electrons can freely oscillate expands after photodoping. This expansion is wide enough to compensate or even overcompensate the increase of carriers. A redshifted photodoped spectrum (**Figure 22a**) is direct evidence against the explanation of photodoping within the flat-band picture as rise of the Fermi energy level. Moreover, even by considering the distortions induced by surface states in the electronic structure of core-shell MO NCs, several aspects remain not explainable with a simple rise of the Fermi level energy. For example, the bi-plasmonic response and the light-induced plasmonic splitting observed in large core-shell samples seem to be incompatible with an increase of n_e in the inner region of the NC. Finally, it is fair to mention that, even without varying the NC's Fermi level energy, the approach and

the interpretation proposed in this chapter involves a local increase of carrier density in the superficial regions. This model is particularly effective for core-shell doped MO NCs, while other approaches might be more convenient for some degenerate cases. Further studies to completely exclude any rise of the Fermi level energy in the system or establish the extent of a similar contribution to the photodoping effects are warmly encouraged. The predominant and most fundamental effect identified by this study is the expansion of the active region into the electronically depleted regions of the NC. This modulation of the depletion layer is found to be strictly necessary for the photodoping process.

The photodoping process unveiled

Here, a new explanation for the physics at the core of the photodoping process is presented. The main light-induced effects on the electronic structure of core-shell MO NCs are the reduction of the depletion layer width and the inhomogeneous rise of carrier density in the outer regions of the NC. The mechanism behind the light-induced filling of electronically depleted layers can be better understood by analyzing the energetic band profile. In core-shell MO NCs, the observed double bending of the energetic bands becomes more pronounced upon photodoping. In some cases, the double bending is emphasized to the point of forming a two-step-like gradient. In this work, it has been shown that it is possible to significantly enhance the band bending of core-shell NCs by growing a shell. With respect to homogenous particles, core-shell systems exhibit more substantial distortions in the band profile (hence, larger W), which amplify the extent of all light-induced modulations. Shell-tuning helped clarify the link between these two aspects, unveiling the role of the energetic structure in the doping process. Photodoping effects, such as variations in the carrier density distribution and related variations in the optical properties, are a direct consequence of modulations of the NC conduction band. Ultimately, photodoping is a powerful tool to achieve dynamic control over the energetic band profile in a continuously tuneable way. The dynamic, photo-induced band bending is the main photodoping mechanism of MO NCs, thanks to which multiple photocarriers accumulate inside MO NCs. Moreover, the bending of the conduction band allows the filling of electronically depleted regions with extra carriers, reducing the depletion width. Since the NC core is not significantly affected by light-induced band bending, the storage of extra carriers occurs mainly, if not exclusively, in the outer parts of the MO NCs. Remarkably, this is the same part of the system affected by distortions induced by surface states, with considerable deviations from the flat-band regime. In addition, the observed band bending creates an energetic gradient inside the NC, which promotes charge separation near the NC surface, driving holes towards the outside of the NC and ultimately allowing the stable accumulation of photoelectrons. This mechanism could help prevent

carrier recombination and further supports the thesis that depletion layers and band bending are strictly necessary for photodoping to occur. As a perspective, further research work on the ligands chemistry and surface states of photodoped MO NCs could be conducted to better clarify the fate of the photogenerated positive charges surrounding the NC.

V. 5 Chapter summary

To summarize, full control over the band structure and their bending in the MO NCs family of materials was demonstrated both during the synthesis stage (static case) and via photodoping. These findings are based on a combination of theory, modeling, and experiments. The band bending of several MO NCs was calculated with numerical simulations (COMSOL) in different architectures, indicating that double band bending is a fundamental property of core-shell NCs. Numerical simulations served as a framework to accurately describe the electronic structure of the NCs at the nanoscale in the static case, as a function of surface states potentials, material composition, the thickness of the shell in core-shell systems and multi-shell architectures; as well as to describe the evolution of the band bending under dynamic modulations, such as after the introduction of extra photocarriers. Thanks to this scheme, it was possible to demonstrate that complete control over the band structure can be achieved by carefully choosing materials and modulating their structural properties, targeting a wide variety of desired features and configurations. These results were experimentally tested using Sn-doped Indium Oxide (ITO)-In_2O_3 core-shell NCs as a case study. In order to investigate the proposed model, I systematically synthesized core-shell ITO-In_2O_3 NCs of targeted features, fine-tuning structural and electrical properties, and post-synthetically modified their band structure with photodoping. The light-induced formation of bi-plasmonic energy landscapes in core-shell NCs was observed due to photodoping. A specifically designed three-layer optical model was developed to describe the optical response of the (photodoped) core-shell ITO-In_2O_3 NCs. Thanks to this fitting model, it is possible to resolve the electronic structure at the nanoscale, obtaining information on the carrier density levels at different points of the NC radial distribution.

From this combined theoretical and experimental approach, I found that, first, double bending of the bands dominates the electronic structure of (photodoped) core-shell ITO-In_2O_3 NCs and that the depletion layer predominantly affects the In_2O_3 shell. Depletion layer engineering is a powerful tool that provides a new degree of freedom for optimizing targeted features in MO NCs. Second, it was unveiled

that the photodoping mechanism relies entirely on the presence of depleted regions and energetic distortions in the outer regions of the NC. The accumulation of extra photocarriers induces the reduction of the depletion layer width and an inhomogeneous distribution of stored charges, resulting in the evolution of different levels of carrier density in the core and the shell. The storage of extra charges is made possible by light-induced modulation of the depletion layer and band bendings. The electronic rearrangement of energy bands and the filling of electronically depleted regions are the primary mechanisms behind the photodoping process of metal oxides NCs. Third, depletion layer engineering was exploited to enhance the number of photocarriers stored in ITO NCs. A direct comparison between homogeneous and core-shell NCs of the same size demonstrated the importance of tuning the electronic structure of these materials for potential energetic applications. This model could be extended to other systems and nanostructures, further validating the proposed approach. The possibility to control energetic band profiles and engineer depletion layers at the nanoscale opens promising perspectives for the design of targeted optoelectronic properties in metal oxide nanostructure. I expect these studies to contribute to the development of optimized devices based on the MO NC photodoping process.

VI. Multi-electron transfer reactions from photodoped nanocrystals

The light-driven charge accumulation process of MO NCs is emerging as a new route to enhance novel photo-conversion processes.[14–16,93,98,99,188,192] Several works have demonstrated the reversibility of the photodoping process by using potentiometric titration methods, in which molecular oxidants were added to the colloidal solution of MO NCs to extract the photo-chemically excited electrons.[14,16,98,188,192] Many applications which require efficient multiple charge transfers of photodoped electrons, such as the conversion of photovoltaic energy, batteries, or the implementations in photocatalysis and photoelectrochemistry, would benefit from this process.[199–201] Importantly, multiple charge transfer per active unit (*i.e.*, MO NCs) would translate in a dramatic increase in energy density, with the associated reduction in materials employed and costs. The same energetic and economic considerations can be applied for the redox transformations of electrochemical cells and catalytic reactions too.[202] The reported yields and kinetics of such reactions show an improved performance due to multi-charge transfers, independently if the reaction occurs in liquid or in solid systems (*e.g.*, electrodes). Up to date, multi-charge transfer reactions have been reported in several examples, such as gold nanoparticles for CO_2 conversion and organic donor-acceptor systems, in which proton-coupled multi-electron transfers were observed.[201,203,204] Colloidal semiconductor NCs can accumulate multiple highly-reactive photocarriers via light absorption and release them to react with organic compounds.[205] However, so far, only few studies on MOs have been reported to directly address a multi-electron transfer of photo-excited electrons. Among these, ZnO and TiO_2 NCs were successfully implemented in photocatalysis and in electrochemical reactions where multi-electron transfer processes were required, such as oxygen reduction reactions.[78,99,206–208]

In this work, I investigate this remarkable opportunity in tin-doped indium oxide NCs. The ability of ITO NCs to provide multi-transfers of electrons accumulated during the photodoping process can be investigated via oxidative titration and monitored with optical spectroscopy measurements. The findings of this work show that photodoped nanocrystals have the ability to trigger multi-electron chemical processes when exposed to a frequently used organic electron acceptor. Specifically, to address multi-electron oxidation 2,3,5,6-tetrafluoro-7,7,8,8-tetracyanoquinodimethane (F4TCNQ), a chemical molecule capable of undergoing a double ionization, was employed. By following characteristic

spectroscopic features of the F4TCNQ ionized species, a quantitative analysis on their concentration can be performed and, by this, investigate the charge transfer mechanism as single or multi-electron phenomenon.

VI. 1 Discharge of photodoped nanocrystals via oxidative reactions

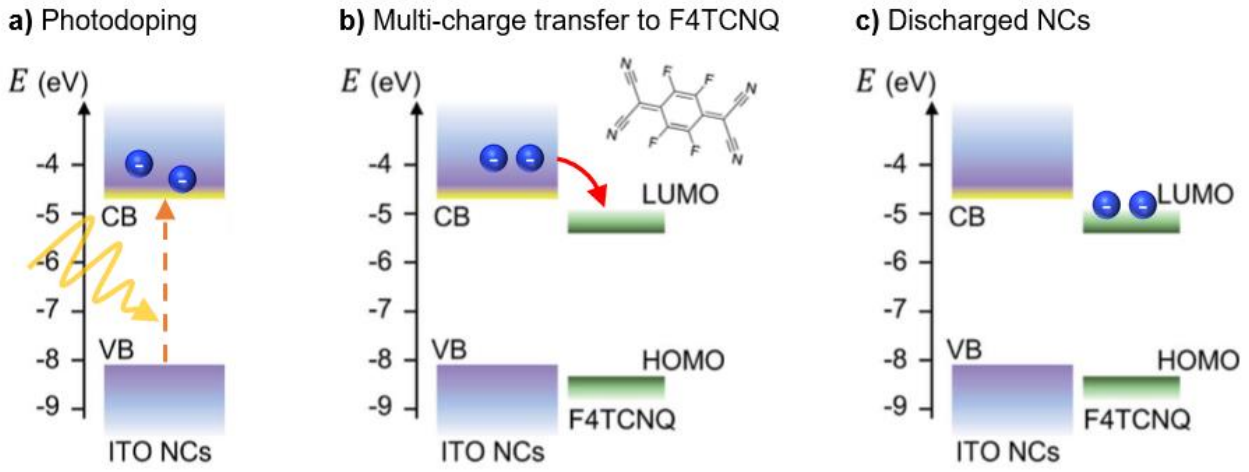

Figure 23 – Schematic illustration of the main steps of the multi-charge transfer experiment. a) *ITO NCs are photocharged with UV light and extra photogenerated electrons are stored inside the conduction band of the nanoparticle.* ***b)*** *Multi-charge transfer from charged ITO NCs to F4TCNQ molecules occurs as soon as the titrants are introduced in the solution. The electron transfer, from ITO's conduction band (CB) to F4TCNQ's LUMO (lowest unoccupied molecular orbital) state is energetically favoured due to band alignment. The highest occupied molecular orbital (HOMO) state's energy is reported next to the valence band (VB) of ITO.* ***c)*** *In the final stage, completely discharged ITO NCs returns to the as-synthesised condition due to the reduced F4TCNQ molecules.*

Here, I analyze homogeneous ITO NCs with a diameter of ~11 nm that are colloidally stable with organic ligands (oleate molecules) in toluene. A solution of ITO NCs was carefully prepared for electro-optical titration measurements and photodoped with a UV LED. Further information on the sample preparation process can be found in **Chapter III**. **Figure 23** summarizes the main steps of the multi-charge transfer experiment from an electronic point of view. First, extra electrons are promoted and stored into the conduction band of ITO NCs via photodoping. Secondly, a known amount of F4TCNQ molecules is introduced into the solution with photodoped NCs. Multi-charge transfer reactions between the two

species occur due to the energetic alignment (**Figure 23b**). The transfer of electrons from ITO's conduction band to the lowest unoccupied molecular orbital (LUMO) state of F4TCNQ molecules is energetically favorable and overcomes any eventual obstacle between the two induced by surface states or ligands. Upon multiple additions of titrants into the solution, this process could continue until – theoretically - all photogenerated electrons are extracted from the ITO NCs, which return to the as-synthesized conditions. In this final stage, the solution is formed by a mixture of discharged ITO NCs and reduced F4TCNQ molecules (and, eventually, unreacted F4TCNQ molecules in excess).

F4TCNQ is a widely-employed electron acceptor with high electron affinity (5.2 eV) and has been extensively implemented for both a large variety of fundamental studies of charge transfer processes (*e.g.*, photoluminescence quenching) and for photovoltaic applications, as a p-dopant of organic materials in hole-transporting layers.[209,210] This titrant is particularly interesting for quantitative analysis of multiple charge transfer due to its ability to acquire multiple electrons in its neutral form. Specifically, F4TCNQ can form two characteristic ionized species (*i.e.*, anion and dianion species)[211,212] with donor-host situations displaying lower ionization energies ($\lesssim$ 5eV). Furthermore, the stable formation of either the anion or dianion species shows distinctive spectral features in the absorption spectrum of the solution, making the detection of the single and double ionization process easily accessible with conventional optical measurement techniques. To give an example, the formation of F4TCNQ dianion is detectable in a variety of polymer-dopant systems.[213] Recent works have shown that the doping of bithiophene-thienothiophene-based copolymers with F4TCNQ resulted in a near to complete double ionization of dopant molecules allowing an ionization enhancement of 200%.[211,214] However, up to date, double reduction of F4TCNQ was never reported for neither inorganic-dopant nor for photodoped MO NCs-dopant mixtures.

Hence, this work focuses on the spectroscopic characterization of the absorption of ITO NCs and the F4TCNQ molecules. The typical photodoped spectrum of ITO NCs is reported in **Figure 17** from **Chapter IV**. In homogeneous MO NCs, upon UV exposure, the band-gap onset moves towards higher energies (*i.e.*, Moss-Burstein effect) while the LSPR feature increases in intensity and its peak shifts to higher energies. Further details on the photodoping process can be found in **Chapters IV** and **V**. After the LSPR peak signal reached its saturation, oxidative titrants were added to the photodoped solution of ITO NCs to perform a quantitative analysis of the number of electrons stored by the material. By analyzing the evolution of the spectra upon the addition of precisely calculated amounts of F4TCNQ molecules, it is possible to monitor the appearance of the spectral features related to the dianion formation and, in a

second stage, the appearance of peaks related to the anion and neutral peaks. At the same time, the photodoped NCs progressively return towards 'undoped' conditions. The discharge of the ITO NCs can be detected both in the modulation of the LSPR signal and in the optical band-gap region. Interestingly, a second signal in the band-gap region at around 3.7 eV is visible, which increases in its intensity upon the first titrant additions (orange and red spectra in **Figure 24b**). This spectral signature corresponds to the formation of the F4TCNQ dianion in the ITO NCs/F4TCNQ mixture, as explained below.

VI. 1.1 Plasmon resonance recovery

Figure 24 displays the experimental results of the performed titration on homogeneous ITO NCs. For accurate quantification of the number of electrons withdrawn from the ITO NCs, a titration with F4TCNQ molecules was carried out. In these experiments, a gradually increasing amount of the titrant was added from a 0.3 M stock solution, and subsequently, the absorption was monitored to visualize the formation of reduced F4TCNQ molecules (molar ratio between 88 and 98 mol%, see **Table 1** in **Appendix**). Technical details on the titration procedure are reported in **Chapter III**. The modulation of the ITO NCs LSPR response in the NIR region upon the introduction of F4TCNQ molecules is reported in **Figure 24**a. In this case, the system seems to recover its as-synthesized conditions, with the plasmon feature decreasing in intensity and shifting towards lower energies with increasing amounts of electron acceptors in the solution. These features signal a reduced charge density in the NCs due to the electron transfer to F4TCNQ molecules. As a matter of fact, these titrant-induced modulations have the opposite effect on the LSPR lineshape with respect to photodoping (*i.e.*, blueshift and increase in LSPR intensity). The newly photogenerated and charged-compensated electrons are more energetic than the native electrons present in the NCs due to the aliovalent doping, due to the incorporation of tin atoms in the indium oxide structure, even under rather mild conditions.[22,215] When inspecting the UV-Vis range of the spectrum, as displayed in **Figure 24b,** a second absorption effect can be identified in the ITO NCs. In a similar manner to the LSPR peak, the absorption band edge restores its initial condition by compensating the blueshift derived from the Moss-Burstein effect. After several additions (20 µL), the spectral signature of unreacted F4TCNQ molecules starts to appear. When larger volumes are introduced into the solution, the neutral peak becomes predominant, indicating that (part of) the titrants do not react with the ITO NCs anymore.

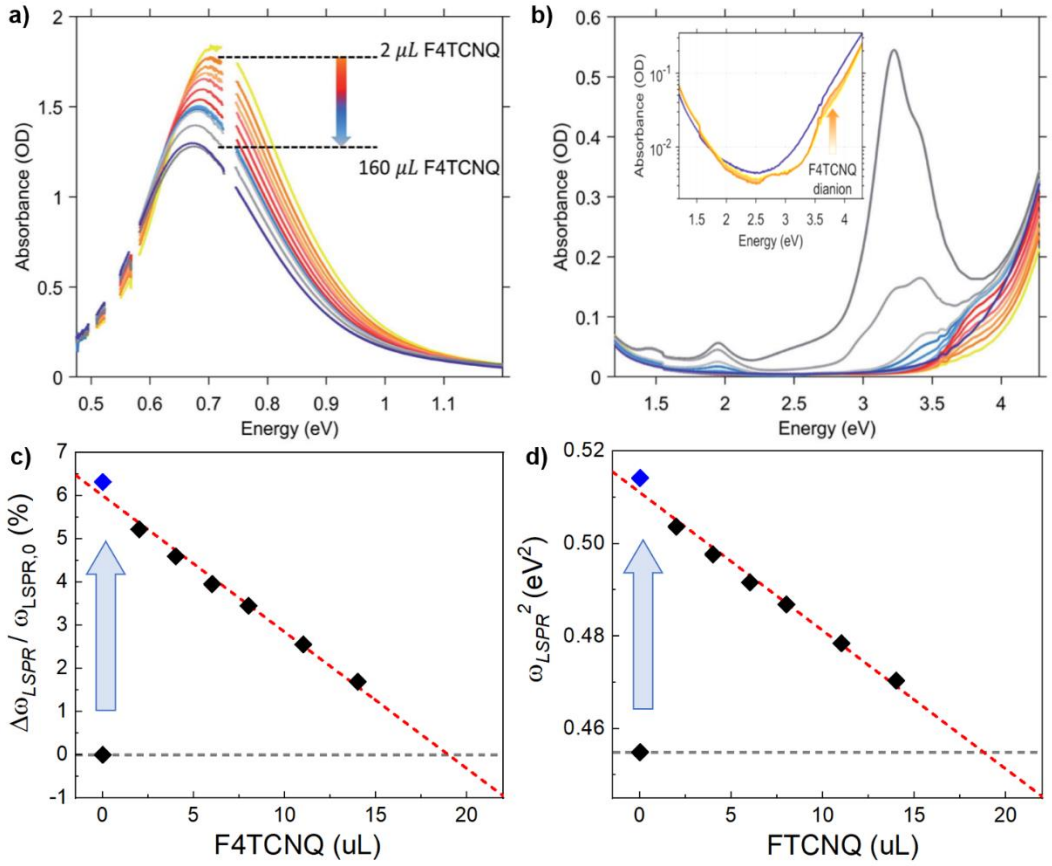

Figure 24 – Results of the oxidative titration of photodoped Sn-doped In_2O_3 (ITO) nanocrystals. a) *recovery of the localized surface plasmon feature to the as-prepared conditions upon adding increasing amount of F4TCNQ molecules.* ***b)*** *Titration effects induced on the ITO bandgap absorption and energy levels of ITO NCs and F4TCNQ. Dark blue and yellow lines in panels (a) and (b) correspond to the as-prepared and photodoped (exposure time: 20 minutes) ITO NCs absorption spectra. During titration, Absorption spectra were recorded after adding a total sum of 2, 4, 6, 8, 11, 14, 17, 20, 23, 26, 60 and 160 μL of F4TCNQ to the photodoped ITO NCs solution.* ***c)*** *Relative variation of the plasmon peak energy after photodoping and* ***d)*** *plasmon peak energy squared as a function of the volume of F4TCNQ added (in μL). In panel (c) $\Delta\omega_{LSPR}$ is defined as $\omega_{LSPR,titration} - \omega_{0,LSPR}$ being $\omega_{LSPR,titration}$ and $\omega_{0,LSPR}$ the plasmon peak energy after a titration step and before photodoping, respectively. At 0 μL, a blue arrow highlights the variations from the as-synthesized and photodoped cases. A linear fit is reported for both panels, pointing towards a recovery of the undoped condition for V~ 19 μL. Figure reproduced from Ref.*[25] *with permission from the Royal Society of Chemistry.*

Furthermore, when large volumes of titrant are introduced in the solution (> 100 μL), dilution effects and the related decrease in signal intensity have to be taken into account. For these reasons, it is reasonable

to restrict the quantitative analysis to the first additions of F4TCNQ molecules. At this stage, modulations of the LSPR peak energy, such as the titration-induced redshift of the plasmon resonance, can be monitored as a function of the volume of titrants introduced: V_t. **Figure 24c** shows the relative variation of the plasmon peak energy $\Delta\omega_{LSPR}/\omega_{LSPR,0}$ after photodoping for each titration step, with $\Delta\omega_{LSPR}$ defined as $\omega_{LSPR,titration} - \omega_{0,LSPR}$. Here $\omega_{LSPR,titration}$ and $\omega_{0,LSPR}$ are the plasmon peak energy after a titration step and before photodoping (*i.e.*, as-synthesized conditions), respectively. **Figure 24** reports the plasmon peak energy squared (${\omega_{LSPR}}^2$) plotted against V_t. In principle, ${\omega_{LSPR}}^2$ is proportional to the carrier concentration n_e and a linear dependence with the number of electrons extracted is expected. In both panels, a horizontal line represents the as-synthesized conditions ($\Delta\omega_{LSPR} = 0$, ${\omega_{LSPR,0}}^2$) and a linear fit of the titration data is provided. The intercept of these two lines point towards a recovery of the undoped condition when a total volume V_t ~ 19 uL is introduced in solution, with a good agreement in both cases. The F4TCNQ equivalents can be obtained as the ratio between the number of moles of F4TCNQ and the number of ITO NCs present in the solution. Then, this ratio is multiplied by the number of electrons transferred to each molecule at each stage of the experiment. The knowledge about the single- or multi-transfer is fundamental to convert F4TCNQ moles into equivalents properly. Hence, the systematic implementation of the spectroscopic analysis of F4TCNQ neutral and ionized species upon titration additions allows to accurately follow the charge extraction process.

VI. 1.2 Evolution of F4TCNQ spectral signatures

As previously discussed, understanding the kind of transfer reaction (*e.g.*, single-transfer, multi-transfer) occurring via titration allows the precise quantification of stored electrons per photodoped NC. The different F4TCNQ species show distinctive spectral features, which are linked to their photo-physics, enabling the characterization of distinguishable oxidative molecular states. The neutral F4TCNQ molecule has a peak maximum at 3.2 eV, the anion a maximum at around 3 eV and two additional peaks between 1.3 and 2 eV, while the dianion instead shows absorption peaks at 3.7 to 3.8 eV. Another feature of this compound is its capability to react via integer charge transfer and/or form charge-transfer complexes.[216,217] Due to the higher reactivity of the ionized F4TCNQ species, reactions between those species and dimerization are possible. [218,219] These intermediate components can generate new optically allowed transitions, appearing in the absorption spectrum along with the previously mentioned species. Hence careful analysis of the data acquired is required.

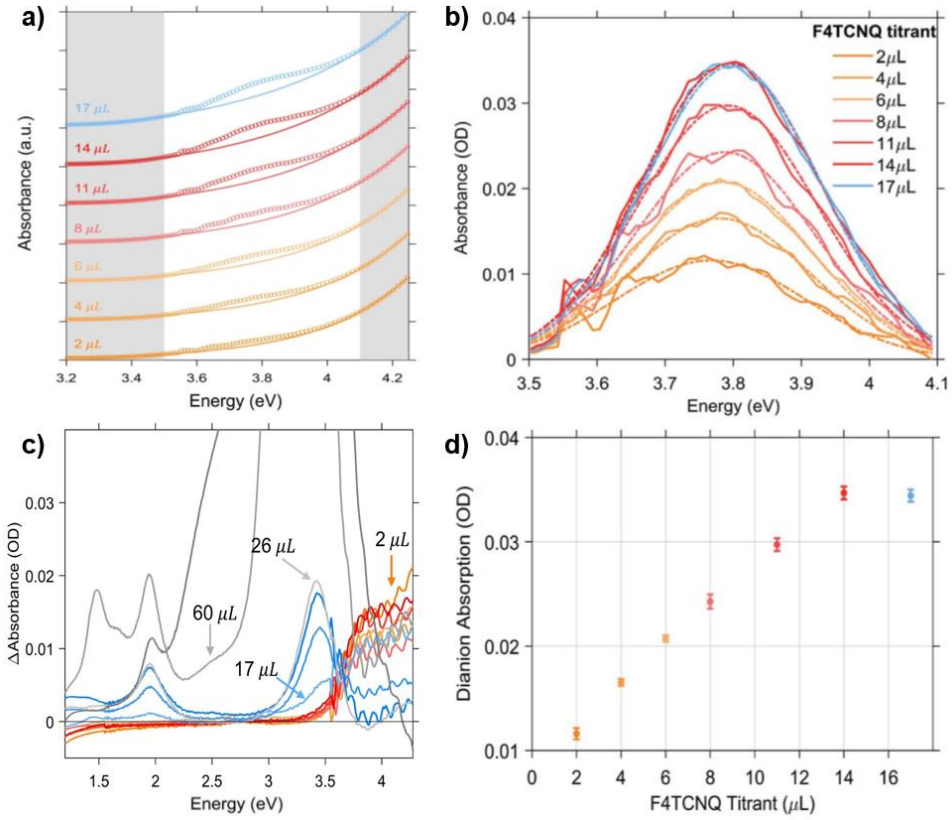

Figure 25 – Evolution of F4TCNQ spectral signatures. a) *Absorption spectra of photodoped ITO NCs after the addition of increasing amount of F4TCNQ titrant solution (0.3mM in anhydrous Toluene). In order to isolate the absorption of the F4TCNQ dianion from the recovery of the band edge we performed a 4th order fit of the absorption spectra. Fitting was performed by taking into account only those data points outside the region of dianion absorption (grey shaded areas).* ***b)*** *F4TCNQ dianion contribution to the absorption spectra of ITO NCs/F4TCNQ mixture. Dash-dotted line are obtained by fitting dianion contribution with a Gaussian function (a).* ***c)*** *Incremental effect of titration on the absorption spectra of ITO NCs/F4TCNQ mixture. Differential absorbance ΔAbsorbance is obtained by subtracting the spectrum from the previous titration step from each curve.* ***d)*** *Dianion contribution increases linearly until the addition of 14μL of F4TCNQ. Figure reproduced from Ref.*[25] *with permission from the Royal Society of Chemistry.*

For this reason, a contribution of all species generated from the charge transfer reaction of the F4TCNQ molecule with the electrons from photodoped ITO NCs can be visualized in the absorption spectra recorded during the titration process. Indeed, this convolution of different species can be seen in the spectra in **Figure 24b**. Both oxidant and reductant signals result in a superposition of features in the UV-Vis range as seen in **Figure 24.** Subsequently, after the addition of F4TCNQ molecules to the photodoped

ITO NCs solution, the unique presence of dianions species was detected in the absorption spectrum. (see inset of **Figure 24b**). For a more accurate analysis of the data, the spectral characteristics of the titrant in the UV range were separated from those of the ITO NCs, by fitting the absorption spectra with a polynomial function considering the ITO band-gap compensation in UV range subsequently after titration (**Figure 25a**). The results of this fit can be seen in **Figure 25b**. After each addition of titrant solution, up to a final addition of 14 μL, the F4TCNQ dianion peak emerges and increases in intensity in the spectrum (**Figure 25d**). This result demonstrates that photodoped ITO NCs are able to transfer two electrons to the titrant, which results in double ionization of the F4TCNQ molecule. This is the first experimental evidence of such multi-charge response from ITO NCs.

Eventually, a saturation of the dianion signal can be reached after a certain amount of titrant has been added to the colloidal solution. **Figure 25c** reports the sequential change of the spectra during the titration process. By subtracting in each curve the spectrum from the previous titration step, the change in the F4TCNQ ionization regime is highlighted. In particular, the neutral F4TCNQ species becomes visible after 14 μL of the titrant was added to the solution, which is a sign of the interrupted transfer of two electrons but also of the ionization itself. An increase of the peak correlated to the anionic species can be observed in the visible range of the spectrum. This suggests that a single transfer of photogenerated electrons can occur even after the double electron transfer mechanism has become saturated. As stated before, it is possible that the F4TCNQ molecule undergoes different types of reactions, ranging from neutralization by back donations and dimerization, as suggested by the presence of an isosbestic point at 3.6 eV between the absorption region of neutral and dianion components (see **Figure 25c**). Hence, the correct interpretation of this last regime of the titration in terms of the number of electrons transferred is not trivial and the disentanglement of the precise set of reactions occurring is left as an open question at this stage. In addition, in this regime, dilution effects can come into play and significantly affect the overall optical response of the mixture.

Electron counting in ITO NCs

By considering the initial concentration of the ITO NCs, the concentration of the F4TCNQ titrant added to induce the appearance of the spectral signature associated with neutral molecules, and knowing that the electron transfer between ITO NCs and titrant molecules occurs with two electrons, the number of electrons extracted per ITO NC can be estimated. The electron counting procedure employed is described in detail in **Chapter III**. Based on the spectroscopic analysis reported in **Figure 25**, the titration process

of homogeneous ITO NCs results in the extraction of approximately 123 electrons per photodoped NC unit. Interestingly, the estimate here performed agrees with estimates based on the relative variation of the plasmon peak energy after photodoping as a function of the F4TCNQ equivalents (**Figure 24c**). The analysis was limited to the range between 0 and 14 μL, where it is possible to safely assume that the double electron transfer process dominates over the mixed regime. As mentioned before, the ratio between the number F4TCNQ molecules and ITO NCs yields to the equivalents per NC; then the obtained number is doubled to account for the double electron transfer. A linear fit of the titration data crosses the as-synthesized conditions $\Delta\omega_{LSPR} = 0$) at a value of ~144 (error +17% with respect to the number of extracted electrons obtained from the analysis of F4TCNQ dianion absorption). The fitting extrapolation of the linear dependence of ${\omega_{LSPR}}^2$ (**Figure 24d**) reaffirms the agreement regarding the number of photoelectrons extracted (142). The results of the analysis of the spectral signatures of F4TCNQ molecules in photodoped core-shell nanoparticles, and related limitations, are reported in **subchapter VI. 2 .**

Given the complexity of the final titration phase, the calculated number is possibly an underestimation of the real number of charges transferred. Independent from this, the here obtained results signal the extensive potential of photodoped ITO NCs as a multi-electron extraction platform. These experimental observations motivate further investigations of these systems. Future studies could consider several factors ranging from the optimization of the system with regards to the used materials and their morphology (i.e. size, shape, level of aliovalent doping), to the operational conditions of the photodoping process, and also to the stabilization of the generated charges with suitable hole scavengers.[78] The perspective of enhancing energy density via multi-charge transfer processes makes MO NCs extremely competitive candidates for the current energy materials research.

VI. 1.3 Photodoping of ITO NCs mixed with F4TCNQ molecules

To verify that the results derive from the reaction between the titrant molecule and the electrons accumulated via photodoping in the ITO NCs, a control experiment was carried out in which the titrant was added prior to photodoping of the sample. As shown in **Figure 26**, this experiment clearly indicates that the addition of the F4TNCQ titrant does not cause any ionization in the as-synthesized NCs, leading instead to the increase of the peak associated with the neutral molecule with each addition of the titrant. It is noteworthy to mention that electrons introduced by tin doping during the synthesis stage are stable carriers that do not participate in the titration event.

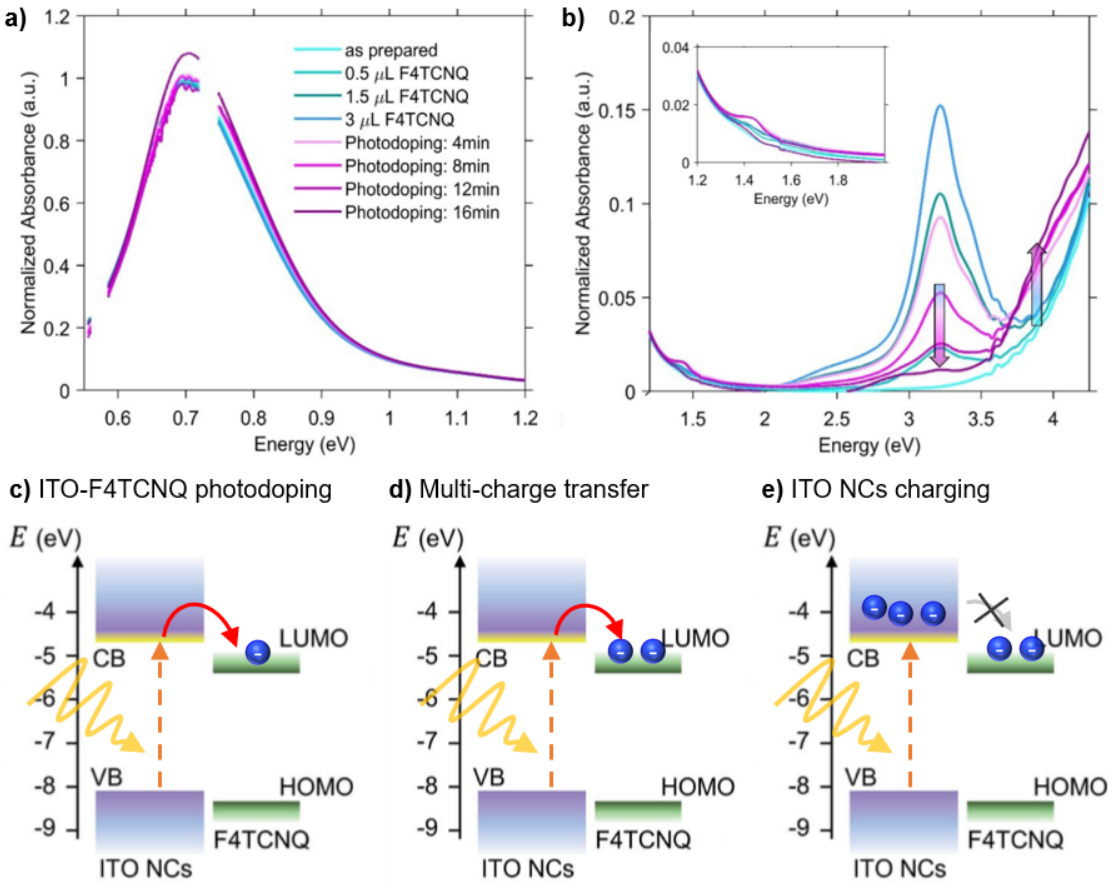

Figure 26 – Photodoping of ITO NCs mixed with F4TCNQ molecules. ***a)*** *Normalized absorbance spectra of as prepared ITO NCs, ITO NCs/F4TCNQ mixture for increasing amounts of F4TCNQ (0.5, 1.5, 3 μL) before any photodoping process. Absorbance spectra in magenta color scale show the effect of photodoping on ITO NCs/F4TCNQ mixture after the addition of 3 μL of F4TCNQ. Panel (a) and (**b**) show the evolution of the spectra in the plasmonic and band gap regions, respectively. Arrows in Panel (b) display the effect of photodoping on the ITO NCs/F4TCNQ mixture. Inset in panel b shows a zoom in the spectral region of F4TCNQ anion absorption. Reproduced from Ref.*[25] *with permission from the Royal Society of Chemistry.* ***c-e)*** *Illustration of a possible dynamics dominating the photodoping process of the ITO-F4TCNQ mixture.* ***d)*** *The kinetic of multi-charge transfer process is faster than the storage of electrons into ITO NCs and, with the timescales used, results in no significative variations in the LSPR lineshape under UV illumination.* ***e)*** *When the charge-transfer process is prohibited, either due to saturation of the reduction power or for the photodegradation of the F4TCNQ molecules, ITO NCs can be photodoped again.*

Furthermore, the mixture of F4TCNQ unreacted molecules and ITO NCs was then illuminated with UV

light as part of a second experiment. Remarkably, under these conditions, the formation of dianionic molecules in the solution is identified while no variation in the ITO plasmonic response is detected. This empirical observation suggests a major difference between the kinetics of photodoping process and the reactivity of the photodoped electrons, with the charge-transfer reaction being clearly favorable (see **Figure 26c** and **d**). Unfortunately, the prolonged UV exposure needed to trigger the photodoping process of ITO NCs also leads to a degradation process of the organic titrant, obstructing precise quantitative analysis of the results of this experiment. Nevertheless, the accumulation of extra photocharges in the ITO NCs can still be achieved in this configuration immediately after the suppression of the neutral peak signal, which can be either caused by dianion formation or photodegradation of the F4TCNQ molecule. As a consequence of the absence of neutral titrant molecules, the typical LSPR evolution of photodoped ITO NCs is detected in the NIR region, suggesting the reversibility and complementary of titration and photodoping.

VI. 2 Charge storage capacity of core-shell nanocrystals

Here, I investigate the electron counting technique based on F4TCNQ oxidative molecules and its limitations when applied on core-shell MO NCs. In particular, electrons counting is performed on the ITO-In_2O_3 NCs introduced in **Chapter IV**. Electrochemical titration has been successfully performed on MO NCs.[14,103,189] Importantly, while analysis based on plasmonic modulations hold for homogeneous ITO NCs, the LSPR lineshape of core-shell MO NCs evolves in more complex ways. Other parameters come into play (such as the frequency dependence of the damping constant and depletion layer modulations), turning the argument more complex for a direct comparison of the number of electrons extracted and out of the scope of this chapter. Hence, in the case of photodoped core-shell ITO-In_2O_3 NCs exposed to F4TCNQ molecules, the most precise quantitative analysis of the photocarriers stored rely entirely on the evolution of the titrants spectroscopic signatures in the UV-VIS region.

Figure 27 reports the electrochemical titration of photodoped core-shell NCs, as a function of the shell thickness. As mentioned in **Chapter 0**, the average number of photoelectrons that can be extracted from each ITO NC can be directly measured using the titration method, with the F4TNCQ molecule acting as the electron acceptor. The number of extracted photocarriers (ΔN_e) increases with increasing shell thickness (t_s), in agreement with what expected from numerical simulations and empirical modeling

(**Chapter V**). The discrepancy observed in terms of absolute values, up to a factor two for large core-shell NCs (**Figure 22b** from **Chapter V**), could be linked to the decreased efficiency in the carrier extraction process for large values of t_s. Nevertheless, the trend $\Delta N_e \sim {t_s}^3$ is replicated. Titration experiments further support the empirical fit model and band structure calculations, validating the approach previously reported. Hundreds of photoelectrons are stored and extracted in photodoped core-shell ITO-In_2O_3 NCs, with values up to almost 400 electrons in the ITO NCs with the largest shell. The quantitative analysis performed here further supports the possibility to optimize the capacity of MO NCs by engineering their electronic structure with depletion layer tuning.

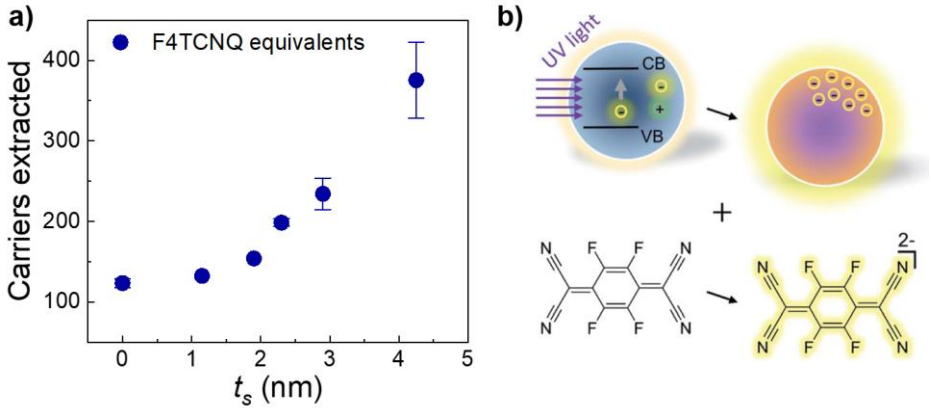

Figure 27 - Charge storage enhancement in core-shell NCs. a) *Number of photoelectrons extracted via chemical titration using F4TCNQ molecules as a function of t_s. The $\Delta N_e \sim {t_s}^3$ trend confirms the results discussed in **Chapter IV**. Figure adapted from Ref.[23] with permission from Springer Nature.* ***b)*** *Multi-charge transfer from photodoped ITO NCs. On the top, photodoping of ITO NCs after the absorption of UV light. Charge transfer of two electrons from the photodoped NC to the LUMO (lowest unoccupied molecular orbital) states of a F4TCNQ molecule is depicted in the lower part of the illustration. Below, a F4TCNQ molecule is turned into the dianion state $F4TCNQ^{2-}$. Figure adapted from Ref.[25] with permission from the Royal Society of Chemistry.*

VI. 3 Chapter summary

To summarize, in this chapter, the possibility to use photodoped electrons of ITO NCs for multiple charge transfer processes via titration with F4TCNQ molecules was investigated. By employing this compound, which can have a single and/or double stable ionization state, the evaluation of the number of electrons

associated with the reduction process in operating conditions can be carried out. The maximum amount of titrants the NC solution can react with was identified from the deconvolution of the optical data. It corresponds to the saturation of the dianion spectral signature and the appearance of peaks related to F4TCNQ molecules in the neutral form. This investigation exposed a number of advantages of the nanocrystal-based system. These results show that photodoped ITO NCs can directly double ionize the F4TCNQ through a two-electron transfer, demonstrating that these highly reactive electrons can be effectively used as multi-electron photocatalysts. This was the first time ITO NCs have shown such an optoelectronic reaction, with the additional benefit of using widely used molecules (F4TCNQ) and not requiring ligand-stripping procedures. ITO NCs resulted to be extremely stable upon charge transfer process, with no degradation effects detected and the initial carrier density concentration, formed by tin doping, is retained. I calculated the number of electrons extracted for the ITO NCs analyzed, resulting in hundreds of electrons released from each photodoped NC, exhibiting competitive values for the next generation high-density batteries. The electron counting technique was successfully applied to core-shell ITO-In_2O_3 of various shell thicknesses. The results, with a number of photoelectrons extracted up to almost 400 in the NC with the larger shell, further support the model proposed in the previous chapter for the optimization of the electronic structure of MO NCs. Finally, the analysis developed in this work for the evolution of spectral signatures of F4TCNQ molecules does not rely on LSPR modulations and, hence, it can be exploited for the quantitative investigations of charging/discharging multi-electrons processes even in non-plasmonic NCs. The photodoping/titration inverse processes provide a non-invasive method to charge/discharge NCs while they retain their stability, making them attractive candidates for the efficient development of light-driven energy conversion/storage applications and for multi-electron photocatalysis.

VII. Light-driven 0D-2D hybrid nanostructures

So far, the photodoping process of doped metal oxide nanocrystals has been shown only in solution and under inert atmosphere, with the additional drawback that the photogenerated holes are lost by reacting with a sacrificial hole scavenger. However, for the efficient exploitation of this process towards the development of an innovative nanostructured material to accumulate, store, and release solar energy, solid-state structures are favorable. In this chapter, I present the light-induced charging of a 0D-2D hybrid system based on Indium Tin Oxide (ITO) NCs and bidimensional Transition Metal Dichalcogenides (TMDs). Thanks to the coupling between the two nanomaterials, all-solid-state photodoping is proven in ambient atmosphere. The extra electrons are stored within the NC layer, while the 2D semiconductor layer, which acts as a solid hole-scavenger, collects the photogenerated holes. After a general introduction of the hybrid system and the results obtained on the light-driven charge separation, the chapter focuses on the possibility of using the 0D-2D scheme for the contactless manipulation of atomically thin 2D materials. As a matter of fact, MO NCs can be employed as all-optical charge injection sources that allow to locally and quasi-permanently modulate the electronic structure of 2D TMDs. The injected photocarriers can travel tens of microns through the monolayer from the excitation spot, accumulating according to the local electronic landscape and altering the photoluminescence spectrum of the 1L-MoS_2 layer. The possibility to precisely localize the charge injection source to the micrometer scale and in the post-fabrication stage empowers the local investigation of unperturbed electronic structure of 2D materials. Thanks to this novel approach, the important impact of sample inhomogeneity on the charge carrier percolation was unraveled. These studies demonstrate that local and contactless charge injection with sub-micrometer precision delivers an alternative route for charge injection and indicates that local 2D material electronic structure can serve as a key element for novel nanoscale device design. Most of the findings reported in this chapter can be found in Ref.[17] and Ref.[18].

VII. 1 Photocharging of a 0D-2D hybrid nanocapacitor

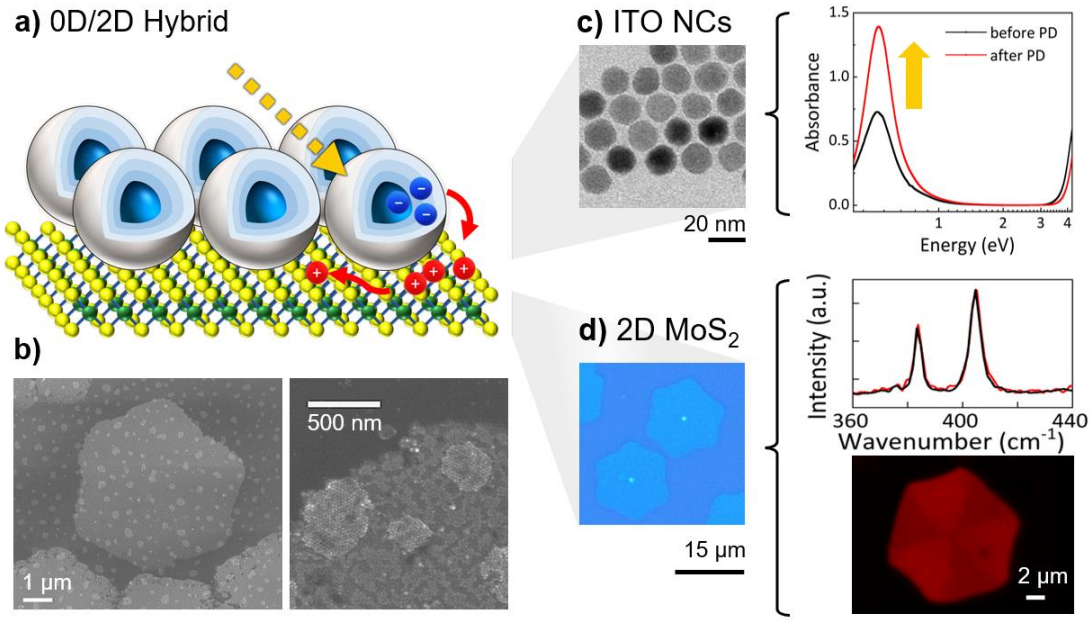

Figure 28 – Hybrid 0D/2D nanostructure. a) *Illustration (not in scale) of the hybrid structure of ITO nanocrystals and 1L-MoS_2. Photogenerated electrons are stored inside the NCs, while the holes are rapidly transferred into the monolayer and diffuse.* ***b)*** *Typical SEM image of the hybrid, with two-dimensional flakes of MoS_2 covered with a thin film of ITO nanocrystals.* ***c)*** *TEM image of ITO nanocrystals. On the right, absorbance spectrum of the ITO nanocrystals in solution, before and after photodoping.* ***d)*** *Typical optical micrograph of the CVD grown 1L-MoS_2 sample. On the right, Raman spectroscopy of a flake without (black line) and with (red line) the nanocrystal layer, the in-plane (E_{2g}) mode and the out-of-plane (A1g) mode located respectively around ~382 cm^{-1} and ~407 cm^{-1}. Below, micro-PL measurement of 1L-MoS_2 flake. Figure adapted from Ref.*[17] *with permission from American Chemical Society.*

The hybrid 0D-2D (ITO-In_2O_3 NCs / 1L-MoS_2) nanostructure analyzed in this chapter is composed of monolayer (1L) MoS_2 covered by a thin film of ITO-In_2O_3 core-shell nanocrystals. Technical information on the nanofabrication of the heterostructure can be found in **Chapter III**. Light with energy beyond the bandgap of ITO generates multiple electron-hole pairs in the NC, via photodoping. The photogenerated holes are rapidly quenched at the surface of NC and transferred to the 2D layer, which acts as solid hole-collector, ensuring a stable charge separation between the two materials (see **Figure 28a** and **b**). The extra photoelectrons are stored within the NC volume, leading to n-type doping of the ITO NCs, while

the corresponding holes are injected into 1L-MoS_2 layer, altering its optoelectronic properties. Multiple charges can be permanently stored with light in the two nanomaterials, effectively photocharging the hybrid system. **Figure 28c** shows a typical TEM image and absorption spectrum of the nanocrystals in solution, before and after the exposure to UV light. Further details on the photodoping of metal oxide NCs, and in particular on ITO-In_2O_3 core-shell NCs, can be found in the previous chapters of this dissertation. **Figure 28d** reports an optical image of the CVD 1L-MoS_2 used, a hyperspectral map of the photoluminescence of a typical flake, and the Raman spectra of the 2D material before and after the deposition of the NCs via spin-coating.

VII. 1.1 All-solid-state photodoping

The 0D-2D hybrid induces the formation of a staggered, type II heterojunction. From an energetic point of view, the coupling between the two materials is fundamental for the charge-separation process, suppressing electron-hole recombination and, ultimately, allowing the light-driven charging of the hybrid. The 2D material acts as an efficient hole collector due to the favorable energetic alignment, with positive charges being spontaneously transferred from the NCs to the 1L-MoS_2 monolayer (see **Figure 29a**). On the contrary, the photogenerated electrons cannot be easily promoted to the CB of MoS_2 and remain constrained within the NC's volume, where they accumulate. Thanks to this coupling, all-solid-state photodoping of MO NCs is achieved.

The light-induced modulations in the 1L-MoS_2 carrier density are monitored via photoluminescence (PL) spectroscopy. Two-dimensional TMDs present unique excitonic properties as a result of greatly enhanced Coulomb interactions and reduced dielectric screening (further details can be found in **Chapter II**).[139] Electrons and holes are tightly bound together by Coulomb attraction with large binding energies of the order of ~ 550 meV and, at the same time, large exciton radii (9.3 Å for MoS_2).[29,139,153,154] Trions, *i.e.*, charged excitons bounded to an additional electron (negative trion) or hole (positive trion), play an important role in the emission of TMDs at room temperature. Remarkably, the system displays the possibility of selective excitation, being the bandgap energies of 1L-MoS_2 and ITO significantly different. The characterization of the system is performed by probing the MoS_2 layer with green light (λ_{ex}= 500 nm, or E_{ex}= 2.48 eV). Under these conditions, it is possible to measure the 1L-MoS_2 PL emission without exciting the NCs. When UV light is employed (λ_{ex}= 350 nm, E_{ex}= 3.54 eV), it triggers the photodoping process in the hybrid and – at the same time – it allows to detect light-induced variations in the 2D material. To conveniently describe the evolution of the PL spectrum, both in terms of energy

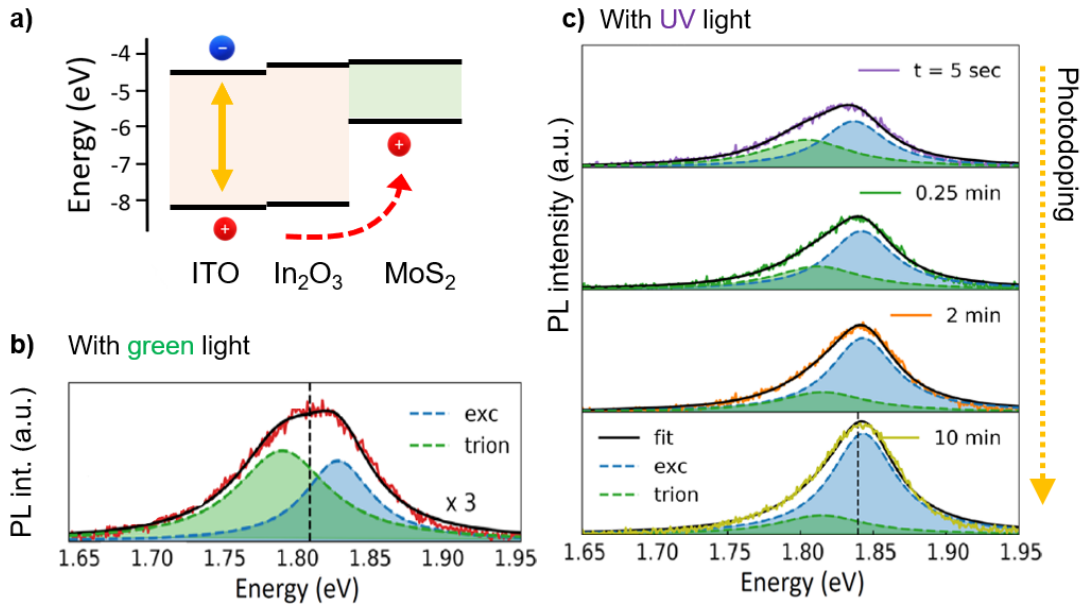

Figure 29 – All-solid-state photocharging of the hybrid nanostructure. a) *Scheme of the energetic alignment of the system. Photoexcited holes generated with light beyond their bandgap inside the ITO nanocrystals are rapidly transferred to the 2D material, while photo-electrons accumulate in the nanocrystal.* ***b)*** *Photoluminescence (PL) spectrum of the 1L-MoS_2 (in red). Spectrum collected with an excitation energy of 2.48 eV (500 nm, no ITO excitation).* ***c)*** *Temporal evolution of the PL spectra of the monolayer MoS_2 with time of photodoping (PD). After photodoping with 3.54 eV (355 nm, above the bandgap of both, the 1L-MoS_2 and the ITO nanocrystals) an immediate blue shift to higher energy is observed (purple curve), which further blue shifts and intensifies with increasing exposure up to 10 min (compare green to yellow spectra). The PL spectra are fitted by the sum (black curves) of two Lorentzian line shapes, which are assigned to emission from the exciton (blue curves) and trion (green curves) states. Figure adapted from Ref.*[17] *with permission from American Chemical Society.*

shift and asymmetric variations of the lineshape, I introduce here the spectral median (SM). The spectral median is defined as the energy that divides the PL spectrum into two regions (high- and low-energy emission) of equal area and can be implemented as a useful indicator of the trion/exciton ratio during the photodoping process. **Figure 29b** and **c** show the 1L-MoS_2 PL spectrum modulation due to photodoping. Upon UV exposure, the PL spectral median blueshifts continuously to higher energies over the course of ~10 minutes. After reaching a maximum shift of 29.4 meV, no further variations in the PL lineshape are detected. Notably, in the first few seconds, a large blueshift (15.9 meV) of the spectral median is observed

(purple line, $t = 5$ seconds). Control measurements were performed on 1L-MoS_2 without the ITO nanocrystals, showing no variations in the PL spectrum of the 2D material (**Figure 42** of **Appendix**).

The comparison between the initial 1L-MoS_2 PL spectrum (panel b) and those after 10 minutes of UV exposure (panel c) highlights that the emission spectrum increases in intensity, its energy blueshifts, and the spectral lineshape changes. Variations in the shape of the PL emission induced by photodoping are compatible with what observed when the free electron density is reduced in electrostatically gated devices[139,168,220] or by locally inhomogeneous dielectric environments.[54,146,167] These light-induced variations are linked to the reduction of the n-type carriers in the TMD monolayer (*i.e.*, p-type light-induced doping) due to the photodoping of the NCs. More precisely, the injected photoholes recombine with the electrons in excess that are naturally present in the TMD layer, suppressing the negatively charged trions. The lineshape of the PL emission evolves asymmetrically due to this variation in the excitonic features. The relative weight of the trion state is immediately suppressed in the very first seconds of the process, indicating rapid and intense initial transfer of photocarriers in the hybrid. The suppression of the trion population is a fingerprint of the MoS_2 photodoping process. These results proved possible, for the first time, an all-solid-state photodoping of doped MO NCs, overcoming the need for an inert atmosphere environment and, at the same time, providing a convenient channel to collect the photogenerated holes. From the deconvolution of the emission peak with two Lorentzian fits it is possible to quantify the exciton and trion contributions to the photoluminescence (**Figure 29**). As discussed in **Chapter II**, the relative spectral weight of the trion state relative to the neutral exciton is acutely sensitive to free carrier density levels of the 1L-TMD.[139,146,167,168] A modified mass action model can accurately describe the dynamic equilibrium of free electrons in bidimensional materials, allowing the quantification of photo-induced variations of the carrier density (n_e) via the spectroscopic analysis of the PL emission (further information on the model can be found in **Chapter III**). By applying this model to the photodoping process reported in **Figure 29**, a decrease in carrier density of ~$6 \cdot 10^{12}$ cm^{-2} is obtained. With this 0D-2D scheme even greater suppressions of n_e, in the order of ~10^{13} cm^{-2}, can be achieved, rivalling the charge density variations observed in single layers of MoS_2 via electrostatic gating.[139,221] The behaviour of the 0D-2D hybrid structure can be modelled as an ideal capacitor consisting of two layer oppositely charged, the NC layer negatively charged and the MoS_2 layer positively charged, separated by an insulating region, *e.g.*, the NC ligands (see **Appendix** for further details). With this approach, the capacitance of a NC-MoS_2 junction results ~6.8 fF and the areal capacitance ~0.86 μF cm^{-2}, with a generated voltage of ~1.18 V in the heterostructure. The photodoping

dynamics of the hybrid structure were investigated beyond the temporal resolution of Ref.[17], as reported in the **Appendix**, showing clear signatures of a two-step process (with a fast and a slow kinetic) in the charging mechanism. Finally, the long-term stability of the light-induced effects in the hybrid were tested (see **Figure 46** in the **Appendix**), showing that the photodoping process is stable up to, at least, 72 days after the transfer of photocharges.

VII. 2 Contactless manipulation of atomically thin 2D materials

Here, I present 0D MO NCs as effective localized light-driven charge injection sources for the contactless manipulation of charge densities in monolayer TMDs, extending theall-solid-state photodoping process to observe the diffusion of the photogenerated holes within the 2D material. Indium tin oxide NCs can be excited locally, within a diffraction-limited excitation spot, transferring photocharges into the 1L-MoS_2. Hyperspectral imaging techniques were employed to spatially resolve variations induced by the photocharging process in the monolayer TMD, with sub-micrometric resolutions. By mapping the hybrid before and after the injection of charges and analyzing the 1L-MoS_2 emission modulations, it is possible to follow the relocation of holes into the 2D materials. This technique allows both the investigation and the manipulation of carriers in 2D transition metal dichalcogenides in a contactless way. Carrier diffusion effects are unveiled and investigated, showing that the vast majority of injected carriers travel long distances away from the micron-sized excitation spot. This work demonstrates a new possibility to manipulate the electronic structure of unperturbed 2D TMDs via photodoping without the need for invasive and broad physical contacts.

VII. 2.1 Spatially-resolved effects of photo-injected carriers

To visualize the impact of photodoping, spatially-resolved images were generated from hyper spectral maps by plotting for each position of the map (*i.e.*, each pixel of the image) the local spectral median (SM) of the 1L-MoS_2 PL. Prior to photodoping, a first hyperspectral map was collected measuring the local 1L-MoS_2 PL emission over the entire extent of the 2D flake (**Figure 30a**) with energy below the bandgap of ITO (*i.e.*, E_{ex}= 2.48 eV). As reported in several works,[142,143,145,149,150,222,223] the PL emission of CVD-grown monolayer MoS_2 is spatially inhomogeneous and, initially, the edge regions of the 2D

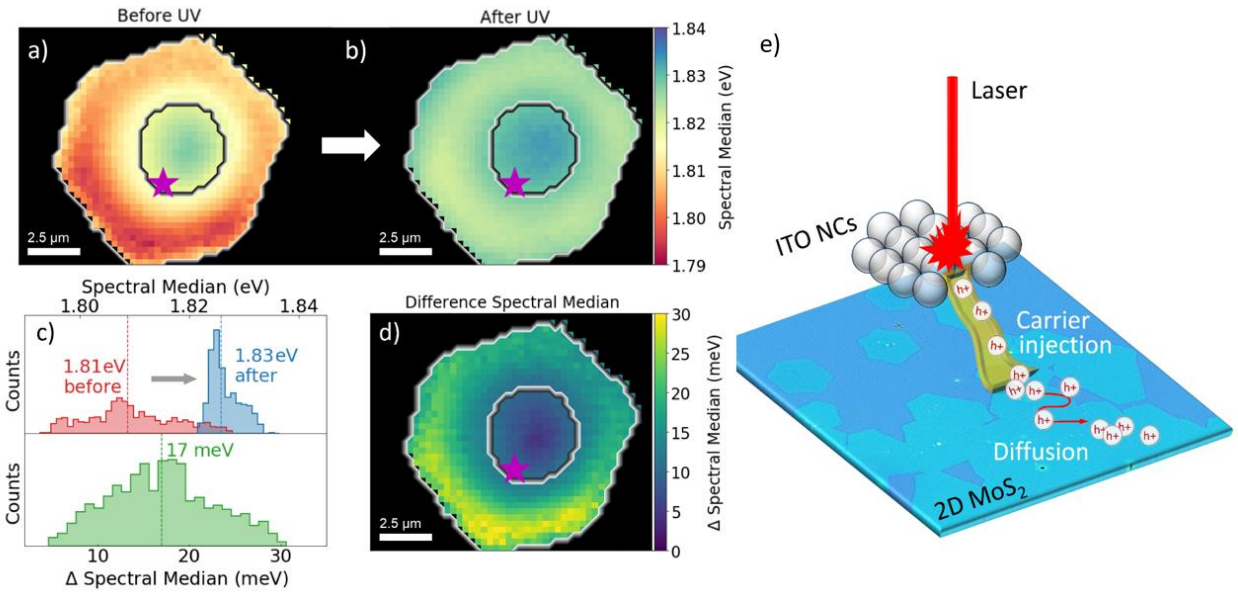

***Figure 30 – Spatial effect of photo-induced carrier extraction in a hybrid NC/MoS2 flake**. **a)** Variation in the spectral median of the PL over a 1L-MoS2/ITO NC hybrid flake a) before and **b)** after exposure to a focused UV laser spot for 5 minutes at the location marked with a star. Substantial differences in the spectral median between the edge and core region of the flake (illustrated by black contours in the plots as guide to the eye) are obvious already before photodoping. **c)** Upper panel: histograms of the PL peak position before (red) and after (blue) photodoping. Lower panel: Statistical summary of the difference in spectral median before and after. **d)** Hyperspectral map of the difference of the spectral median before and after exposure to UV light. The most striking changes are observed towards the edges of the flake with peak shifts reaching 30 meV, while the core region remains fairly unchanged. **e)** Illustration of the contactless injection of carriers into the 2D material. Figure adapted from Ref.[18] with permission from John Wiley & Sons.*

flake present a redshifted spectral median with respect to the inner region. A similar redshifted PL spectrum can be locally caused by higher carrier density values as well as increased strain or defect densities in the edge.[142,150,222,224] The initial characterization of the 0D-2D flake was followed by the photodoping of the hybrid. A localized spot in the center region (indicated by a purple star symbol in **Figure 30**) was irradiated with focused (r < 2 µm) UV light for 5 minutes, triggering the photocharging of the ITO NCs and the charge separation process. Then, a second map of the hybrid, analogous to the initial one (E_{ex} = 2.48 eV), was collected to investigate the spatially-dependent light-induced variations. As reported in **Figure 30b**, after the photodoping process, an increase in spectral median energies of the 2D layer is observed in regions that are several micrometers away from the excitation spot. These parts

of the sample are not directly illuminated and the variations in their carrier density are attributed to diffusion mechanisms. . A summary of the local PL properties of the flake is reported in **Figure 30c** as spectral median histograms. Before photodoping, the 2D layer exhibits a broad distribution of different spectral median (red histograms), with an average value of around ~1.81 eV. After photodoping, the average position shifts to ~1.83 eV (blue histogram) and the distribution of PL emissions significantly narrows. A statistical summary of the difference in spectral median (green histogram) show an average shift in energy of 17 meV, with maximum values reaching up to 30 meV. **Figure 30d** reports the spatially-dependent variations in the spectral median energy of the 1L-MoS_2 PL. Remarkably, the most intense changes in the photoluminescence spectrum occur in the edge region, in parts of the 2D layer that were never exposed to UV light. The localized spot in which the NCs were photoexcited was close to the center of the flake. Nevertheless, the internal region remained unaffected from the photodoping process and the PL spectrum of the spot position itself did not shift significantly (**Figure 42** of **Appendix**). These findings demonstrate that the positive carriers photogenerated within the ITO NCs are not confined to the excitation spot size and they relocate over the entire extent of the MoS_2 flake.

VII. 2.2 Light-induced carrier density manipulation

The relative contributions of excitons and trions to the PL emission of the 1L-MoS_2 is extracted from the fit of each spectrum at each point of the hyperspectral map. Initially, the PL emission of the 2D flake is characterized by a wide distribution of exciton and trion spectral weights (**Figure 31a** and **Figure 31b**, red histograms), owing to the inhomogeneity of the sample. After the photodoping process of the hybrid, the same histograms show an increase in the exciton spectral weight (with the relative decrease in the trion spectral weight) and a generalized narrowing of the distribution (**Figure 31a** and **Figure 31b**, blue histograms). The mass action model introduced above can be applied to analyze the spatially-resolved variations of carrier density over the entire extent of the 2D flake. Thus, for each point of the map, 1L-MoS_2 carrier density levels were calculated before (**Figure 31c**) and after (**Figure 31d**) the light-driven doping process. In the hybrid 0D-2D system, the light-driven hole transfer from the photodoped ITO NCs to the 1L-MoS_2 leads to a strong suppression of the extra carriers in the 2D material. The photodoped flake exhibits a more spatially-homogeneous distribution of carrier concentrations with respect to the initial case, as highlighted by the comparison between the two density maps. A statistical summary of the local carrier density levels of the flake before and after photodoping is reported in **Figure 31e**. After the UV exposure, the initially broad distribution of carrier densities becomes sharper (*i.e.*, more uniform

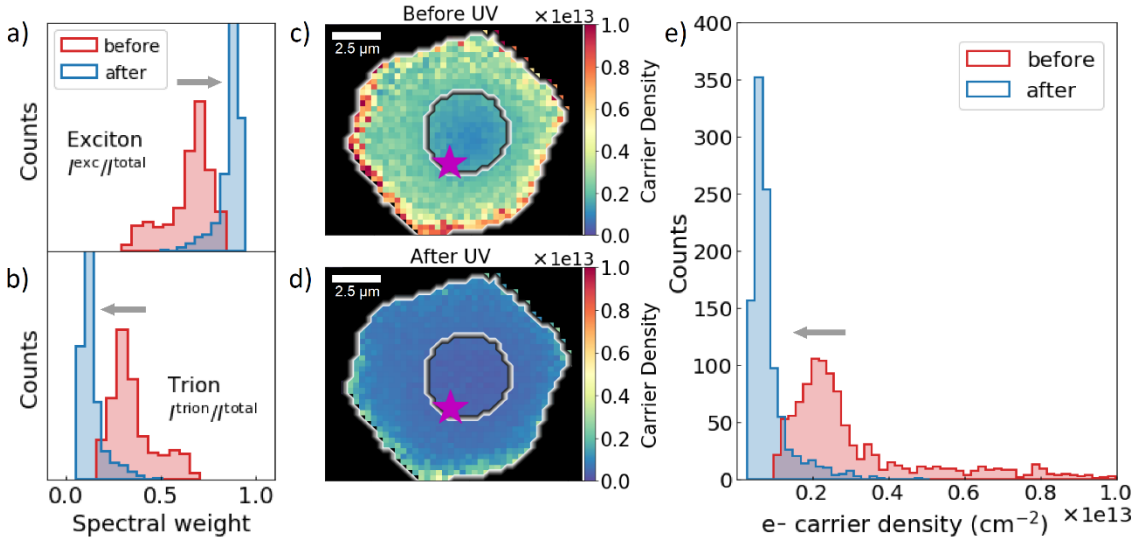

Figure 31 - Carrier density reduction in MoS2 monolayer due to UV photo-doping. a) *Statistical summary of the spectral contributions of excitons and trions to the PL over the entire hybrid NC/MoS2, before (in red) and after (in blue) the photo-doping. Quasiparticle contributions are calculated by fitting the PL emission with two Voigt line profiles and by separately plotting the spectral weight of the exciton (a, upper panel) and trion (**b**, lower panel)**. c)** Illustration of the electron carrier density in the 1L-MoS2/ITO flake before (c) and after (**d**) exposing the hybrid system to UV light. The impact of the photodoping is evident in the sharp reduction of carriers in the 1L-MoS2 flake, leading to a more smooth spatial distribution of the carrier density. **e)** Variation in the electron carrier density before (red) and after (blue) the photodoping. The initial broad distribution shifts significantly and flattens onto low carrier density values (n<1012 cm-2) due to the injection of photo-holes in the system. Reproduced from Ref.*[18] *with permission from John Wiley & Sons.*

flake), and the free-electron levels drop to low values (n_e < 10^{12} cm^{-2}). The resulting average variation in carrier density is Δn_e~-2.3·10^{12} cm^{-2} with peaks in the order of 1·10^{13} cm^{-2}. Similar results were observed by varying the illumination spot position in several flakes of the hybrid system (**Figure 43**, in the **Appendix**), showing that the photodoping process and the consequent carrier density manipulation of the 2D TMD do not depend significantly on the local injection point. As summarized in **Figure 44** (**Appendix**), the photodoping process induces spatially-inhomogeneous variations in the PL intensity too. While the average intensity increases in terms of absolute counts almost in every part of the 2D material, the greatest variations (in percentage terms) occur in regions initially rich in trion concentrations. This can be explained by the higher quantum yield of excitons with respect to trions.[139,168] The photo-injected holes tend to recombine with the extra electrons naturally present in the 1L-MoS_2,

hindering the formation of negatively charged excitons (*i.e.*, trions). In this context, trion suppression via photodoping is reported as an effective tool for PL intensity enhancement, increasing the overall emission efficiency.

VII. 2.3 Long-range diffusion of photo-injected carriers

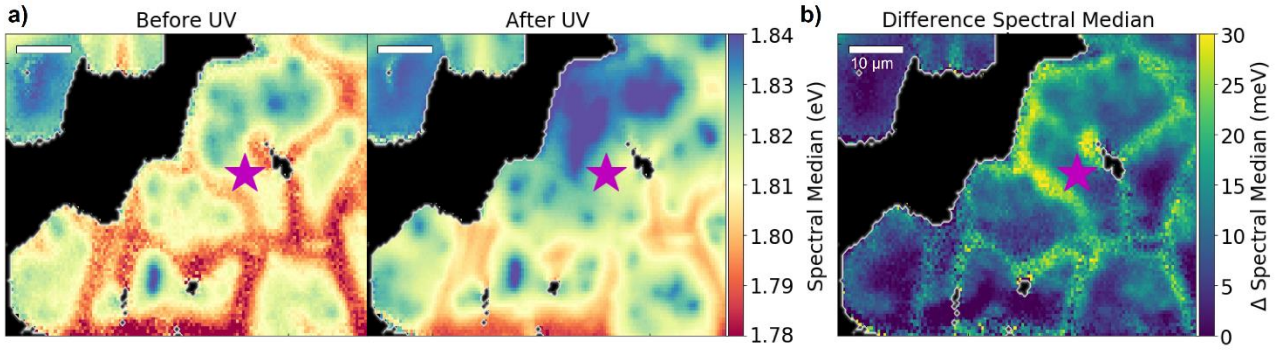

Figure 32 – Long-range diffusion of photo-injected carriers. a) *Spectral median of a large area of the 1L-MoS2/ITO hybrid with multiple connected flakes before (left) and after (right) the exposure to the UV laser source. Photo-doping was performed at the purple colored star in a micrometer-sized spot. Scale bar = 10 µm.* ***b)*** *Map of the photo-induced variations of the spectral median of the 1L-MoS2 PL, reaching changes of more than 30 meV. The impact of the photo-injected carriers into the 2D material is not spatially uniform and it is stronger along edges and grain boundaries of the flake. Figure adapted with permission from Ref.*[18] *with permission from John Wiley & Sons.*

Further study to clarify the spatial extent of the relocation of photocarriers in the 0D-2D hybrid was conducted in a large area (~ 40×60 µm^2) of polycrystalline 1L-MoS_2. This part of the heterostructure is formed by a continuous monolayer TMD film composed of multiple 2D flakes that have merged together during the CVD growth process. This network of micron-sized crystalline domains is characterized by internal grain boundaries between flakes. In analogy to what was described before, hyperspectral maps of the 1L-MoS_2 area were collected before and after the photodoping process, which was triggering only in a localized spot with a focused UV laser (purple star in **Figure 32a** and **b**). Variations in the 1L-MoS_2 PL spectral median energy up to 30 meV were observed over impressive distances, farther than 40 µm away from the micrometer-sized excitation spot (**Figure 32c**). Interestingly, the light-induced variations are not spatially uniform. Greater values of blueshift in the spectral median spatially coincide with the grain boundaries of the MoS_2 flakes network, suggesting the photo-injected carriers tend to accumulate

in these regions. Grain boundary regions are found to be also the areas with the highest trion populations pior to the photodoping process, characterized by an initially low spectral median energy.

Driving force of the relocation

More generally, larger variations in the 1L-MoS_2 PL emission are observed in areas with higher ratios of trion spectral weight, regardless of the distance from the excitation spot. Further analyses on the light-driven effects over long distances were performed by extracting the local carrier concentrations before and after the injection of additional photocharges. A statistical analysis of the magnitude of carrier modulations (normalized counts) plotted against the distance from the charge injection location is reported in **Figure 33a**. Remarkably, charge density variations in the order of $\sim 1 \cdot 10^{13}$ cm^{-2} are detected at more than 40 μm of distance from the excitation spot. Furthermore, no evidence of correlation between Δn_e (carrier density changes) and the distance from the injection source is found, indicating that distance is not the limiting factor in the relation and accumulation of photocarriers into the 2D layer. **Figure 33b** shows the modulation in the carrier density levels (after photodoping) plotted against the initial carrier density for each point of the map. The large area involved in the analysis, composed of several flakes merged together, provides a broad set of structural and electrical conditions (*e.g.*, different natural levels of doping, strain, defects), strengthening the study. Notably, the maximum variation in carrier density that can be achieved exactly coincides with the initial carrier density for all values of carrier concentrations. The striking 1-to-1 linear relation between the maximum variations in carrier density and its initial concentration (highlighted with a dashed line in **Figure 33b**) suggests that each point of the 1L-MoS_2 tends to return to intrinsic doping conditions, irrespective of the distance from the excitation spot. With this scheme, by triggering the photodoping process in a micrometer-sized excitation spot, it was possible to lower the carrier density of 2D material back to intrinsic conditions ($\sim n_e < 2 \cdot 10^{12}$)[183,225,226] in an area larger than 2200 μm^2. In classical electrostatic devices, the diffusion of charges is driven by an electric field generated by a back-gate (in electrostatic gating) or with physical electrodes (for electrical contacts). In this case, however, carriers are injected without a pre-determined driving force (*i.e.*, in the absence of a generalized electric field). Moreover, conventional transport techniques introduce averaging effects over the volume of the contacts or the area of the back-gate. The lack of a pre-determined current path presented in this scheme might allow to extract local values of resistivity in real time, going beyond what is possible with traditional transport measurements. Here, I hypothesize that the relocation of the photodoped charges in the hybrid is driven by the initial 1L-MoS_2 local carrier

concentration. In this picture, the photo-injected holes diffuse in the 2D layer until they annihilate the extra electrons naturally present in the hybrid.

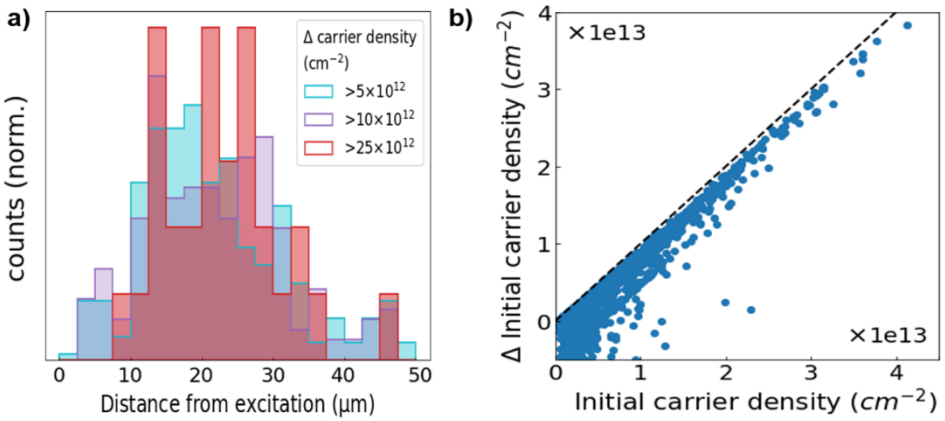

Figure 33 – Annihilation of naturally present extra charges via photodoping. a) *Normalized statistical correlation of the magnitude of the change in the initial carrier density (Δ) with the distance from the excitation spot. Significant variations reach distances of more than 40 μm, and that the magnitude of Δ is not strongly correlated to the distance from the point where photodoping was conducted.* ***b)*** *Reduction in the carrier density as a function of the initial carrier density of the 1L-MoS2. The striking 1-1 linear relation between the maximum charge density variations induced and initial concentration of extra charges suggests that it is possible to completely undope the monolayer and restore a zero-doping condition in the semiconductor, regardless of the initial carrier concentration or of the distance from the excitation source. Dashed line shows the y = x function, as a comparison. Figure adapted with permission from Ref.*[18] *with permission from John Wiley & Sons.*

This theory consistently explains most of the experimental results presented. However, some aspects of the dynamic of the system are yet to be clarified. Ideally, a perfectly smoothed carrier density landscape could be expected in the 2D flake after photodoping. In practice, inhomogeneities in carrier density (and spectral medians) remain present. Several contributions could lead to the observed deviations, given the acute sensitivity of 2D-TMDs to the local effects such as defect densities (*e.g.*, S vacancies), variations induced by the substrate, and strain.[145,150] Lower values of tensile strain are identified via micro-Raman spectroscopy in the edges and other regions of the 2D sample (**Figure 45** in the **Appendix**).[144,173] Several works in literature investigated the effect of strain on the band structure of TMDs, [145,173,174,223,224] indicating that tensile strain relaxation leads to an increase in the energy of the quasiparticles.[173] While a similar increase in the VB energy would provide a driving force for electrons in correspondence of edges

and grain boundaries,[144] the variations in the SM energy observed in this work involves significantly larger areas than those affected by sharp variations of mechanical strain. This suggests that the electronic structure of 1L-MoS_2 changes more gradually, not only in the proximity of edges. An additional explanation for the inhomogeneity observed is the possibility that the photodoping process of the hybrid was not completely saturated after the 5 minutes of UV exposure. This would also explain the deviations from the 1-1 linear relation of **Figure 33b**, between initial carrier density levels and maximum variations achieved, indicating that the number of photo-holes introduced was not sufficient to compensate for all extra electrons initially present in the 2D layer. Hence, the time of UV exposure and the power employed could represent a limiting factor to the maximum area affected by photodoping.

Finally, the number of carriers injected from the ITO NCs into the 1L-MoS_2 was estimated (further details on the quantitative approach employed can be found in the **Appendix**). For the area reported in **Figure 32** an average number of q^{NC} = 75 photocarriers per nanocrystal was calculated, corresponding to 75 photoelectrons stored in each NC and 75 holes injected into the 2D layer. The previous work introduced in **Chapter VII. 1** estimated an average of only ~5 carriers stored per NC by analyzing the light-induced variations at the excitation spot, considering only the region of the sample directly probed by the focused UV laser.[17] This indicates that the vast majority of the transferred carriers relocate far from the excitation spot and further supporting the importance of charge diffusion in the system. By further optimizing the 0D charge injection sources (for example, by optimizing the electronic structure of core-shell ITO NCs) higher values of injected carriers and doping could be achieved with this contactless scheme.

VII. 3 Chapter summary

In this chapter, a novel 0D-2D hybrid heterostructure displaying light-driven capacitive charging was reported. The coupling between ITO NCs and 2D TMDs allows to absorb and convert the energy of the incoming light in extra charges confined within the ultrathin heterostructure. All-solid-state photodoping of MO NCs was achieved in ambient atmosphere, with the additional benefit of collecting photogenerated holes. Upon illumination, the TMD layer collects the positive charges and the MO NCs the negative ones, showing capacitor-like charging behaviors with capacitances values in the fF range. By employing ITO NCs as 0D charge injection sources, it was possible to transfer into the 1L-MoS_2 more than 75 photoholes per NC, reaching unprecedented charge transfer capabilities. Furthermore, the charge transfer

process was proven to be stable for at least 72 days, a timeframe not observed in other photodoping techniques.[227–229] Charge density variations in the order of $\sim 1 \cdot 10^{13}\,cm^{-2}$ were achieved, proving the photodoping scheme as an efficient and competitive alternative to electrostatic doping. The light-induced variations were detected at surprisingly long distances, up to more than 40 μm from the injection source. By triggering the photodoping process in a micrometer-sized excitation spot, it was possible to lower the carrier density of 2D material back to intrinsic conditions ($\sim n_e < 2 \cdot 10^{12}$ cm^{-2}) in an area of more than 2200 μm^2. The 1-1 linear relation between the initial carrier density and its maximum variation indicates that every part of the 1L-MoS_2 uniformly tends to return to intrinsic doping conditions, regardless of the distance from the injection source. The scheme presented in this work is an effective all-optical tool to locally induce p-type doping in 2D TMDs semiconductors. The importance of local inhomogeneities in the charge relocations and in the PL emission of 1L-MoS_2 was reported, showing that the impact of strain, defects densities, and the presence of charge localization effects, which might negatively impact device performance, can be examined via the photodoping of MO NCs. Along this direction, the local manipulation of 2D semiconductors could lead to the design of novel nanoscale devices to target specific materials features.

The proposed tool for the light-induced injection of photocarriers opens the possibility to locally investigate transport processes in 2D semiconductors and remotely manipulate their electronic structure. The key innovation introduced from this work is the contactless nature of the scheme, as the charge injection is provided with light by exciting the ITO NCs in a localized spot. I identify here some of the main advantages of this approach. First, the fabrication step of bulky contacts and electrodes can be avoided. The diffusion and accumulation of charges reported in this work occur freely according to the unperturbed electronic structure of the material, a feature unique to this technology. Second, the injection of carriers is localized to a single spot with micrometric precision, determined by the positioning of the laser anywhere on the sample after the fabrication stage is completed. Third, the charges introduced into the 2D layer are not forced to any pre-determined current path. This all-optical scheme could allow the study of carrier diffusion effects and optoelectronic properties in native, undisturbed bidimensional materials. Future work could further investigate light-driven dynamics in solid-state, from the photocharging and transfer dynamics of the nanocrystals to the diffusion of the injected extra carriers into the 2D material. Further p-type doping could be achieved by using a combination of optimized materials systems (*e.g.,* optimized ITO NCs) or by externally tuning the 2D material. For example, experiments conducted with electrostatically gated devices could provide control over the electronic

landscape of the 2D TMD and its trion concentrations, creating a favorable environment for the detection of even greater modulation in the carrier density upon photodoping. Furthermore, the reversibility of the photocharging process and the recovering the original state of the monolayer could be experimentally investigated.

VIII. Perspectives of photodoping towards applications

VIII. 1 Light-driven energy storage solutions and future applications of photodoped MO NCs

The ability to integrate both energy harvesting, energy conversion, and energy storage into a single nanosized material system could lead to disruptive innovations in the field of light-driven energy storage and self-powered devices. Currently, light-driven rechargeable devices rely on the incorporation of solar cells or photoelectrodes for the conversion of photons and separate units for the accumulation of charges.[9] Metal oxide nanocrystals are promising platforms to combine all these aspects in a unique nanomaterial, including light absorption, stable charge separation, and multiple charge accumulation processes.[15] Moreover, the photocharging process could be exploited in combination with additional features of MO NCs, such as tunable NIR plasmonic resonances and the capability of triggering multiple charge transfer reactions. Multiple technical analyses have been conducted over different energy storage schemes and technologies, comparing the advantages and criticalities of various solutions.[230–236] Two major complementary approaches have arisen in recent years, depending on the timescales involved and the underlying technical necessity. High-performance devices have been engineered to store energy for extended periods of time, such as batteries, and to provide great amounts of power concentrated in short times, such as supercapacitors. Several aspects are taken into consideration while evaluating their optimal design for each configuration. Their performances can be evaluated in terms of efficiency, energy capacity, energy density (*i.e.,* energy stored per volume or mass unit), power density (*i.e.,* speed of the energy transfer per volume or mass unit), response time, operational lifetime (*e.g.,* in years and cycles), and self-discharge.[231,234,237] Batteries have become a fundamental part of modern electronics and several technologies have been developed, ranging from lithium-ion (Li-ion), sodium-sulfur (NaS), nickel-cadmium (NiCd), lead-acid (Pb-acid), lead-carbon batteries, to zebra (Na-$NiCl_2$) batteries and redox flow batteries, which hold promising perspectives for large-scale energy storage solutions.[233,238] On the other side, it is possible to categorize capacitors as electrostatic capacitors, electrolytic capacitors, and supercapacitors (SCs), with SCs having the highest capacity per unit volume due to their operational principles (further information can be found in **Chapter II**).[237,239] The previous chapters of this work extensively discussed the photocharging properties of MO NCs, both from a theoretical and experimental

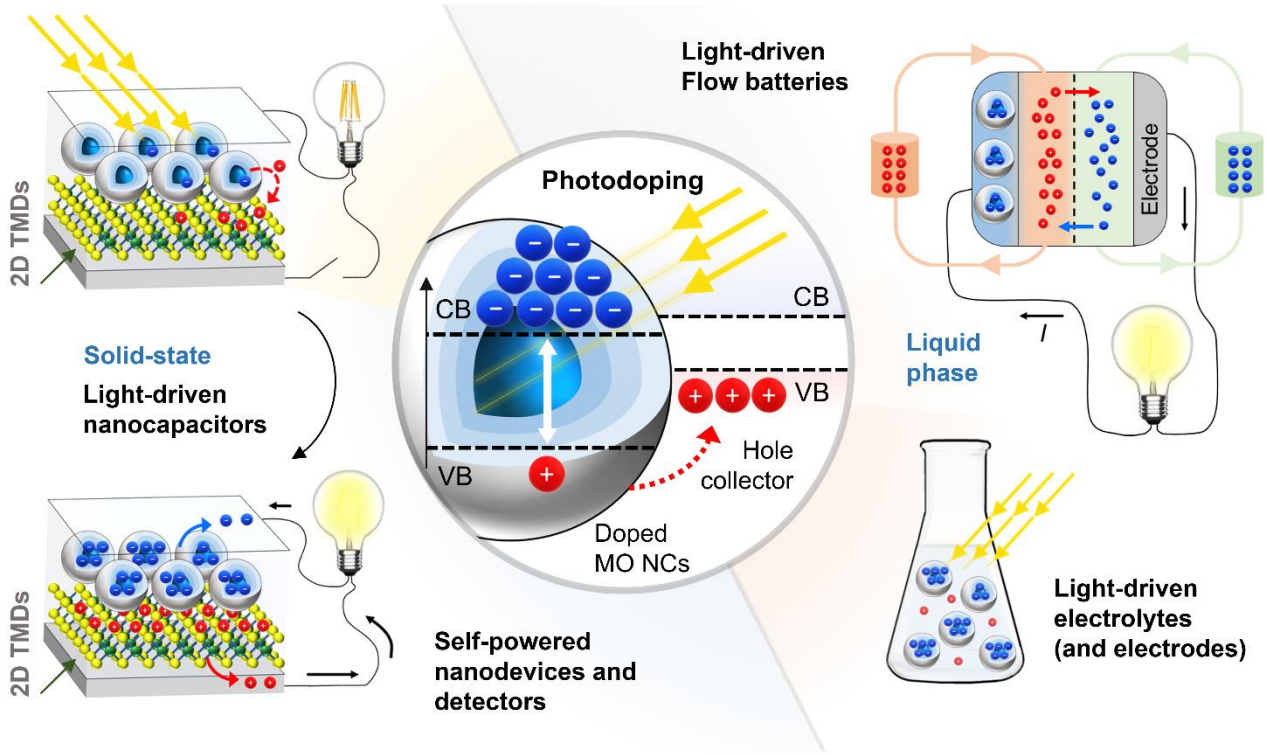

Figure 34 – Possible architectures for light-powered energy storage solutions and light-driven nanodevices based on the photodoping of doped MO nanocrystals*. On the left side: All-solid-state light-driven capacitor based on the coupling between MO NCs and a monolayer 2D Transition Metal Dichalcogenides (TMDs). Center: Illustration of photodoping in the presence of a hole collector with proper band alignment. Light triggers the photodoping process and photo-generated charges are transferred to the hole collector. On the right side: possible application of MO NCs in solution illustrating a light-driven flow cell battery architecture (on top) and light-charged MO NC-based electrolytes. Figure reproduced from Ref.*[15] *with permission from the Royal Society of Chemistry.*

perspective, highlighting their potential as light-driven supercapacitors. Owing to the novelty of these findings, the photodoping scheme still has to be converted to fully-operating supercapacitive technologies and, up to date, only a limited number of proof-of-concept MO NCs-based devices have been investigated. I anticipate significant advancements in the upcoming years, with critical breakthroughs in the development of optimized devices for high-performance and long-lasting light-driven energy storage solutions. Research works conducted in the last decade highlighted the benefits of employing nanomaterials in the energy sector, with energy storage advantages rising from high packing density, high surface-to-volume ratio, and short diffusion pathways.[13,41,43,230,232] In particular, nanocrystals could be implemented to achieve simultaneously high energy and high power densities.[41]

This promising perspective, combined with the possibility of light-driven charging, can open avenues to novel renewable energy storage designs. Here, I delineate possible architectures for light-powered energy storage solutions based on the photodoping of MO NCs, both in liquid-phase and solid-state configurations (**Figure 34**).

Liquid-phase energy storage applications of photodoped MO NCs

A first promising opportunity arising from the photodoping process of MO NCs is the possibility to develop light-driven electrodes (**Figure 34,** right panel). The electrode's design is a critical aspect for the efficient storage functionality of liquid-phase systems. In particular, by increasing the electrode/electrolyte interface area is possible to reach high specific capacitance values. The implementation of MO NCs as electrodes would benefit from the high surface-to-volume ratios and atomically-thin charge layer separations occurring at the SC's surface and, hence, high energy density values are anticipated.[13,14,237] For the efficient implementation of supercapacitors, state-of-the-art devices often involve the design of 3D architectures where micro-supercapacitors are incorporated in a three-dimensional matrix to maximize the total active surface. In opposition to traditional flat systems, a 3D structure of anodes and cathodes would further benefit from nanostructured morphologies, such as nanocrystals, nanowires, nanotubes, nanosheets, and nanowalls.[10] The same principle could be exploited in the development of MO NC-based electrodes to design specific capacitances after light absorption. For the successful implementation of MO NCs as electrodes, further advancements in material design are needed to address additional requirements of this configuration, including high ionic adsorption capacity at the solid-liquid interface, fast and reversible surface redox reactions, fast charge transfer, as well as high conductivity.[10] The ability of photodoped MO NCs to trigger multi-charge transfer reactions is a valuable advantage of this scheme. In detail, the specific capacity (Q) directly correlates to the number of electrons N_e involved in the reaction: $Q = NF\ /\ M$ (where F is the Faraday constant and M the low molecular weight). Multiple charge transfer processes are widely regarded as key tools for the achievement of high energy density in batteries. Hence, MO NCs, exhibiting multi-charge transfer capabilities and supercapacitive photocharging dynamics, are promising high energy density candidates for the next-generation of energy storage devices. Currently, stability issues and the formation of highly-reactive species during charge transfer limit the development of multi-charge transfer components.[121,240] Owing to the delocalization of the photoexcited carriers,[69,122] superior stability properties could be achieved in MO NCs. Long service-life devices could be particularly valuable when operating in remote

places is needed. Another interesting perspective for the photodoping of MO NCs in solution is the development of functional light-driven nano-inks. In a similar technology, the colloidal solution of MO NCs would act as a light-driven energy-carrying electrolyte.[241]

The implementation of light-driven MO solutions in flow batteries would open avenues to visionary applications, such as the development of solar rechargeable flow-cell systems.[242] In flow cell systems, the electrode and the charge-bearing electrolyte are spatially separated, allowing the individual tuning of energy and power densities (**Figure 34**, right panel). Depending on the architecture designed, MO NCs could be employed both as light-driven electrolyte (*e.g.*, MO nano-inks), constituting the charged liquid moving through the well-established device compartments of flow battery systems, or as light-driven electrodes, charging the moving electrolyte via photodoping. As shown in this work, the electrons stored in photodoped ITO NCs can be efficiently extracted by widely-employed oxidative molecules, such as F4TCNQ. Non-invasive charge-transfer reactions can be implemented simply by the mixing of the two solutions. In flow batteries, this process could occur at the interface between the two charged liquids. Given the stability of the nanocrystals, the implementation of multiple reversible charge/discharge cycles is foreseen in liquid setups based on the coupling between charged MO NCs and similar molecules. However, the liquid-phase approaches proposed so far display a significant drawback: the loss of the photogenerated hole during the photodoping process. By reacting with sacrificial hole scavengers, half of the photogenerated carriers are not allowed to contribute to the stored energy, corresponding to a loss of half of the light energy converted. This important aspect could be solved with the design of appropriate hole collection mechanisms. For example, adequate molecules or nanostructured materials could be employed to capture the photogenerated holes in solution and, in a second stage, release the stored carriers to appropriate electrodes when energy is needed. Another strategy for the collection of both photocharges in a fully functional light-driven device comes from the incorporation of MO NCs in solid-state architectures.

Solid-state photocapacitor based on MO NCs

As reported in **Chapter VII**, two-dimensional transition metal dichalcogenides (2D TMDs) were successfully employed as hole-collector in an all-solid-state heterostructure, facilitating the charge separation and photodoping process of ITO NCs. This work showed the stable accumulation of multiple photogenerated electrons in the NC film, acting as a negative electrode, and the accumulation of the corresponding holes in the 2D layer, representing the positive electrode. By applying a capacitor model,

promising capacitance values and areal capacitances in the range of femto Farads and μF cm^{-2} were reported, as well as energy and power densities of the order of μJ cm^{-2} and μW cm^{-2}. Remarkably, these values were estimated without considering diffusion effects; hence, greater values are expected. A detailed discussion of the hybrid system can be found in **Chapter VII**. The practical realization of a light-driven nanocapacitor based on MO NCs is foreseen. However, for a fully functional, photocapacitor device the implementation of functional charge extraction electrodes is required (**Figure 34**, left panel). Additional layers of conductive materials, such as transparent conductive oxides (*e.g.*, bulk ITO) or gold contacts, could be integrated into the final structure, optimizing the carrier extraction process of both photoholes and photoelectrons. The relative energetic alignments between the conduction band minimum and the valence band maximum of the electron and hole collectors, respectively, define the potential achievable in the device. In this case, an expected cell voltage of around ∼1.2 V was reported. This first estimate raises important considerations on the role of the hole collector's electronic structure and its desired properties. More specifically, the potential output of the fully-operating photocapacitor device is expected to depend significantly on the relative band alignment. As a strategy to achieve efficient light-driven charge separation, the engineering of the band offsets of the materials involved is foreseen (**Figure 34**, central panel). For example, single layer TMD can be engineered by several means (*e.g.*, changing dopant concentrations, material, applying electric fields or mechanical strain) to enhance the energetic alignment responsible for the permanent charge transfer from the NCs. More generally, multiple semiconductors could be employed to generate a type II heterojunction in the hybrid system and the full library of suitable materials still requires thorough investigation, highlighting the importance of further materials' research on photodoped MO NCs.

The implementation of a MO-based photocapacitor would stand on the recent discovery and optimization of light-driven supercapacitors (see **Chapters IV-VI**). The development of a first proof-of-concept device could definitively demonstrate the feasibility of such innovative technology, allowing the characterization of the performances of this new type of circuitry element in terms of charge/discharge cycles, efficiency, and storage capacity, reaching a broader audience and igniting further research on the topic. Performance analyses on the light-driven nanocapacitor have to be performed to test critical parameters such as areal and volumetric capacity, the efficiency of the light conversion process, life cycles, speed of the charging and discharging processes, and robustness to different environmental conditions. According to the performance results, different geometries can be fabricated, such as flat multi-layered structures or more complex architectures involving 3D matrices of NCs. Here, the proposed

perspectives display the implementation of the photodoping process of MO NCs in proper device architectures as a promising and viable pathway for novel light-driven energy storage solutions.

VIII. 2 Further perspectives of photodoping and open issues

Apart from energy-related applications, the photodoping process of MO NCs presents a rich variety of opportunities for several different applications. For example, the capability of photodoped MO NCs to trigger multiple charge transfer reactions with light is a valuable feature in the field of photocatalysis. As a matter of fact, metal oxide NCs such as ZnO and TiO_2 have been widely employed for heterogeneous catalysis[99,208] and, hence, the optimization of the photodoping process (*e.g.*, via depletion layer engineering) would have beneficial implications on existing photocatalytic applications. Furthermore, MO NCs could find implementation in the field of nanomedicine. Due to the possibility to non-invasively target biological tissues and interact at the sub-cellular level,[243] nanoparticles have been extensively investigated for biomedical applications ranging from diagnostics (*e.g.*, imaging, detection) to therapy (*e.g.*, hyperthermia treatments, drug delivery).[35,36] Only recently first results showed that NCs have the potential to electrically charge the cellular environment and to alter the excitability of single neurons.[34] The wireless charging of MO NCs could find unexpected applications in the field of electrophysiology, with the perspective of developing light-driven control over the activation of neurons. More conventionally, MO NCs can be exploited within existing strategies for hyperthermia treatments, due to the strong plasmonic resonances, or functionalized for drug delivery techniques. Optoelectronic nanodevices would strongly benefit from the incorporation of photodoped MO NCs. Their ability to dynamically modify carrier density levels in doped semiconductors could be employed for modern transistor designs, replacing the gate input with light or even for the fabrication of all-optical-input transistors.[244] In **Chapter V**, dynamic control of electronic band profiles and depletion layer engineering was presented, allowing the design of MO NCs with targeted optoelectronic properties. I anticipate multiple practical applications of this technique for metal oxide nanocrystals-based devices. Light-driven control over the plasmonic properties could be beneficial for sensing, signal enhancement, surface-enhanced infrared spectroscopy, and smart window technologies. Since depletion layers strongly affect the resistivity of MO-based films with detrimental effects, photodoping could be exploited as a post-fabrication, last-stage tool to improve device performances, enabling conductivity enhancements in thin films via the photo-tuning of depletion layers. A recently published work seems to confirm this effect.[129]

Lastly, the coupling between 2D TMDs and MO NCs enables the manipulation of the monolayers' properties, with possible implications for exciton funneling and quantum optics. Doped MO NCs (such as ITO NCs) can be utilized as light-driven injection charge sources. The optical scheme proposed in **Chapter VII** delivers a tool to locally investigate transport processes in 2D semiconductors and remotely manipulate their electronic structure. While in classical electrostatic devices the current is forced to flow between two electrodes, introducing averaging effects in transport measurements, by implementing MO NCs as active injection elements charge diffusion is observed with the lack of a pre-determined current path. As a perspective, I foresee a new all-optical technique to measure the local resistivity of conductive materials in real-time, without external perturbations nor averaging effects. This together displays the photodoping process of MO NCs enables horizons for innovative application spaces in light-powered optoelectronics and nanoelectronics. The progress achieved in these works marked milestones in the field of photodoping of MO nanocrystals and of the wireless manipulation of 2D materials. The reported 0D-2D heterostructure could become the fundamental working unit for the next-generation energy conversion and storage devices and currently my research group is working on the development of the first fully-operating MO-based photocapacitor.

Finally, I remark some open questions and delineate some aspects discussed in this dissertation that could benefit from future and more extended work. Regarding the dynamics of the photodoping process, the role of the surface states and ligands during charging has to be further investigated, and might provide useful insights on the fate of the photogenerated holes in solution environments. As reported in **Chapter II**, the kinetic equilibrium between recombination processes, such as Auger recombination, and the competing hole-capture processes is of fundamental importance for the accumulation of photogenerated carriers in the system. Further studies on the charge recombination dynamics (for example, with ultra-fast transient absorption measurements) could highlight new ways to hinder radiative and non-radiative recombination mechanisms, with semi-permanent effects in terms of amount of stored carriers in photodoped MO NCs. In hybrid 0D-2D systems, charge transfer and charge recombination could be either promoted or limited with the introduction of intermediate materials with different energy levels. In the case of the ITO-MoS_2 heterostructure (more details in **Chapter VII**), the stability of the charge separation process between the two materials is guaranteed by the energetic alignment, with the energy bending of the superficial layers of core-shell ITO-In_2O_3 NCs promoting hole transfer and preserving the extra electrons within the NC volume. Additionally, the long-range diffusion of photo-holes from the

injection spot in hybrid systems further limits carriers recombination and could be artificially targeted via dopants or strain engineering of the 2D layer.

Some of the effects reported in this work were limited by experimental conditions. Hence, superior results could be achieved under the right conditions, further proving the capability of these materials for energy-related applications. This was the case for multi-electron transfer reactions from photodoped ITO NCs to F4TCNQ molecules. It is reasonable to assume that oxidative molecules capable of accepting more than two electrons could unveil even larger multiple transfers. Furthermore, a replica of the photodoping experiment of the 0D-2D hybrid would benefit from the implementation of electrostatic gating. This would allow control over the initial charge populations of the 2D layers, proving that even greater variations in carrier density can be induced by light (since the drop in electron density was limited by the initial conditions) and testing the reversibility of the photodoping process in solid-state structures. Another aspect worth considering, in sight of future developments, is control over the bandgap energy of MO NCs. The most-studied MO NPs are transparent in the visible and absorb UV light. The practical implementation of the proposed would benefit by avoiding the ultraviolet radiation to promote electrons via photodoping. For example, for competitive solar conversion efficiency, the absorption of the active materials needs to be redshifted to the visible part of the spectrum. Alternative materials with a lower bandgap could be employed to achieve this goal, such as CuO (1.5 eV) or InN (1.2 eV) NCs. The capacitive properties of InN NCs have been recently reported,[245,246] and further investigations in this direction are encouraged. Other strategies to achieve this goal include the introduction of optically-active states within the bandgap and multi-photon absorption techniques, in order to photodope MO NCs with NIR radiation.[247] The additional participation of an active hole collector would contribute to the system's overall efficiency and might enable the further extension of the absorbed spectrum. Moreover, light-driven applications of MO NCs could be exploited in combination with existing technologies, providing additional features. For example, doped MO NCs could be incorporated in multi-layered third-generation photovoltaic cells. Furthermore, environmentally benign and non-toxic chemical elements are a key aspect to consider for all future technologies. Currently, the investigation of the photodoping dynamics was limited to a few metal oxide materials. Additional materials research is encouraged to fully exploit the richness of chemical synthesis techniques and expand the list of materials capable of photodoping to low-cost, environmentally friendly, and abundant light-driven materials.

IX. Conclusions

As shown in the previous chapter, the photodoping process of MO NCs is an extraordinarily effective tool to dynamically manipulate the electronic properties of nanomaterials and accumulate multiple charges in an entirely contactless manner, with potentially disruptive implications for innovative light-driven energy storage solutions. In this PhD thesis, I took a step towards understanding the photo-physical fundamentals of the light-driven charging process and I investigated the implementation of these photoactive nano-units in a combination of different environments and material configurations, contributing to the development of proof-of-concepts devices towards implementation. The main results achieved in this experimental work are summarized here.

Full control over the electronic structure of MO NCs was demonstrated both in the static case, by the tuning of the material's composition and structures (*e.g.*, core-shell, core-multishell architectures) at the synthesis stage, and in the dynamic case, with post-synthetic modulations induced by light (photodoping) or oxidative molecules (titration). These findings have been validated by a combination of experiments, theory, optical modeling, and numerical simulations. In particular, a specifically designed optical model was developed to describe the optical response of core-shell NCs upon photodoping, allowing to resolve their electronic structure and carrier density profiles at the nanoscale. In the static case, for Sn:In_2O_3-In_2O_3 core-shell NCs, the fine-tuning of the shell thickness is a powerful tool to engineer the depletion layer width (W) and modulate the band bending of the conduction band. The introduction of the shell material with distinctive energy and doping levels induces a double bending of the electronic bands, with the formation of three different regions of distinctive features in the electronic profile of the NC: an active core region characterized by the unperturbed carrier density, an active transition region with an order of magnitude lower carrier density, and a depletion region in which the metallic behavior is completely suppressed. Notably, the electronic band profile and the physical core-shell structure do not coincide. Due to the enhanced band bending, the growth of the undoped shell around the ITO core results in a significant increase in W (in the nanometric regime) and the possibility to induce step-like profiles in the CB, with the consequent formation of biplasmonic responses in the NIR spectrum. Depletion layer engineering is a powerful tool that provides a new degree of freedom for optimizing targeted optical and electrical features in MO NCs. Core-shell MO NCs with large depletion layers exhibit an enhanced sensitivity of LSPR modulations to external stimuli (*e.g.,* UV light) and, noteworthy, a significant increase in the capability of storing carriers.

In the dynamic case, modulations in the electronic structure can accurately describe the LSPR response of MO NCs and the accumulation of extra charges via photodoping. Specifically, the introduction of extra photocarriers leads to the light-driven band bending and the rearrangement of the electronic profile, with n_e increasing mainly in the shell regions. This work investigated the physics of the photodoping process, unveiling that depletion layer tuning and band bending are the primary mechanisms behind the photocharging of MO NCs. From these new insights, depletion layer engineering was exploited to enhance the charge storage capability of ITO NCs. A direct comparison between homogeneous and core-shell NCs confirmed the importance of depletion layer tuning for potential energetic applications of these materials. This model could be extended to other systems and nanostructures, further validating the proposed approach and enabling new features. For example, the light-driven dynamic formation of bi-plasmonic energy landscapes was observed in core-shell NCs. Control over the energetic band profiles and nanometric depletion layer open promising perspectives for the design of targeted optoelectronic properties in metal oxide nanostructures. I anticipate these studies to contribute to the optimization of the performances of MO NCs-based nanodevices.

Multiple charge transfer processes from photodoped MO NCs were proven via titration with F4TCNQ molecules. The photodoped electrons are able to ionize the F4TCNQ molecules with a transfer of two electrons, which highlights the capability of these highly reactive charges as efficient multi-electron photocatalysts. Electron counting procedures were developed successfully applied to core-shell ITO-In_2O_3 of various shell thicknesses, resulting in hundreds of electrons released from each photodoped nanocrystal, exhibiting competitive values for the next high-density battery generation. A number of photoelectrons extracted up to almost 400 was obtained in the NC with the larger shell, further supporting the depletion layer engineering model proposed for the optimization of the electronic structure of MO NCs. Furthermore, the technique developed in this work can be extended for the quantitative investigations of charging/discharging multi-electron processes in non-plasmonic NCs, being based only on the analysis of spectral signatures of F4TCNQ molecules in the UV-VIS region. Photodoping and oxidative reactions provide a non-invasive method to control the optoelectronic properties of MO NCs, without inducing degradations effects. The stability of MO NC involved in multi-charge reactions could be employed for multiple charging/discharging cycles in light-driven energy conversion/storage applications and for multi-electron photocatalysis.

Finally, the photodoping process of MO NCs was proven possible in all-solid-state configurations and ambient atmosphere conditions, thanks to the coupling between core-shell ITO NCs and single-layer

MoS_2. This 0D-2D hybrid heterostructure displays light-driven capacitive charging dynamics with capacitances values in the fF range. In this scheme, it was possible to store in the ITO layer and transfer to the 2D TMD more than 75 photocarriers per NC, reaching unprecedented charge-transfer capabilities. MO NCs can serve as efficient charge injection sources, inducing charge density variations in the 2D materials in the order of $\sim 1 \cdot 10^{13}$ cm^{-2} and proving photodoping as a competitive alternative to electrostatic doping. Remarkably, light-induced variations and long-range diffusion effects were detected at up to more than 40 μm of distance from the injection source. The charge transfer process and the long-range diffusion of carriers, driven by the relative energy alignment, is further suppressing charge recombination and the charge separation was proven to be stable up to more than 70 days, with no theoretical time limitations. The linear relation between the light-induced variations and the initial carrier density of the 1L-MoS_2 suggests that the photoinjected carriers tend to travel freely in the monolayer until recombination with naturally-present extra charges occurs. By triggering the photodoping process in a micrometer-sized excitation spot, it was possible to achieve intrinsic doping conditions ($\sim n_e < 2 \cdot 10^{12}$ cm^{-2}) in the 2D TMD in an area of more than 2200 μm^2. The all-optical scheme proposed allows the precise investigation of local inhomogeneities in unperturbed 2D TMDs semiconductors, with submicrometer precision, exposing the impact of strain and defects densities. Along this path, the ability to locally manipulate 2D semiconductors via p-type photodoping could lead to the design of novel nanoscale devices to target specific materials features. Further details on future proof of concept devices for energy storage and light-driven applications based on the photodoping process of MO NCs were reported in the previous chapter.

All the above findings add to the unique properties of metal oxide nanocrystals, further demonstrating this materials system as an extremely promising alternative to current optoelectronics devices and energy storage solutions. In summary, MO NCs combine record-high capacitance values and multi-transfer capabilities with the novel opportunity of photocharging. In addition to technological implementations, such as light-driven supercapacitors and self-powered nanoelectronics, the photodoping process of these emerging nanomaterials may also offer new research avenues in the fields of solid physics, materials chemistry and nanoscience. Fundamentally new approaches to solar energy conversion and storage can be conceived and experimented on these material-platforms. The research of the incoming years could demonstrate the integration of energy harvesting, conversion, accumulation, and release into a unique nanostructured device with high energy density features. Therefore, with the proper architecture and photocharging

scheme, doped metal oxide nanocrystals have the potential to contribute to the transition towards a sustainable future.

X. Appendix

X. 1 Appendix to Chapter III

Table 1 – Amounts of F4TCNQ titrants in terms of microliters and number of moles added to the photodoped ITO NCs solution. *Molar ratio percentage is defined as mol % = 100 × moles of F4TCNQ / (moles of F4TCNQ + moles of ITO NCs).* $n_{reacted}$ *is the number of F4TCNQ molecules that reacted with each ITO NC. Reproduced from Ref.*[25] *with permission from the Royal Society of Chemistry.*

	Moles of ITO NCs (n_{NC}) [10^{-9} mol]		
	0.08		
Added Volume of F4TCNQ [μL]	**Moles of F4TCNQ (n_{F4TCNQ}) [10^{-9} mol]**	mol %	$n_{reacted} = n_{F4TCNQ}/n_{NC}$
2	0.62	88.3	7.6
4	1.2	93.8	15.2
6	1.8	95.8	22.7
8	2.5	96.8	30.3
11	3.4	97.7	41.7
14	4.3	98.2	53.1
$Vmid = 15.5$	4.8	98.3	58.8
17	5.2	98.5	64.4
20	6.2	98.7	75.8
23	7.1	98.9	87.2
26	8.0	99	98.6
60	18	99.6	227.4
160	49	99.8	606.5

Parameters used in the numerical simulations

Table 2 – Parameters used in the simulations. *Table reproduced from Ref.[23] with permission from Springer Nature.*

e	ε	k_B	T	m_h	m_e	h
$1.602 \cdot 10^{-19}$ C	$8.854 \cdot 10^{-12}$ Fm^{-1}	$1.381 \cdot 10^{-23}$ JK^{-1}	293.15 K	$5.466 \cdot 10^{-31}$ kg	$3.644 \cdot 10^{-31}$ kg	$6.626 \cdot 10^{-34}$ Js

For the numerical simulations, the parameters introduced in Table 2 were used. In the case of homogeneous NCs, energy levels, the number of donor atoms, and relative dielectric permittivity are all constant. For core-shell systems, the radius-dependent non-equilibrium potentials profiles, donor distribution profile ($N_D = N_D(r)$) and relative dielectric profile ($\varepsilon(r)$) have to be defined according to the materials architecture. **Figure 35** reports the radius-dependent non-equilibrium potentials profiles and donor distribution profile employed to solve Poisson's equation for ITO-In_2O_3 core-shell NCs.[17] Different distributions and energy levels can be found for other metal oxides, such as ZnO and CdO.[248–250]

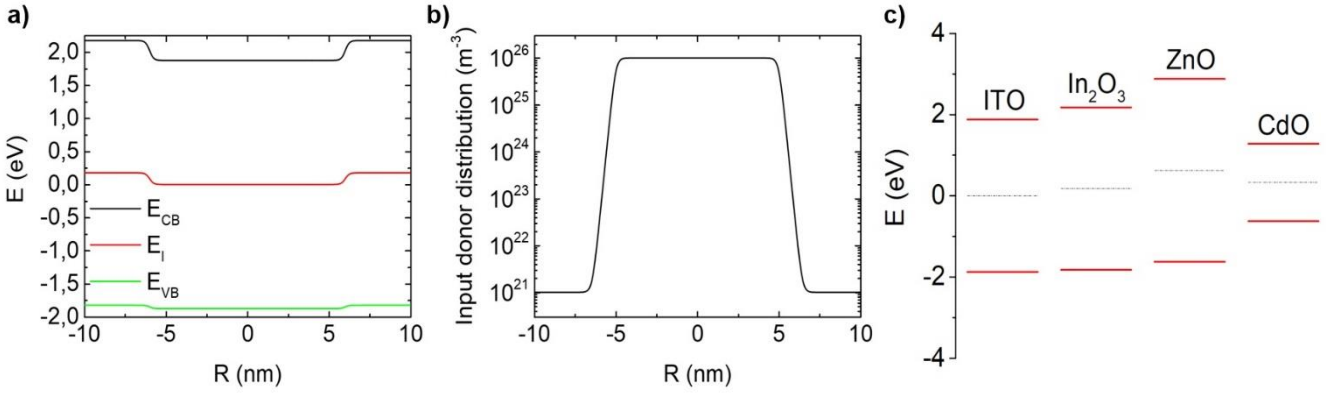

Figure 35 – Potential and donor distribution in ITO-In_2O_3 nanocrystal with 6 nm core and a 5 nm shell. a) *Input band diagram for a core-shell ITO- In_2O_3 structure. The system reference is the intrinsic level of the core material.* ***b)*** *Input donor distribution as a function of the nanocrystal radius.* ***c)*** *Relative conduction and valence band levels for ITO, In_2O_3, ZnO and CdO nanocrystals. The energy levels are referred as non-equilibrium states. Dashed lines represent the intrinsic level. Figure adapted from Ref.[23] with permission from Springer Nature.*

Table 4 - Extracted parameters for three-layer model fit for the as-synthetized samples. *Table reproduced from Ref.* [23] *with permission from Springer Nature.*

As-synthetized	C0	S1	S2	S3	S4	S5
$N_{e,core}$	703	911	912	916	914	937
$N_{e,shell}$	0	0	0	49	75	250
R_{core} (nm)	5.3	5.32	5.45	5.62	5.7	5.6
R_{active} (nm)	5.3	5.32	5.45	5.83	6.03	6.56
γ_c (cm^{-1})	$2.08 \cdot 10^3$	$1.62 \cdot 10^3$	$2.04 \cdot 10^3$	$1.88 \cdot 10^3$	$2.35 \cdot 10^3$	$1.66 \cdot 10^3$
γ_s (cm^{-1})	$10 \cdot 10^3$	$10 \cdot 10^3$	$10 \cdot 10^3$	$3.19 \cdot 10^3$	$3.62 \cdot 10^3$	$4.60 \cdot 10^3$
p	$3.40 \cdot 10^{-5}$	$5.68 \cdot 10^{-5}$	$7.87 \cdot 10^{-5}$	$11.98 \cdot 10^{-5}$	$11.73 \cdot 10^{-5}$	$11.71 \cdot 10^{-5}$
W (nm)	0.2	1.33	1.95	1.97	2.37	3.19

Table 3 – Extracted parameters for three-layer model fit for the photodoped samples*. Table reproduced from Ref.* [23] *with permission from Springer Nature.*

Photodoped	C0	S1	S2	S3	S4	S5
$N_{e,core}$	823	1136	1171	1177	1111	528
$N_{e,shell}$	0	0	0	99	327	1365
R_{core} (nm)	5.5	5.73	6.02	6.38	6.39	4.59
R_{active} (nm)	5.5	5.73	6.02	6.62	7.26	9.45
γ_c (cm^{-1})	$1.91 \cdot 10^3$	$1.53 \cdot 10^3$	$2.12 \cdot 10^3$	$2.01 \cdot 10^3$	$2.87 \cdot 10^3$	$1.36 \cdot 10^3$
γ_s (cm^{-1})	$10 \cdot 10^3$	$10 \cdot 10^3$	$1.97 \cdot 10^3$	$5.67 \cdot 10^3$	$2.60 \cdot 10^3$	$2.58 \cdot 10^3$
p	$3.4024 \cdot 10^{-5}$	$5.68 \cdot 10^{-5}$	$7.87 \cdot 10^{-5}$	$11.98 \cdot 10^{-5}$	$11.73 \cdot 10^{-5}$	$11.71 \cdot 10^{-5}$
W (nm)	0	0.92	1.38	1.18	1.14	0.3

X. 2 Appendix to Chapter V

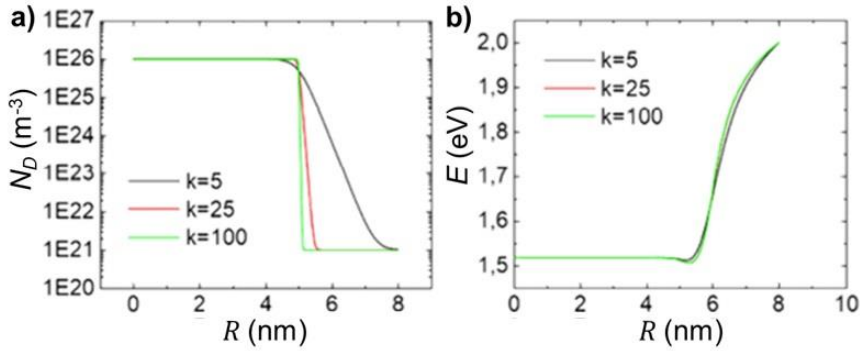

***Figure 36** – **Effects of dopants diffusion on the band profile numerically simulated. a**) The diffusion effects on the NCs are investigated by modifying the donor distribution profile $N_D(r)$ by using a sigmoid-like function: $N_D(r) = 10^{21} + [10^{26}/(1 + e^{k(r-Rcore)})]$. By varying the shape factor (k = 5, 25, 100), it is possible to induce a symmetric variation of the dopant distribution within the core-shell nanocrystal to simulate diffusion effects in three very different cases. The Poisson's equation was solved and the band diagram was analysed finding that the double bending of the conduction band is not significantly affected by moderate amounts of diffusion. **b**) The numerically calculated energy levels of an ITO-In_2O_3 core-shell NC with the donor profiles input as shown in panel a. Figure adapted from Ref.[23] with permission from Springer Nature.*

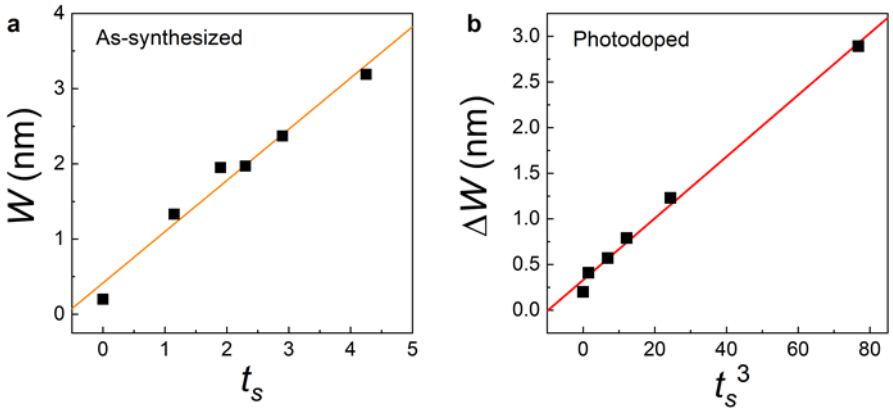

***Figure 37 - Depletion layer width and its modulation as a function of the shell thickness**. **a)** Depletion layer width as a function of the shell thickness t_s. A linear fit is reported in orange. **b)** The contraction of the depletion layer width (ΔW) in core-shell ITO-In_2O_3 NCs follows a t_s^3 law (linear fit showed in red), with t_s being the shell thickness. Figure adapted from Ref.[23] with permission from Springer Nature.*

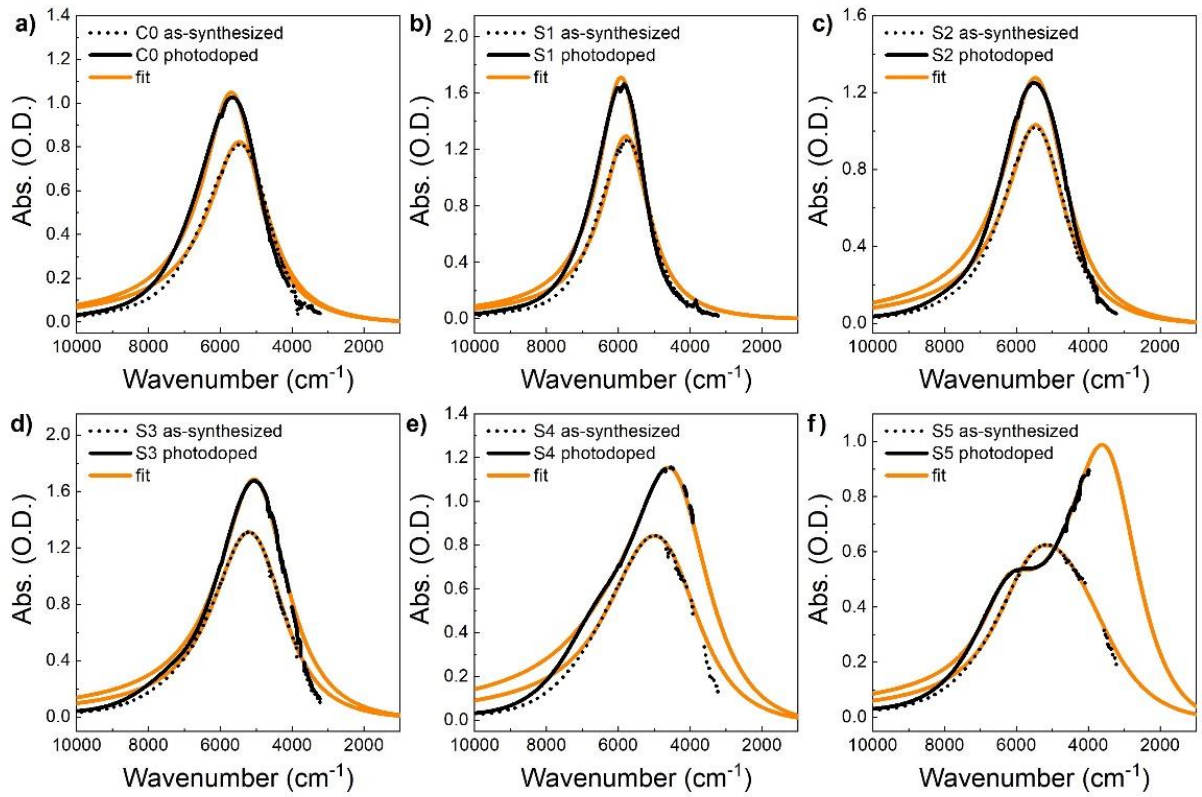

Figure 38 – Fitting of the absorbance spectra of samples C0-S5*. Spectra in the as-synthesized (dotted line) and photodoped (continue line) cases, with values of shell thickness from zero to 4.25 nm. The fitting of the experimental data using the multi -layer optical model is reported with the orange lines. Figure reproduced from Ref.*[23] *with permission from Springer Nature.*

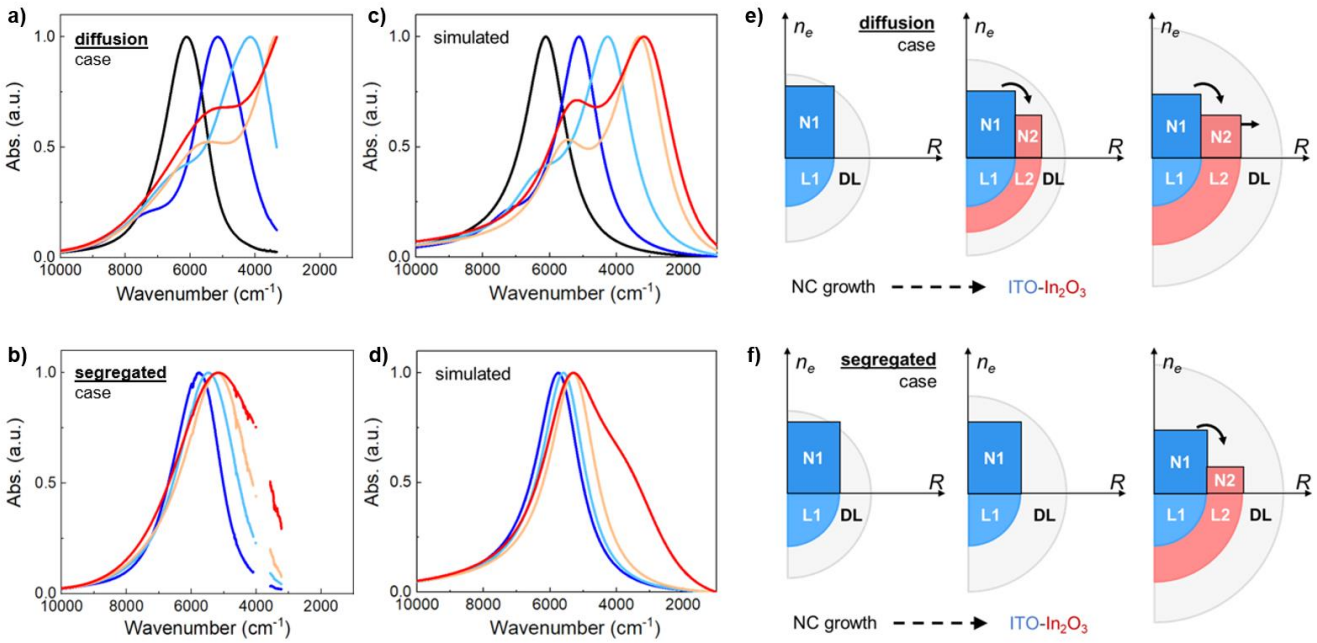

Figure 39 - Growth of core-doped-shell NCs and multi-layer model simulations. a) *Normalized absorption spectra of the two sets of samples (**a** and **b**), obtained employing two different synthesis techniques: subject to Sn-atoms diffusion and segregated particles. Respectively, the first set of ITO-In_2O_3 core-shell samples has a shell thickness going from 0 nm up to 4.95 nm (diameters: 10.1, 14.4, 16.1, 19.6, 20.0 nm), while the second set of samples is the already analyzed set C0-S5 with t_s up to 4.25 nm (diameters: 11, 13.3, 14.8, 15.6, 16.8, 19.5 nm). The plasmon peak position shifts to towards the red during the growth of the In_2O_3 layer.* ***c)*** *Simulated normalized absorption spectrum of ITO-In_2O_3 core-shell NCs, of growing shell thickness, for particles subject to donor diffusion (**c**) and for segregated particles (**d**). Scheme illustrating the procedure followed to replicate the experimentally observed trend. In the diffusion case (**d**), a spill-over of electrons from the core into the shell is simulated by the multi-layer model with the appearance of a second layer (L2), responsible for the second plasmonic mode and which then expands upon shell growth. In the segregated case (**e**), initially shell growth corresponds only to an increase of the depletion layer width, with the formation of a second layer (L2) occurring only in the latest stages and with low carrier density values (N2). In both cases, the total number of electrons was kept constant. Unpublished data from Ref.* [24].

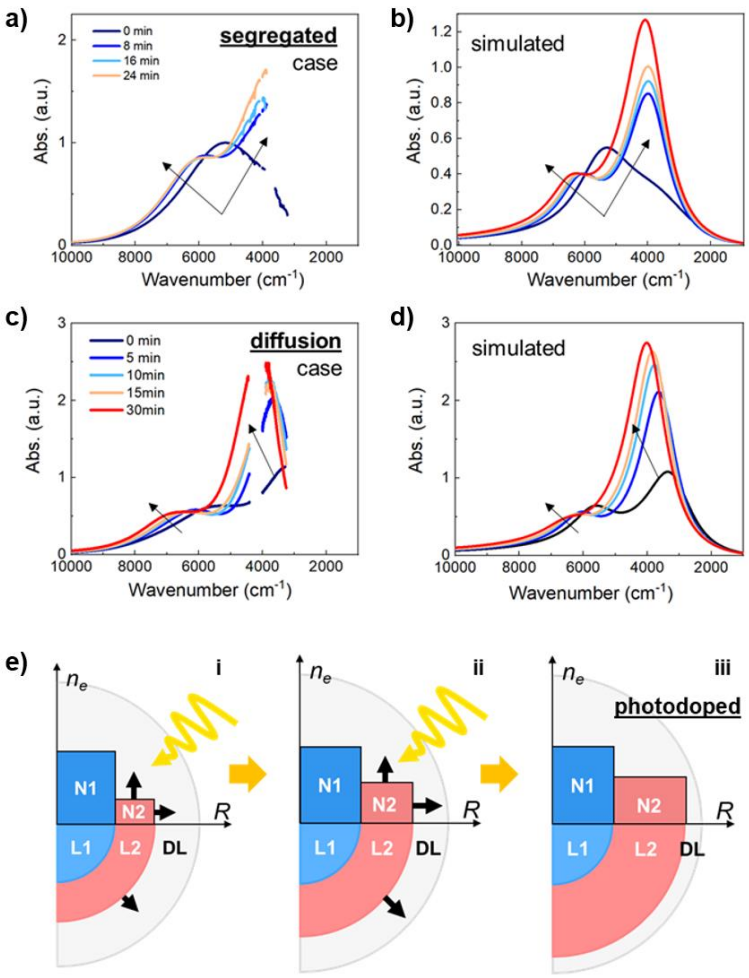

Figure 40 - Photodoping of ITO NCs simulated with multi-layer optical model. *Evolution of the absorption spectrum of ITO-In_2O_3 core-shell NCs under UV exposure for segregated particles (**a**) and particles subject to donor diffusion (**c**). The simulated spectra of the two samples (**b** and **d**) are obtained with the multi-layer optical model by expanding the second layer (L2) and slightly increasing its concentration (N2). The segregated NCs undergo a two-step process: initially photodoping causes plasmonic splitting by increasing the contribution of the second layer (from **e-i** to **e-ii**); after that, the addition of extra photoelectrons causes the peaks to blueshift and increase in intensity (from **e-ii** to **e-iii**), as for the diffusion case. Unpublished data from Ref.* [24].

X. 3 Appendix to Chapter VII

The photocapacitor model

The hybrid 0D-2D system can be modeled as an ideal capacitor composed of two oppositely charged layers (*i.e.,* the ITO NC layer and the 1L-MoS_2 layer) separated by an insulating region of thickness *d*. In this case, the dielectric layer is composed of the packed ligands and the depleted shell of the core-shell particle. By using a ligand shell thickness of ~0.8 nm (estimated from ligands of length ~1.5 nm)[251] and an In_2O_3 shell thickness of 1.25 nm, the total dielectric thickness is estimated as d =2.05 nm. An effective refractive index $\varepsilon_r \approx 2$ accounts for the dielectric materials and the intra-NC space. The capacitance (C) of the system is then $C = \varepsilon_r \varepsilon_0 \frac{A}{d}$ and the voltage difference as $\Delta V = \frac{Q}{C}$. By applying this model with the values of charge transferred a capacitance of ~6.8 fF is obtained for a single nanocrystal-1L-MoS_2 junction, corresponding to an areal capacitance of ~0.86 μF cm^{-2}. The calculated voltage potential is ~1.18 V, which is compatible with a potential difference of 1.27 eV between the ITO CB (*e.g.,* -4.6 eV, from Ref. [252]) and 1L-MoS_2 VB (*e.g.*, -5.87 eV, from Ref.[253]). The overall thickness of the hybrid nanocapacitor results to be approximately 12 nm, exhibiting a store energy density in the range of 1 μJ cm^{-2}. By considering the fast timescale of the charging process reported from kinetic investigations, power densities up to the nW cm^{-2} range were calculated.

Photo-charging kinetics

By analyzing the kinetics of the spectra and the shape of the photoluminescence peak it is possible to extract useful information on the physics of the photodoping and of the processes involved. The intensity of the photoluminescence variates over time in a non-trivial way which is yet to be fully unveiled. To further investigate photodoping dynamics of the hybrid structure beyond the temporal resolution of Ref.[17], the PL spectrum of 1L-MoS_2 was measured over the course of 10 minutes of photodoping with a step resolution of Δt ~ 0.3 seconds. As previously explained, the photoluminescence peak was fitted by two Lorentzian functions, taking into account the exciton and the trion contribution (in blue and green in **Figure 41**, respectively). The photodoping process of the hybrid system can be separated into two main phases: with a fast (A) and a slow (B) kinetics. The first phase takes place in the first 10 seconds of UV exposure (**Figure 41a-c)**. The spectral median of the PL quickly shifts to higher energies, the trion population decreases significantly, and simultaneously the intensity of the photoluminescence decreases.

The second phase (B) involves a slower process that takes place from 30 seconds to 10 minutes (**Figure 41d-f)**. The trion population remains virtually constant while the exciton contribution gets progressively enhanced. The intensity of the PL emission increases over time, recovering and exceeding the initial value. The increase in intensity can be explained by the greater quantum yield associated with the exciton emission (compared to the trions). The suppression of the trions is consistent with the thesis that photo-excited holes injected into the monolayer from the nanocrystals can annihilate the extra electron present in the 1L-MoS_2. Further experiments would be needed to better clarify the origin of the mechanisms involved and the dynamics of the photodoping in the heterostructure.

Figure 41g and **h** report the typical evolution of the spectral median and of exciton and trion contributions to the 1L-MoS2 PL spectrum as a function of the photodoping time of the hybrid system. The 0D-2D hybrid was being exposed to UV light (350 nm) continuously for more than 10 minutes. Remarkably, the trion peak is almost entirely suppressed via photodoping while initially being the predominant contribution. In addition to the steady-state analysis, the temporal response of the system can also be fit to a capacitor model, as shown in **Figure 41i**. Immediately after illumination, the temporal evolution of the charge density in the 1L-MoS_2 strongly resembles the transient response of a capacitor, which, in first approximation, can be fitted by: $Q = A_1 \cdot \left[1 - e^{-t/T_1}\right] = C\Delta V \cdot \left[1 - e^{-t/RC}\right]$. However, a similar fit deviates from the experimental data in the first minute of the charging kinetics. As a matter of fact, the initial charge transfer from the ITO nanocrystals to the 1L-MoS_2 accounts for more than half of the total carriers transferred in just 5 seconds. To overcome this, I introduce another term with a second time constant ($T_2 = R_2C_2$) in the capacitor-like dynamics:

$$\frac{n_{X-}(t)}{n_X(t)} \propto A_1 \left[1 - e^{-t/T_1}\right] + A_2 \left[1 - e^{-t/T_2}\right] \quad (26)$$

This second term is justified from the experimental observation of two distinct phases in the evolution of the PL spectrum, as described above. By implementing this new equation into the analysis, the fit can perfectly reproduce the evolution of the data. The second dynamics of the photodoping process exhibits a slower charging time constant RC^{-1} that is more than 8 times larger than the time constant T_1 extracted from the fit for the first phase. Given all the assumptions, this simple model confirms the hypothesis that the photodoping of the heterostructure evolves in two different phases with different timescales.

Electron counting in solid-state photodoping

Quantitative analysis of the number of electrons injected was performed considering the carrier density variations observed over the entire flake. The mass action model was applied only to the regions of the flake in which the SM change was larger than 10 meV, to avoid noise in the analysis. Hence, q^{tot} was obtained from the measured variations in n_e. To estimate the number of charges injected per NC (q^{NC}), the total amount of carrier transferred (q^{tot}) was normalized over the total number of NC excited with the UV laser (N^{excited}):

$$q^{NC} = \frac{q^{tot}}{N^{excited}} = \frac{q^{tot}}{\pi(d^{spot}/2)^2 \cdot \rho^{NC}}$$

Where d^{spot} = 5 μm is the diameter of the area illuminated by the laser spot (approximated with a circle) and ρ_{NC} is the density of the layer of ITO NCs in the hybrid. Due to inhomogeneities in the monolayer of NCs, ρ_{NC} was estimated from SEM images in three different areas of the hybrid characterized by a low, average, and high packing density of NCs. From these estimates, an upper value of q^{NC} = 100, a minimum value of q^{NC} = 50, and an average value of q^{NC} = 100 were obtained.[18]

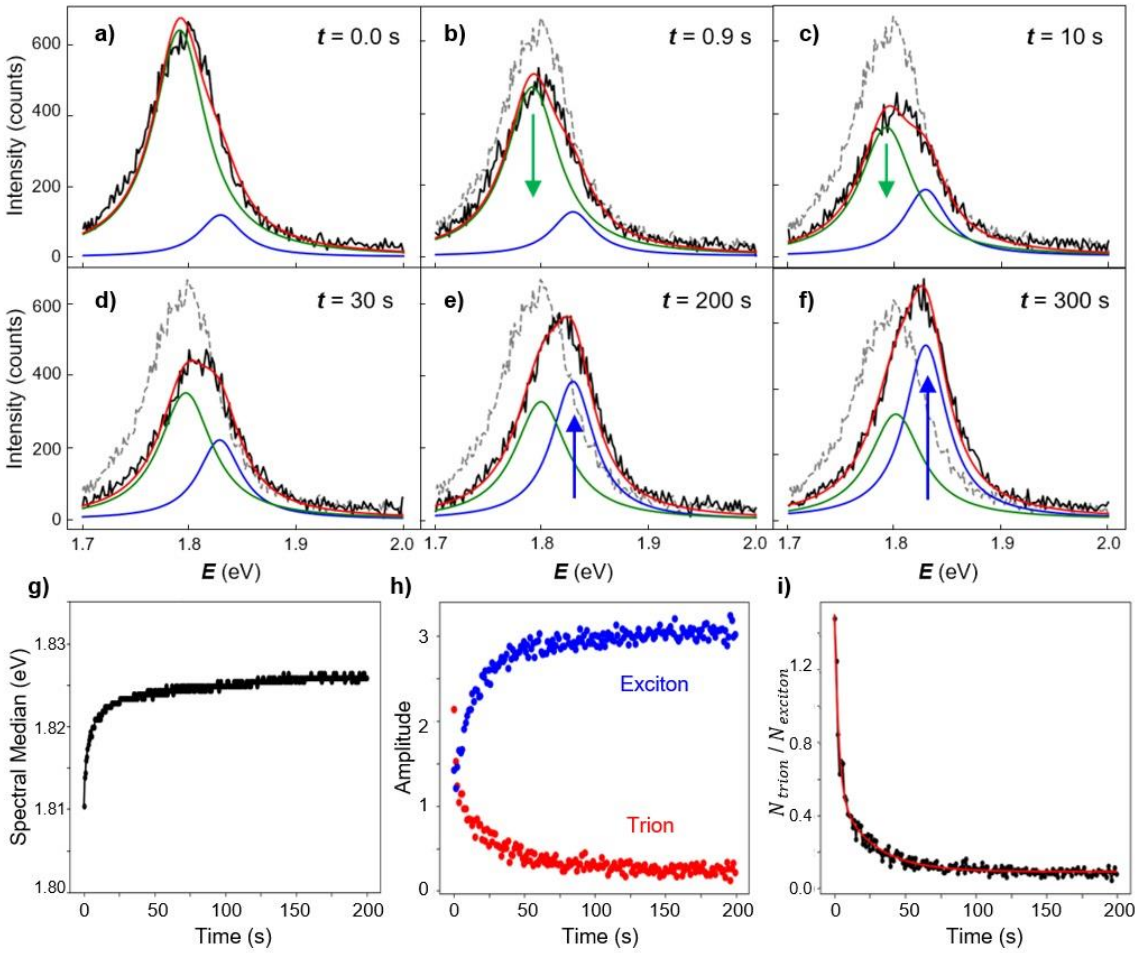

Figure 41 – Spectral evolution of the MoS2 photoluminescence over time during the photodoping. *The spectra were continuously collected with UV light (λex = 350 nm) every 0.3 seconds for 10 minutes. The grey dashed line reports the first spectrum acquired at t = 0 s, immediately after the exposure to UV light, as a comparison. The fits indicate the trion (green) and exciton (blue) contribution to the PL peak. It is possible to detect two processes separated in time involved in the blue-shift of the PL: in the first 10 seconds (from a to c) the trion population is suppressed together with the overall intensity; from 30 seconds to 600 seconds (from d to f) the exciton population increases as well as the intensity of the PL, recovering the initial magnitude at t = 350 s and increasing even more after.* ***g)*** *Typical spectral median of the MoS_2 photoluminescence as a function of time.* ***h)*** *Temporal evolution of the excitons (in blue) and trions (in red) during the photodoping.* ***i)*** *Evolution of the ratio between trions and excitons over time, proportional to the number of free carriers in the monolayer of MoS_2, fitted with a capacitor charging dynamics. By using two different time constants it is possible to reproduce faithfully the kinetics of the heterostructure, consistently with what previously hypothesized. Unpublished data.*

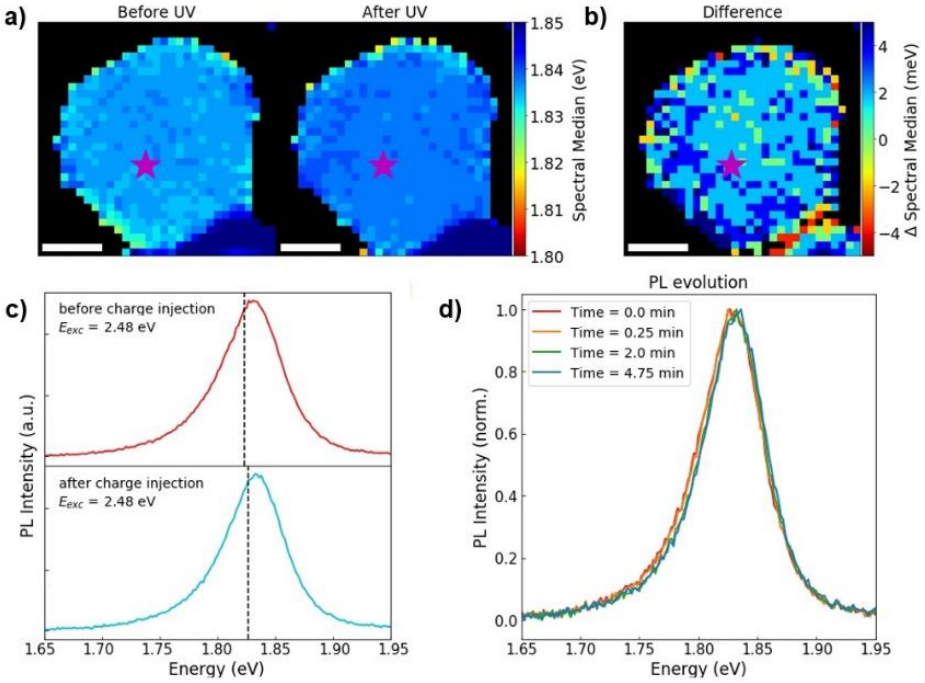

Figure 42 – Effects of UV exposure on 1L-MoS_2 emission. a) *Photodoping of a reference sample without ITO nanocrystals. Plot of the spectral median of the PL spectrum scanned over a single MoS_2 flake without ITO nanocrystals before and after exposure to UV light.* ***b)*** *No significant variations are observed as demonstrated by the difference map. The pink star illustrates the location at which the UV (350 nm) laser was focused (with a radius of circa 2.5 μm).* ***c)*** *Emission before (upper panel) and after (lower panel) the photodoping of the flake investigated in* ***Figure 30*** *collected directly at the UV excitation spot.* ***d)*** *Temporal evolution of the PL emission over a time scale of 5 minutes of UV exposure showing representative spectra. Strikingly, barely any changes are observed in the PL, indicating that most of the photo-injected charges diffuse from the excitation spot to farther regions of the hybrid system leaving almost unaffected the area directly illuminated with the laser. Figure reproduced from Ref.*[18] *with permission from John Wiley & Sons.*

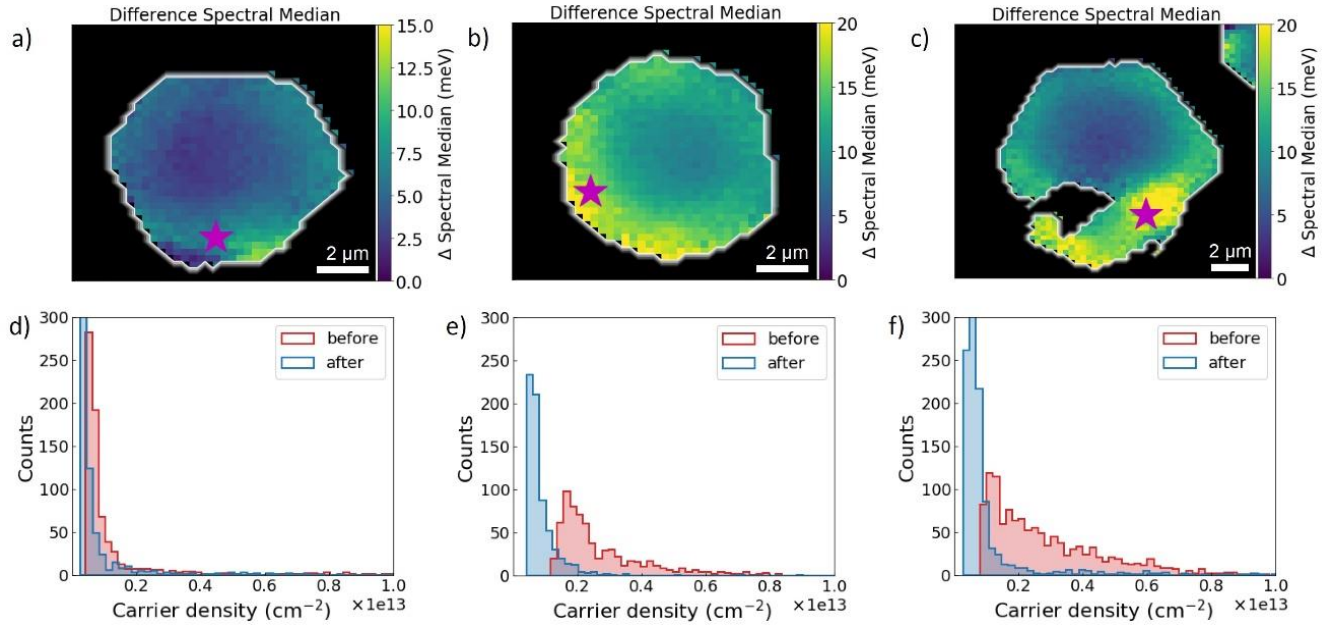

Figure 43 – Photodoping effects in various flakes with different excitation spots. *Variation of the spectral median of the PL due to the photodoping for three different flakes (a-c). The laser position is indicated by a purple star for each flake. d) Statistical summary of the carrier density distribution in the same three flakes (d-e) before (red) and after (blue) the injection of photo-charges. Photodoping effects depend on the initial carrier density distribution and occurs irrespectively from the injection location. Figure reproduced from Ref.*[18] *with permission from John Wiley & Sons.*

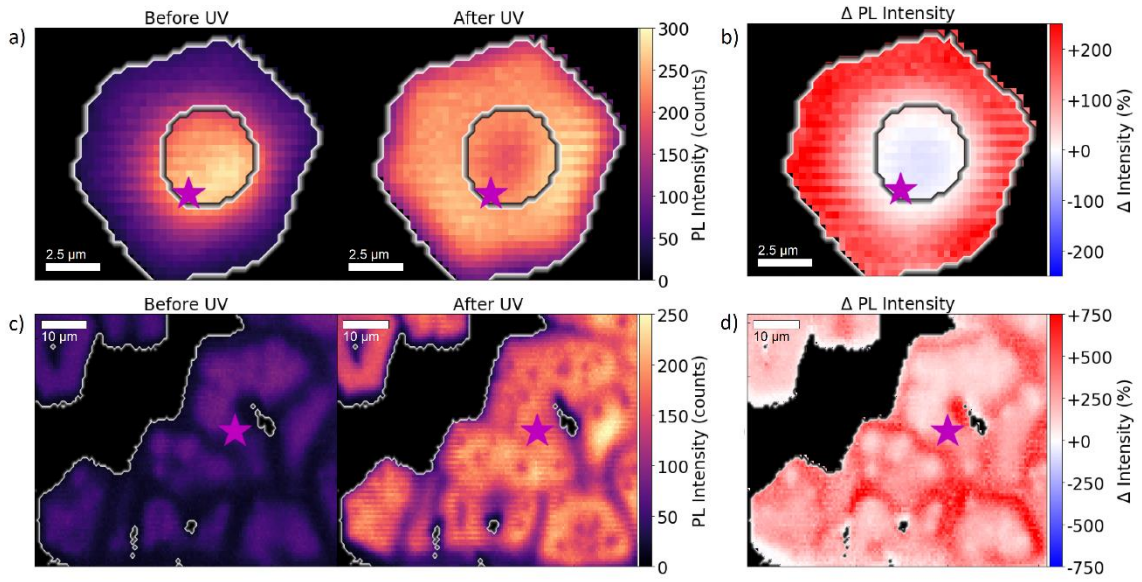

Figure 44 – Photo-induced variations in the photoluminescence intensity. a) *PL intensity before and after the photodoping of the Flake reported in* ***Figure 30*** *and* ***b)*** *illustration of intensity increase (in percentage) normalized with respect to the initial intensity. Δ Intensity (%) = 100×(I^{after} - I^{before})/I^{before}.* ***c)*** *PL intensity before and after the photodoping of the area reported in* ***Figure 32*** *and* ***d)*** *illustration of the normalized intensity increase Δ Intensity (%). While the overall PL intensity tend to increase almost everywhere in term of absolute counts, the biggest variations in intensity percentage are localized in the areas that initially present a high concentration of trions. This is consistent with what is expected as the PL emission generated from the recombination of excitons is brighter than the same trion-based process, and it is another indicator that the formation of trions is hindered and the formation of excitons is enhanced increasing the overall photoluminescence efficiency of the 1L-MoS_2. Figure reproduced from Ref.*[18] *with permission from John Wiley & Sons.*

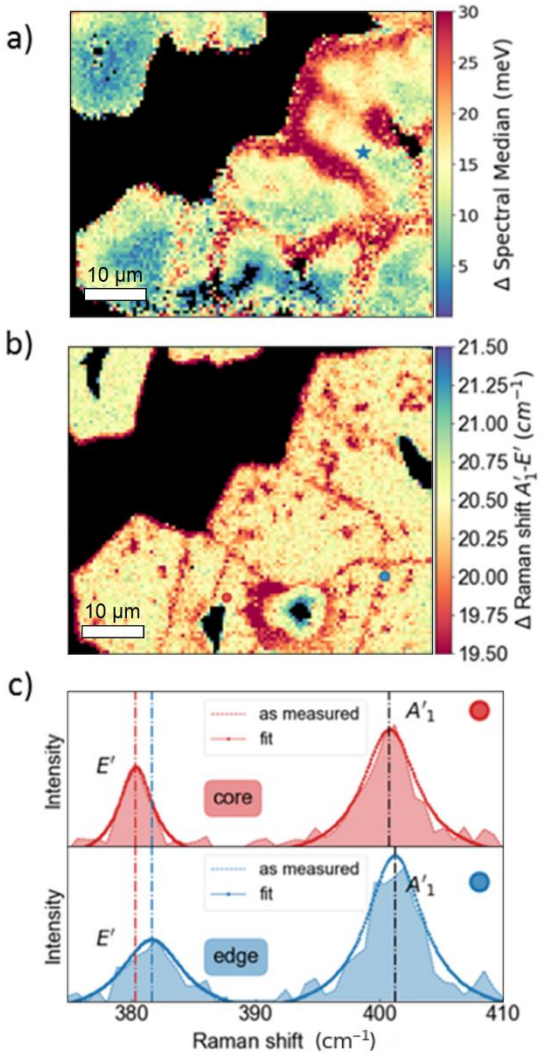

Figure 45 – Raman measurements illustrating relaxed strain along grain boundaries. *A measure of strain in monolayer MoS_2 is the Raman shift of the E' and A_1'. Lower Δ Raman shifts of E' and A_1' indicate relaxed tensile strain. In fact, in our Raman map of the same area of investigation grain boundaries of the individual MoS_2 flakes are highlighted by lower Δ Raman shifts, i.e. relaxed tensile strain, and coincide with the largest photo-induced electron extraction.* ***a)*** *The difference map of the spectral median of a larger area of MoS_2 flakes illustrating variations of the spectral median of the PL of more than 30 meV. Photodoping was induced at the blue colored star in a diffraction limited spot.* ***b)*** *Δ Raman map of the difference of A_1' and E' modes showing lowest Δ Raman shift along the grain boundaries, correlated to regions with decreased strain.* ***c)*** *Example of two Raman spectra in the core (red) and edge (blue) region, illustrating that only the E' mode is affected by strain. Figure reproduced from Ref.*[18] *with permission from John Wiley & Sons.*

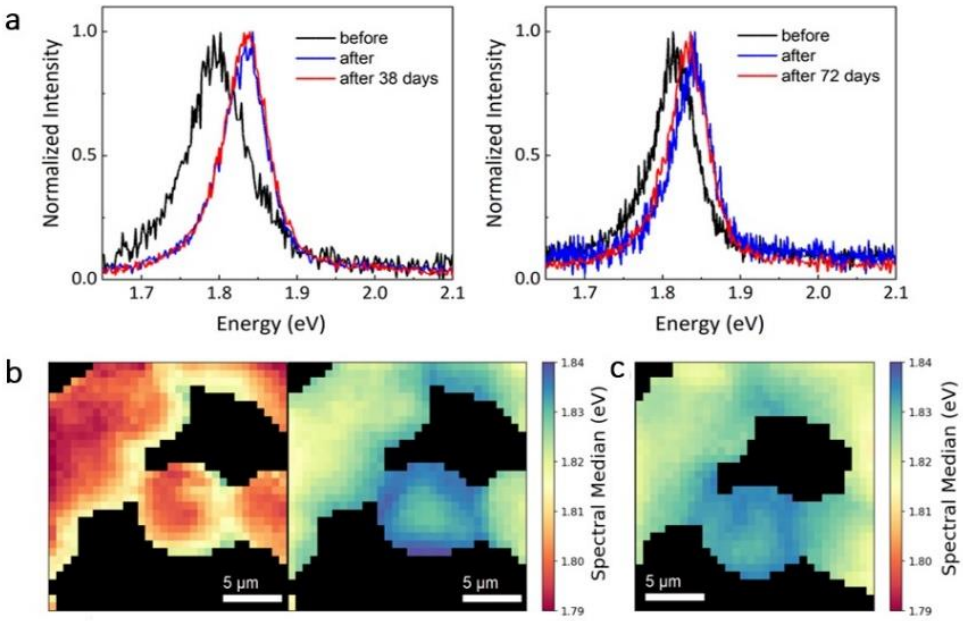

Figure 46 – Long-term stability of the photodoping effect. *The photoluminescence spectrum of the monolayer MoS_2 before photodoping (black curves), directly after photodoping (blue curves), (**a**) 38 days later (red curve), and (**b**) 72 days (red curve). Care was taken to measure the same region of the monolayer MoS_2 and the results in (a) and (b) are on independent samples illustrating the robustness of the effect. For both samples, the photoluminescence peak position and line shape are altered significantly during the initial photodoping process as a result of the injection of holes from the ITO nanocrystals to the monolayer MoS_2 (from black to blue curves). These changes persist near perfectly after measuring again the same spot after several days, indicating that the charge transfer after photodoping is permanent on the timescales of months. **c)** Spectral median map of a portion of the MoS2/ITO hybrid before (left) and after (right) the photodoping. **d**) Spectral map of the same area of the system collected 38 days later. The photo-induced effects of few minutes of UV exposure are still clearly visible in the hybrid, proving that the transfer of photo-holes is permanent and stable on a timescale of months. Figure adapted from Ref.*[17] *with permission from American Chemical Society and from Ref.*[18] *with permission from John Wiley & Sons.*

XI. Bibliography

1. International Panel on Climate Change [IPCC]. Reports — IPCC. (2007).

2. Kerr, R. A. Global warming is changing the world. *Science (80-.).* **316**, 188–190 (2007).

3. OECD/IEA. IEA (International Energy Agency). *Renewable Information 2011* (2011).

4. Karneyeva, Y. & Wüstenhagen, R. Solar feed-in tariffs in a post-grid parity world: The role of risk, investor diversity and business models. *Energy Policy* **106**, 445–456 (2017).

5. Obama, B. The irreversible momentum of clean energy. *Science (80-.).* **355**, 126–129 (2017).

6. Sugiyama, M. Climate change mitigation and electrification. *Energy Policy* **44**, 464–468 (2012).

7. Koomey, J. G., Scott Matthews, H. & Williams, E. Smart Everything: Will Intelligent Systems Reduce Resource Use? *Annu. Rev. Environ. Resour.* **38**, 311–343 (2013).

8. Ludig, S., Haller, M., Schmid, E. & Bauer, N. Fluctuating renewables in a long-term climate change mitigation strategy. *Energy* **36**, 6674–6685 (2011).

9. Zeng, Q. *et al.* Integrated Photorechargeable Energy Storage System: Next-Generation Power Source Driving the Future. *Adv. Energy Mater.* **10**, 1–30 (2020).

10. Kyerematen, N. A., Brousse, T. & Pech, D. Microsupercapacitors as miniaturized energy-storage components for on-chip electronics. *Nat. Nanotechnol.* **12**, 7–15 (2017).

11. Winter, M. & Brodd, R. J. What are batteries, fuel cells, and supercapacitors? *Chem. Rev.* **104**, 4245–4269 (2004).

12. Musolino, V. & Tironi, E. A comparison of supercapacitor and high-power lithium batteries. *Int. Conf. Electr. Syst. Aircraft, Railw. Sh. Propulsion, ESARS 2010* (2010) doi:10.1109/ESARS.2010.5665263.

13. Poonam, Sharma, K., Arora, A. & Tripathi, S. K. Review of supercapacitors: Materials and devices. *J. Energy Storage* **21**, 801–825 (2019).

14. Brozek, C. K. *et al.* Soluble Supercapacitors: Large and Reversible Charge Storage in Colloidal Iron-Doped ZnO Nanocrystals. *Nano Lett.* **18**, 3297–3302 (2018).

15. Ghini, M. *et al.* Photodoping of metal oxide nanocrystals for multi-charge accumulation and light-driven energy storage. *Nanoscale* **13**, 8773–8783 (2021).

16. Schimpf, A. M., Lounis, S. D., Runnerstrom, E. L., Milliron, D. J. & Gamelin, D. R. Redox chemistries and plasmon energies of photodoped In2O3 and Sn-Doped In2O3 (ITO) nanocrystals. *J. Am. Chem. Soc.* **137**, 518–524 (2015).

17. Kriegel, I. *et al.* Light-Driven Permanent Charge Separation across a Hybrid Zero-Dimensional/Two-Dimensional Interface. *J. Phys. Chem. C* **124**, 8000–8007 (2020).

18. Ghini, M. *et al.* 0D Nanocrystals as Light-Driven, Localized Charge-Injection Sources for the Contactless Manipulation of Atomically Thin 2D Materials. *Adv. Photonics Res.* **2**, 2000151 (2021).

19. Huang, Y. *et al.* Multifunctional Energy Storage and Conversion Devices. *Adv. Mater.* **28**, 8344–8364 (2016).

20. Zandi, O. *et al.* Impacts of surface depletion on the plasmonic properties of doped semiconductor nanocrystals. *Nat. Mater.* **17**, 710–717 (2017).

21. Gibbs, S. L., Staller, C. M. & Milliron, D. J. Surface Depletion Layers in Plasmonic Metal Oxide Nanocrystals. *Acc. Chem. Res.* **52**, 2516–2524 (2019).

22. Staller, C. M. *et al.* Tuning Nanocrystal Surface Depletion by Controlling Dopant Distribution as a Route Toward Enhanced Film Conductivity. *Nano Lett.* **18**, 2870–2878 (2018).

23. Ghini, M. *et al.* Control of electronic band profiles through depletion layer engineering in core–shell nanocrystals. *Nat. Commun.* **13**, 537 (2022).

24. Ghini, M. *et al.* Multi-Modal Plasmonic Dynamic Splitting in Doped Metal Oxide Nanocrystals. *Prep.*

25. Ghini, M., Camellini, A., Rubino, A. & Kriegel, I. Multi-charge Transfer from Photodoped ITO Nanocrystals. *Nanoscale Adv.* (2021) doi:10.1039/D1NA00656H.

26. Manzeli, S., Ovchinnikov, D., Pasquier, D., Yazyev, O. V & Kis, A. {2D} transition metal dichalcogenides. *Nat. Rev. Mater.* **2**, 17033 (2017).

27. Prakash Sharma, V., Sharma, U., Chattopadhyay, M. & Shukla, V. N. Advance Applications of Nanomaterials: A Review. *Mater. Today Proc.* **5**, 6376–6380 (2018).

28. Kolahalam, L. A. *et al.* Review on nanomaterials: Synthesis and applications. *Mater. Today Proc.* **18**, 2182–2190 (2019).

29. Zheng, W. *et al.* Light Emission Properties of 2D Transition Metal Dichalcogenides: Fundamentals and Applications. *Adv. Opt. Mater.* **6**, 1–29 (2018).

30. Gambetta, J. M., Chow, J. M. & Steffen, M. Building logical qubits in a superconducting quantum computing system. *npj Quantum Inf.* **3**, 0–1 (2017).

31. Vandersypen, L. M. K. *et al.* Interfacing spin qubits in quantum dots and donors—hot, dense, and coherent. *npj Quantum Inf.* **3**, 1–10 (2017).

32. Vandersypen, L. M. K. & Eriksson, M. A. Quantum computing with semiconductor spins. *Phys. Today* **72**, 38–45 (2019).

33. Sharma, N., Ojha, H., Bharadwaj, A., Pathak, D. P. & Sharma, R. K. Preparation and catalytic applications of nanomaterials: a review. *RSC Adv.* **5**, 53381–53403 (2015).

34. Dante, S. *et al.* Selective Targeting of Neurons with Inorganic Nanoparticles: Revealing the Crucial Role of Nanoparticle Surface Charge. *ACS Nano* **11**, 6630–6640 (2017).

35. Figuerola, A., Di, R., Manna, L. & Pellegrino, T. From iron oxide nanoparticles towards advanced iron-based inorganic materials designed for biomedical applications. *Pharmacol. Res.* **62**, 126–143 (2010).

36. Razzaque, S., Hussain, S. Z., Hussain, I. & Tan, B. Design and utility of metal/metal oxide nanoparticles mediated by thioether end-functionalized polymeric ligands. *Polymers* vol. 8 (2016).

37. Han, J. *et al.* Polymer-Based Nanomaterials and Applications for Vaccines and Drugs. *Polymers (Basel).* **10**, (2018).

38. Paranjpe, M. & Müller-Goymann, C. C. Nanoparticle-Mediated Pulmonary Drug Delivery: A Review. *Int. J. Mol. Sci.* **15**, 5852–5873 (2014).

39. Mirza, A. Z. & Siddiqui, F. A. Nanomedicine and drug delivery: a mini review. *Int. Nano Lett.* **4**, (2014).

40. Maçaira, J., Andrade, L. & Mendes, A. Review on nanostructured photoelectrodes for next generation dye-sensitized solar cells. *Renew. Sustain. Energy Rev.* **27**, 334–349 (2013).

41. Pomerantseva, E., Bonaccorso, F., Feng, X., Cui, Y. & Gogotsi, Y. Energy storage: The future enabled by nanomaterials. *Science (80-.).* **366**, eaan8285 (2019).

42. Bonaccorso, F. *et al.* 2D materials. Graphene, related two-dimensional crystals, and hybrid systems for energy conversion and storage. *Science (80-.).* **347**, 1246501 (2015).

43. Su, X. *et al.* Silicon-Based Nanomaterials for Lithium-Ion Batteries: A Review. *Adv. Energy Mater.* **4**, 1300882 (2014).

44. Gatti, T. *et al.* Opportunities from Doping of Non-Critical Metal Oxides in Last Generation Light-Conversion Devices. *Adv. Energy Mater.* **11**, 2101041 (2021).

45. Klein, A. Transparent Conducting Oxides: Electronic Structure–Property Relationship from Photoelectron Spectroscopy with in situ Sample Preparation. *J. Am. Ceram. Soc.* **96**, 331–345 (2013).

46. Maduraiveeran, G., Sasidharan, M. & Jin, W. Earth-abundant transition metal and metal oxide nanomaterials: Synthesis and electrochemical applications. *Prog. Mater. Sci.* **106**, 100574 (2019).

47. Chen, Z. *et al.* Fabrication of highly transparent and conductive indium-tin oxide thin films with a high figure of merit via solution processing. *Langmuir* **29**, 13836–13842 (2013).

48. Afre, R. A., Sharma, N., Sharon, M. & Sharon, M. Transparent Conducting Oxide Films for Various Applications: A Review. *Rev. Adv. Mater. Sci.* **53**, 79–89 (2018).

49. Edwards, P. P., Porch, A., Jones, M. O., Morgan, D. V & Perks, R. M. Basic materials physics of transparent conducting oxides. *Dalt. Trans.* 2995–3002 (2004) doi:10.1039/B408864F.

50. Tandon, B., Ashok, A. & Nag, A. Colloidal transparent conducting oxide nanocrystals: A new infrared plasmonic material. *Pramana - J. Phys.* **84**, 1087–1098 (2015).

51. Minami, T. Transparent conducting oxide semiconductors for transparent electrodes. *Semicond. Sci. Technol.* **20**, (2005).

52. Yu, X., Marks, T. J. & Facchetti, A. Metal oxides for optoelectronic applications. *Nat. Mater.* **15**, 383–396 (2016).

53. De Trizio, L. *et al.* Nb-doped colloidal TiO2 nanocrystals with tunable infrared absorption. *Chem. Mater.* **25**, 3383–3390 (2013).

54. Jansons, A. W., Plummer, L. K. & Hutchison, J. E. Living Nanocrystals. *Chem. Mater.* **29**, 5415–5425 (2017).

55. Jansons, A. W. & Hutchison, J. E. Continuous Growth of Metal Oxide Nanocrystals: Enhanced Control of Nanocrystal Size and Radial Dopant Distribution. *ACS Nano* **10**, 6942–6951 (2016).

56. Lounis, S. D., Runnerstrom, E. L., Llordés, A. & Milliron, D. J. Defect chemistry and Plasmon physics of colloidal metal oxide Nanocrystals. *J. Phys. Chem. Lett.* **5**, 1564–1574 (2014).

57. Kriegel, I., Scotognella, F. & Manna, L. Plasmonic doped semiconductor nanocrystals: Properties, fabrication, applications and perspectives. *Phys. Rep.* **674**, 1–52 (2017).

58. Crockett, B. M., Jansons, A. W., Koskela, K. M., Johnson, D. W. & Hutchison, J. E. Radial Dopant Placement for Tuning Plasmonic Properties in Metal Oxide Nanocrystals. *ACS Nano* **11**, 7719–7728 (2017).

59. Liu, J. *et al.* Recent advances of plasmonic nanoparticles and their applications. *Materials (Basel).* **11**, (2018).

60. Abb, M., Wang, Y., Papasimakis, N., de Groot, C. H. & Muskens, O. L. Surface-enhanced infrared spectroscopy using metal oxide plasmonic antenna arrays. *Nano Lett.* **14**, 346–352 (2014).

61. Wang, Y., Runnerstrom, E. L. & Milliron, D. J. Switchable Materials for Smart Windows. *Annu. Rev. Chem. Biomol. Eng.* **7**, 283–304 (2016).

62. Agrawal, A., Kriegel, I. & Milliron, D. J. Shape-dependent field enhancement and plasmon resonance of oxide nanocrystals. *J. Phys. Chem. C* **119**, 6227–6238 (2015).

63. Blemker, M. A., Gibbs, S. L., Raulerson, E. K., Milliron, D. J. & Roberts, S. T. Modulation of the Visible Absorption and Reflection Profiles of ITO Nanocrystal Thin Films by Plasmon

Excitation. *ACS Photonics* **7**, 1188–1196 (2020).

64. Tandon, B., Ghosh, S. & Milliron, D. J. Dopant Selection Strategy for High-Quality Factor Localized Surface Plasmon Resonance from Doped Metal Oxide Nanocrystals. *Chem. Mater.* **31**, 7752–7760 (2019).

65. Matsui, H., Furuta, S. & Tabata, H. Role of electron carriers on local surface plasmon resonances in doped oxide semiconductor nanocrystals. *Appl. Phys. Lett.* **104**, 211903 (2014).

66. Runnerstrom, E. L. *et al.* Defect Engineering in Plasmonic Metal Oxide Nanocrystals. *Nano Lett.* **16**, 3390–3398 (2016).

67. Dahlman, C. J., Tan, Y., Marcus, M. A. & Milliron, D. J. Spectroelectrochemical Signatures of Capacitive Charging and Ion Insertion in Doped Anatase Titania Nanocrystals. *J. Am. Chem. Soc.* **137**, 9160–9166 (2015).

68. Giannuzzi, R. *et al.* Pseudocapacitive behaviour in sol-gel derived electrochromic titania nanostructures. *Nanotechnology* **32**, (2021).

69. Agrawal, A. *et al.* Rationalizing the Impact of Surface Depletion on Electrochemical Modulation of Plasmon Resonance Absorption in Metal Oxide Nanocrystals. *ACS Photonics* **5**, 2044–2050 (2018).

70. Stankic, S., Suman, S., Haque, F. & Vidic, J. Pure and multi metal oxide nanoparticles: synthesis, antibacterial and cytotoxic properties. *J. Nanobiotechnology* **14**, 73 (2016).

71. Niederberger, M. Nonaqueous Sol–Gel Routes to Metal Oxide Nanoparticles. *Acc. Chem. Res.* **40**, 793–800 (2007).

72. Niederberger, M., Garnweitner, G., Pinna, N. & Neri, G. Non-aqueous routes to crystalline metal oxide nanoparticles: Formation mechanisms and applications. *Prog. Solid State Chem.* **33**, 59–70 (2005).

73. Ito, D., Yokoyama, S., Zaikova, T., Masuko, K. & Hutchison, J. E. Synthesis of Ligand-Stabilized Metal Oxide Nanocrystals and Epitaxial Core/Shell Nanocrystals via a Lower-Temperature Esterification Process. *ACS Nano* **8**, 64–75 (2014).

74. Mattox, T. M., Bergerud, A., Agrawal, A. & Milliron, D. J. Influence of Shape on the Surface Plasmon Resonance of Tungsten Bronze Nanocrystals. *Chem. Mater.* **26**, 1779–1784 (2014).

75. Yang, C., Chen, J.-F., Zeng, X., Cheng, D. & Cao, D. Design of the Alkali-Metal-Doped WO3 as a Near-Infrared Shielding Material for Smart Window. *Ind. \& Eng. Chem. Res.* **53**, 17981–17988 (2014).

76. Lounis, S. D., Runnerstrom, E. L., Bergerud, A., Nordlund, D. & Milliron, D. J. Influence of dopant distribution on the plasmonic properties of indium tin oxide nanocrystals. *J. Am. Chem. Soc.* **136**, 7110–7116 (2014).

77. Maho, A. *et al.* Aqueous Processing and Spray Deposition of Polymer-Wrapped Tin-Doped

Indium Oxide Nanocrystals as Electrochromic Thin Films. *Chem. Mater.* **32**, 8401–8411 (2020).

78. Schimpf, A. M., Gunthardt, C. E., Rinehart, J. D., Mayer, J. M. & Gamelin, D. R. Controlling carrier densities in photochemically reduced colloidal ZnO nanocrystals: Size dependence and role of the hole quencher. *J. Am. Chem. Soc.* **135**, 16569–16577 (2013).

79. Araujo, J. J. *et al.* Tunable Band-Edge Potentials and Charge Storage in Colloidal Tin-Doped Indium Oxide (ITO) Nanocrystals. *ACS Nano* acsnano.1c04660 (2021) doi:10.1021/acsnano.1c04660.

80. Tandon, B., Agrawal, A., Heo, S. & Milliron, D. J. Competition between Depletion Effects and Coupling in the Plasmon Modulation of Doped Metal Oxide Nanocrystals. *Nano Lett.* **19**, 2012–2019 (2019).

81. Yang, H., Garfunkel, E. L. & Batson, P. E. Probing free carrier plasmons in doped semiconductors using spatially resolved electron energy loss spectroscopy. *Phys. Rev. B* **102**, 205427 (2020).

82. Benton, B. T., Greenberg, B. L., Aydil, E., Kortshagen, U. R. & Campbell, S. A. Variable range hopping conduction in ZnO nanocrystal thin films. *Nanotechnology* **29**, 415202 (2018).

83. Staller, C. M., Gibbs, S. L., Saez Cabezas, C. A. & Milliron, D. J. Quantitative Analysis of Extinction Coefficients of Tin-Doped Indium Oxide Nanocrystal Ensembles. *Nano Lett.* **19**, 8149–8154 (2019).

84. Seiwatz, R. & Green, M. Space Charge Calculations for Semiconductors. *J. Appl. Phys.* **29**, 1034–1040 (1958).

85. Mie, G. Beiträge zur Optik trüber Medien, speziell kolloidaler Metallösungen. *Ann. Phys.* **330**, 377–445 (1908).

86. Bohren, C. F. & Huffman, D. R. *Absorption and scattering of light by small particles*. *Absorption and Scattering of Light by Small Particles* (Wiley-VCH, 2004). doi:10.1002/9783527618156.

87. Myroshnychenko, V. *et al.* Modelling the optical response of gold nanoparticles. *Chem. Soc. Rev.* **37**, 1792–1805 (2008).

88. Perner, M. *et al.* Optically Induced Damping of the Surface Plasmon Resonance in Gold Colloids. *Phys. Rev. Lett.* **78**, 2192–2195 (1997).

89. Hu, M. *et al.* Dark-field microscopy studies of single metal nanoparticles: understanding the factors that influence the linewidth of the localized surface plasmon resonance. *J. Mater. Chem.* **18**, 1949–1960 (2008).

90. Colas des Francs, G., Derom, S., Vincent, R., Bouhelier, A. & Dereux, A. Mie Plasmons: Modes Volumes, Quality Factors, and Coupling Strengths (Purcell Factor) to a Dipolar Emitter. *Int. J. Opt.* **2012**, 175162 (2012).

91. Mergel, D. & Qiao, Z. Dielectric modelling of optical spectra of thin In 2 O 3 : Sn films. *J. Phys. D. Appl. Phys.* **35**, 794–801 (2002).

92. Agrawal, A., Johns, R. W. & Milliron, D. J. Control of Localized Surface Plasmon Resonances in Metal Oxide Nanocrystals. *Annu. Rev. Mater. Res.* **47**, 1–31 (2017).

93. Schimpf, A. M., Thakkar, N., Gunthardt, C. E., Masiello, D. J. & Gamelin, D. R. Charge-tunable quantum plasmons in colloidal semiconductor nanocrystals. *ACS Nano* **8**, 1065–1072 (2014).

94. Geng, D. & Yang, H. Y. Recent Advances in Growth of Novel 2D Materials: Beyond Graphene and Transition Metal Dichalcogenides. *Adv. Mater.* **30**, 1800865 (2018).

95. Mattox, T. M. *et al.* Chemical Control of Plasmons in Metal Chalcogenide and Metal Oxide Nanostructures. *Adv. Mater.* **27**, 5830–5837 (2015).

96. Garcia, G. *et al.* Dynamically Modulating the Surface Plasmon Resonance of Doped Semiconductor Nanocrystals. *Nano Lett.* **11**, 4415–4420 (2011).

97. Feigenbaum, E., Diest, K. & Atwater, H. A. Unity-Order Index Change in Transparent Conducting Oxides at Visible Frequencies. *Nano Lett.* **10**, 2111–2116 (2010).

98. Haase, M., Weller, H. & Henglein, A. Photochemistry and Radiation Chemistry of Colloidal Semiconductors. 23. Electron Storage on ZnO Patricles and Size Quantization. *J. Phys. Chem.* **92**, 482–487 (1988).

99. Schrauben, J. N. *et al.* Titanium and zinc oxide nanoparticles are proton-coupled electron transfer agents. *Science (80-.).* **336**, 1298–1301 (2012).

100. Joost, U. *et al.* Reversible Photodoping of TiO2 Nanoparticles for Photochromic Applications. *Chem. Mater.* **30**, 8968–8974 (2018).

101. Schneider, J. & Bahnemann, D. W. Undesired Role of Sacrificial Reagents in Photocatalysis. *J. Phys. Chem. Lett.* **4**, 3479–3483 (2013).

102. Chen, X., Shen, S., Guo, L. & Mao, S. S. Semiconductor-based Photocatalytic Hydrogen Generation. *Chem. Rev.* **110**, 6503–6570 (2010).

103. Carroll, G. M., Schimpf, A. M., Tsui, E. Y. & Gamelin, D. R. Redox Potentials of Colloidal n-Type ZnO Nanocrystals: Effects of Confinement, Electron Density, and Fermi-Level Pinning by Aldehyde Hydrogenation. *J. Am. Chem. Soc.* **137**, 11163–11169 (2015).

104. Chen, J., Ollis, D. F., Rulkens, W. H. & Bruning, H. Photocatalyzed oxidation of alcohols and organochlorides in the presence of native TiO2 and metallized TiO2 suspensions. Part (I): photocatalytic activity and pH influence. *Water Res.* **33**, 661–668 (1999).

105. Wang, C., Rabani, J., Bahnemann, D. W. & Dohrmann, J. K. Photonic efficiency and quantum yield of formaldehyde formation from methanol in the presence of various TiO2 photocatalysts. *J. Photochem. Photobiol. A Chem.* **148**, 169–176 (2002).

106. Schimpf, A. M., Knowles, K. E., Carroll, G. M. & Gamelin, D. R. Electronic Doping and Redox-Potential Tuning in Colloidal Semiconductor Nanocrystals. *Acc. Chem. Res.* **48**, 1929–1937 (2015).

107. Liu, W. K. *et al.* Room-Temperature Electron Spin Dynamics in Free-Standing ZnO Quantum Dots. *Phys. Rev. Lett.* **98**, 186804 (2007).

108. Brozek, C. K., Hartstein, K. H. & Gamelin, D. R. Potentiometric Titrations for Measuring the Capacitance of Colloidal Photodoped ZnO Nanocrystals. *J. Am. Chem. Soc.* **138**, 10605–10610 (2016).

109. Scanlon, M. D., Peljo, P., Méndez, M. A., Smirnov, E. & Girault, H. H. Charging and discharging at the nanoscale: Fermi level equilibration of metallic nanoparticles. *Chem. Sci.* **6**, 2705–2720 (2015).

110. Bueno, P. R. Nanoscale origins of super-capacitance phenomena. *J. Power Sources* **414**, 420–434 (2019).

111. González, A., Goikolea, E., Barrena, J. A. & Mysyk, R. Review on supercapacitors: Technologies and materials. *Renew. Sustain. Energy Rev.* **58**, 1189–1206 (2016).

112. Sawangphruk, M. *et al.* High-performance supercapacitors based on silver nanoparticle–polyaniline–graphene nanocomposites coated on flexible carbon fiber paper. *J. Mater. Chem. A* **1**, 9630–9636 (2013).

113. Wang, G., Zhang, L. & Zhang, J. A review of electrode materials for electrochemical supercapacitors. *Chem. Soc. Rev.* **41**, 797–828 (2012).

114. Zhang, Y. *et al.* Progress of electrochemical capacitor electrode materials: A review. *Int. J. Hydrogen Energy* **34**, 4889–4899 (2009).

115. Sudhakar, Y. N., Selvakumar, M. & Bhat, D. K. Chapter 3 - Biopolymer Electrolyte for Supercapacitor. in (eds. Sudhakar, Y. N., Selvakumar, M. & Bhat, D. K. B. T.-B. E.) 53–116 (Elsevier, 2018). doi:https://doi.org/10.1016/B978-0-12-813447-4.00003-0.

116. Srinivasan, S. *Fuel Cells: From Fundamentals to Applications*. (Springer Science & Business Media, 2006).

117. Frackowiak, E. & Béguin, F. Carbon materials for the electrochemical storage of energy in capacitors. *Carbon N. Y.* **39**, 937–950 (2001).

118. Frackowiak, E., Jurewicz, K., Delpeux, S. & Béguin, F. Nanotubular materials for supercapacitors. *J. Power Sources* **97**–**98**, 822–825 (2001).

119. Ochsenbein, S. T. *et al.* Charge-controlled magnetism in colloidal doped semiconductor nanocrystals. *Nat. Nanotechnol.* **4**, 681–687 (2009).

120. Zhou, D. & Kittilstved, K. R. Electron trapping on Fe3+ sites in photodoped ZnO colloidal nanocrystals. *Chem. Commun.* **52**, 9101–9104 (2016).

121. Wang, J. *et al.* Spin blockade and phonon bottleneck for hot electron relaxation observed in n-doped colloidal quantum dots. *Nat. Commun.* **12**, 550 (2021).

122. Whitaker, K. M. *et al.* Hyperfine coupling in colloidal n-type ZnO quantum dots: Effects on electron spin relaxation. *J. Phys. Chem. C* **114**, 14467–14472 (2010).

123. Kriegel, I. *et al.* Tuning the Excitonic and Plasmonic Properties of Copper Chalcogenide Nanocrystals. *J. Am. Chem. Soc.* **134**, 1583–1590 (2012).

124. Agrawal, A. *et al.* Localized Surface Plasmon Resonance in Semiconductor Nanocrystals. *Chem. Rev.* **118**, 3121–3207 (2018).

125. Liu, X. & Swihart, M. T. Heavily-doped colloidal semiconductor and metal oxide nanocrystals: An emerging new class of plasmonic nanomaterials. *Chem. Soc. Rev.* **43**, 3908–3920 (2014).

126. Plummer, L. K. *et al.* Influence of Monomer Flux and Temperature on Morphology of Indium Oxide Nanocrystals during a Continuous Growth Synthesis. *Chem. Mater.* **31**, 7638–7649 (2019).

127. Hamberg, I., Granqvist, C. G., Berggren, K.-F., Sernelius, B. E. & Engström, L. Band-gap widening in heavily Sn-doped In203. *Phys. Rev. B - Condens. Matter Mater. Phys.* **30**, (1984).

128. Saleh, N. B. *et al.* Importance of doping, dopant distribution, and defects on electronic band structure alteration of metal oxide nanoparticles: Implications for reactive oxygen species. *Sci. Total Environ.* **568**, 926–932 (2016).

129. Morfa, A. J., Macdonald, B. I., Subbiah, J. & Jasieniak, J. J. Understanding the chemical origin of improved thin-film device performance from photodoped ZnO nanoparticles. *Sol. Energy Mater. Sol. Cells* **124**, 211–216 (2014).

130. Peper, J. L. & Mayer, J. M. Manifesto on the thermochemistry of nanoscale redox reactions for energy conversion. *ACS Energy Lett.* **4**, 866–872 (2019).

131. Schimpf, A. M., Ochsenbein, S. T., Buonsanti, R., Milliron, D. J. & Gamelin, D. R. Comparison of extra electrons in colloidal n-type Al3+-doped and photochemically reduced ZnO nanocrystals. *Chem. Commun.* **48**, 9352–9354 (2012).

132. Mendelsberg, R. J. *et al.* Dispersible Plasmonic Doped Metal Oxide Nanocrystal Sensors that Optically Track Redox Reactions in Aqueous Media with Single-Electron Sensitivity. *Adv. Opt. Mater.* **3**, 1293–1300 (2015).

133. Castro Neto, A. H., Guinea, F., Peres, N. M. R., Novoselov, K. S. & Geim, A. K. The electronic properties of graphene. *Rev. Mod. Phys.* **81**, 109–162 (2009).

134. Fang, L. *et al.* Disassembling 2D van der Waals crystals into macroscopic monolayers and reassembling into artificial lattices. *Science (80-.).* **367**, 903–906 (2020).

135. Hills, R. D. Y. *et al.* From Graphene and Topological Insulators to Weyl Semimetals. in *Symmetry, Spin Dynamics and the Properties of Nanostructures* 277–315 (WORLD

SCIENTIFIC, 2015). doi:10.1142/9789814740371_0012.

136. Sarkar, J. & Bhattacharyya, S. Application of graphene and graphene-based materials in clean energy-related devices Minghui. *Arch. Thermodyn.* **33**, 23–40 (2012).

137. Carr, S. *et al.* Twistronics: Manipulating the electronic properties of two-dimensional layered structures through their twist angle. *Phys. Rev. B* **95**, 75420 (2017).

138. Cao, Y. *et al.* Unconventional superconductivity in magic-angle graphene superlattices. *Nature* **556**, 43–50 (2018).

139. Mak, K. F. *et al.* Tightly bound trions in monolayer MoS2. *Nat. Mater.* **12**, 207–211 (2013).

140. Radisavljevic, B., Radenovic, A., Brivio, J., Giacometti, V. & Kis, A. Single-layer MoS2 transistors. *Nat. Nanotechnol.* **6**, 147–150 (2011).

141. Basov, D. N., Averitt, R. D. & Hsieh, D. Towards properties on demand in quantum materials. *Nat. Mater.* **16**, 1077–1088 (2017).

142. Bao, W. *et al.* Visualizing nanoscale excitonic relaxation properties of disordered edges and grain boundaries in monolayer molybdenum disulfide. *Nat. Commun.* **6**, 7993 (2015).

143. Borys, N. J. *et al.* Anomalous Above-Gap Photoexcitations and Optical Signatures of Localized Charge Puddles in Monolayer Molybdenum Disulfide. *ACS Nano* **11**, 2115–2123 (2017).

144. Castellanos-Gomez, A. *et al.* Local Strain Engineering in Atomically Thin MoS2. *Nano Lett.* **13**, 5361–5366 (2013).

145. Liu, Z. *et al.* Strain and structure heterogeneity in MoS2 atomic layers grown by chemical vapour deposition. *Nat. Commun.* **5**, 5246 (2014).

146. Mouri, S., Miyauchi, Y. & Matsuda, K. Tunable Photoluminescence of Monolayer MoS2 via Chemical Doping. *Nano Lett.* **13**, 5944–5948 (2013).

147. Amani, M. *et al.* Near-unity photoluminescence quantum yield in MoS_2. *Science* **350**, 1065–1068 (2015).

148. Mitterreiter, E. *et al.* Atomistic Positioning of Defects in Helium Ion Treated Single-Layer MoS2. *Nano Lett.* **20**, 4437–4444 (2020).

149. Kastl, C. *et al.* Multimodal spectromicroscopy of monolayer WS2 enabled by ultra-clean van der Waals epitaxy. *2D Mater.* **5**, 45010 (2018).

150. Carozo, V. *et al.* Optical identification of sulfur vacancies: Bound excitons at the edges of monolayer tungsten disulfide. *Sci. Adv.* **3**, e1602813 (2017).

151. Chhowalla, M. *et al.* The chemistry of two-dimensional layered transition metal dichalcogenide nanosheets. *Nat. Chem.* **5**, 263–275 (2013).

152. Lee, C.-H. *et al.* Tungsten Ditelluride: a layered semimetal. *Sci. Rep.* **5**, 10013 (2015).

153. Wang, G. *et al.* Colloquium: Excitons in atomically thin transition metal dichalcogenides. *Rev. Mod. Phys.* **90**, 21001 (2018).

154. Lin, Z. *et al.* 2D materials advances: from large scale synthesis and controlled heterostructures to improved characterization techniques, defects and applications. *2D Mater.* **3**, 42001 (2016).

155. Zeng, Q. & Liu, Z. Novel Optoelectronic Devices: Transition-Metal-Dichalcogenide-Based 2D Heterostructures. *Adv. Electron. Mater.* **4**, 1700335 (2018).

156. Berkelbach, T. C. & Reichman, D. R. Optical and Excitonic Properties of Atomically Thin Transition-Metal Dichalcogenides. *Annu. Rev. Condens. Matter Phys.* **9**, 379–396 (2018).

157. Choi, W. *et al.* Recent development of two-dimensional transition metal dichalcogenides and their applications. *Mater. Today* **20**, 116–130 (2017).

158. Mak, K. F., Lee, C., Hone, J., Shan, J. & Heinz, T. F. Atomically Thin MoS2: A New Direct-Gap Semiconductor. *Phys. Rev. Lett.* **105**, 136805 (2010).

159. Wang, Q. H., Kalantar-Zadeh, K., Kis, A., Coleman, J. N. & Strano, M. S. Electronics and optoelectronics of two-dimensional transition metal dichalcogenides. *Nat. Nanotechnol.* **7**, 699–712 (2012).

160. Bao, W., Cai, X., Kim, D., Sridhara, K. & Fuhrer, M. S. High mobility ambipolar MoS 2 field-effect transistors: Substrate and dielectric effects. *Appl. Phys. Lett.* **102**, 042104 (2013).

161. Islam, M. R. *et al.* Tuning the electrical property via defect engineering of single layer MoS 2 by oxygen plasma. *Nanoscale* **6**, 10033 (2014).

162. Choudhary, N. *et al.* Two-dimensional lateral heterojunction through bandgap engineering of MoS 2 via oxygen plasma. *J. Phys. Condens. Matter* **28**, 364002 (2016).

163. Cheiwchanchamnangij, T. & Lambrecht, W. R. L. Quasiparticle band structure calculation of monolayer, bilayer, and bulk MoS2. *Phys. Rev. B* **85**, 205302 (2012).

164. Scheuschner, N. *et al.* Photoluminescence of freestanding single- and few-layer MoS 2. *Phys. Rev. B - Condens. Matter Mater. Phys.* **89**, 2–7 (2014).

165. Fuhrer, M. S. & Hone, J. Measurement of mobility in dual-gated MoS2 transistors. *Nat. Nanotechnol.* **8**, 146–147 (2013).

166. Niu, Y. *et al.* Thickness-Dependent Differential Reflectance Spectra of Monolayer and Few-Layer MoS2, MoSe2, WS2 and WSe2. *Nanomaterials* **8**, (2018).

167. Li, Z. *et al.* Graphene Quantum Dots Doping of MoS2 Monolayers. *Adv. Mater.* **27**, 5235–5240 (2015).

168. Ross, J. S. *et al.* Electrical control of neutral and charged excitons in a monolayer

semiconductor. *Nat. Commun.* **4**, 1474 (2013).

169. Kümmell, T., Quitsch, W., Matthis, S., Litwin, T. & Bacher, G. Gate control of carrier distribution in k-space in MoS2 monolayer and bilayer crystals. *Phys. Rev. B* **91**, 125305 (2015).

170. Ross, J. S. *et al.* Electrically tunable excitonic light-emitting diodes based on monolayer WSe2 p–n junctions. *Nat. Nanotechnol.* **9**, 268–272 (2014).

171. Baugher, B. W. H., Churchill, H. O. H., Yang, Y. & Jarillo-Herrero, P. Optoelectronic devices based on electrically tunable p–n diodes in a monolayer dichalcogenide. *Nat. Nanotechnol.* **9**, 262–267 (2014).

172. Pospischil, A., Furchi, M. M. & Mueller, T. Solar-energy conversion and light emission in an atomic monolayer p–n diode. *Nat. Nanotechnol.* **9**, 257–261 (2014).

173. Feng, J., Qian, X., Huang, C. W. & Li, J. Strain-engineered artificial atom as a broad-spectrum solar energy funnel. *Nat. Photonics* **6**, 866–872 (2012).

174. van der Zande, A. & Hone, J. Inspired by strain. *Nat. Photonics* **6**, 804–806 (2012).

175. Gong, C. *et al.* Metal contacts on physical vapor deposited monolayer MoS2. *ACS Nano* **7**, 11350–11357 (2013).

176. Fang, H. & Hu, W. Photogating in Low Dimensional Photodetectors. *Adv. Sci.* **4**, 1700323 (2017).

177. Buscema, M. *et al.* Photocurrent generation with two-dimensional van der Waals semiconductors. *Chem. Soc. Rev.* **44**, 3691–3718 (2015).

178. Chernikov, A., Ruppert, C., Hill, H. M., Rigosi, A. F. & Heinz, T. F. Population inversion and giant bandgap renormalization in atomically thin WS2 layers. *Nat. Photonics* **9**, 466–470 (2015).

179. Wang, K. *et al.* Strain tolerance of two-dimensional crystal growth on curved surfaces. *Sci. Adv.* **5**, eaav4028 (2019).

180. Lui, C. H. *et al.* Trion-Induced Negative Photoconductivity in Monolayer MoS2. *Phys. Rev. Lett.* **113**, 166801 (2014).

181. Li, J. *et al.* Tuning the optical emission of MoS2 nanosheets using proximal photoswitchable azobenzene molecules. *Appl. Phys. Lett.* **105**, 241116 (2014).

182. Liu, H. F., Wong, S. L. & Chi, D. Z. CVD Growth of MoS2-based Two-dimensional Materials. *Chem. Vap. Depos.* **21**, 241–259 (2015).

183. Kaasbjerg, K., Thygesen, K. S. & Jacobsen, K. W. Phonon-limited mobility in n-type single-layer MoS2 from first principles. *Phys. Rev. B* **85**, 115317 (2012).

184. Liao, L. *et al.* Theoretical study on the photodoping effects in La 1- x Sr x MnO 3 /SrNb y Ti 1- y O 3 p-n heterojunction. *Phys. status solidi* **206**, 1655–1659 (2009).

185. Kossacki, P. Optical studies of charged excitons in II~VI semiconductor quantum wells. *J. Phys. Condens. Matter* **15**, R471--R493 (2003).

186. Siviniant, J., Scalbert, D., Kavokin, A. V, Coquillat, D. & Lascaray, J.-P. Chemical equilibrium between excitons, electrons, and negatively charged excitons in semiconductor quantum wells. *Phys. Rev. B* **59**, 1602–1604 (1999).

187. Gibbs, S. L. *et al.* Dual-Mode Infrared Absorption by Segregating Dopants within Plasmonic Semiconductor Nanocrystals. *Nano Lett.* **20**, 7498–7505 (2020).

188. Liu, W. K., Whitaker, K. M., Kittilstved, K. R. & Gamelin, D. R. Stable Photogenerated Carriers in Magnetic Semiconductor Nanocrystals. *J. Am. Chem. Soc.* **128**, 3910–3911 (2006).

189. Carroll, G. M., Brozek, C. K., Hartstein, K. H., Tsui, E. Y. & Gamelin, D. R. Potentiometric Measurements of Semiconductor Nanocrystal Redox Potentials. *J. Am. Chem. Soc.* **138**, 4310–4313 (2016).

190. Luther, J. M., Jain, P. K., Ewers, T. & Alivisatos, A. P. Localized surface plasmon resonances arising from free carriers in doped quantum dots. *Nat. Mater.* **10**, 361–366 (2011).

191. Kanehara, M., Koike, H., Yoshinaga, T. & Teranishi, T. Indium tin oxide nanoparticles with compositionally tunable surface plasmon resonance frequencies in the near-IR region. *J. Am. Chem. Soc.* **131**, 17736–17737 (2009).

192. Van Dijken, A., Meulenkamp, E. A., Vanmaekelbergh, D. & Meijerink, A. Influence of Adsorbed Oxygen on the Emission Properties of Nanocrystalline ZnO Particles. *J. Phys. Chem. B* **104**, 4355–4360 (2000).

193. Wuister, S. F., De Mello Donegá, C. & Meijerink, A. Influence of thiol capping on the exciton luminescence and decay kinetics of CdTe and CdSe quantum dots. *J. Phys. Chem. B* **108**, 17393–17397 (2004).

194. Zhang, J. J., Cheng, F. F., Li, J. J., Zhu, J. J. & Lu, Y. Fluorescent nanoprobes for sensing and imaging of metal ions: Recent advances and future perspectives. *Nano Today* **11**, 309–329 (2016).

195. Morris-Cohen, A. J., Frederick, M. T., Lilly, G. D., McArthur, E. A. & Weiss, E. A. Organic surfactant-controlled composition of the surfaces of CdSe quantum dots. *J. Phys. Chem. Lett.* **1**, 1078–1081 (2010).

196. Cohn, A. W., Schimpf, A. M., Gunthardt, C. E. & Gamelin, D. R. Size-dependent trap-assisted auger recombination in semiconductor nanocrystals. *Nano Lett.* **13**, 1810–1815 (2013).

197. Kriegel, I. *et al.* Ultrafast Photodoping and Plasmon Dynamics in Fluorine-Indium Codoped Cadmium Oxide Nanocrystals for All-Optical Signal Manipulation at Optical Communication Wavelengths. *J. Phys. Chem. Lett.* **7**, 3873–3881 (2016).

198. Rinehart, J. D., Schimpf, A. M., Weaver, A. L., Cohn, A. W. & Gamelin, D. R. Photochemical electronic doping of colloidal CdSe nanocrystals. *J. Am. Chem. Soc.* **135**, 18782–18785 (2013).

199. Gao, M. *et al.* Lithium metal batteries for high energy density: Fundamental electrochemistry and challenges. *J. Energy Chem.* **59**, 666–687 (2021).

200. Chen, R., Luo, R., Huang, Y., Wu, F. & Li, L. Advanced High Energy Density Secondary Batteries with Multi-Electron Reaction Materials. *Adv. Sci.* **3**, 1600051 (2016).

201. Pannwitz, A. & Wenger, O. S. Proton-coupled multi-electron transfer and its relevance for artificial photosynthesis and photoredox catalysis. *Chem. Commun.* **55**, 4004–4014 (2019).

202. Koper, M. T. M. Thermodynamic theory of multi-electron transfer reactions: Implications for electrocatalysis. *J. Electroanal. Chem.* **660**, 254–260 (2011).

203. Kim, Y., Smith, J. G. & Jain, P. K. Harvesting multiple electron–hole pairs generated through plasmonic excitation of Au nanoparticles. *Nat. Chem.* **10**, 763–769 (2018).

204. Yu, S., Wilson, A. J., Heo, J. & Jain, P. K. Plasmonic Control of Multi-Electron Transfer and C–C Coupling in Visible-Light-Driven CO2 Reduction on Au Nanoparticles. *Nano Lett.* **18**, 2189–2194 (2018).

205. Knowles, K. E., Malicki, M., Parameswaran, R., Cass, L. C. & Weiss, E. A. Spontaneous Multielectron Transfer from the Surfaces of PbS Quantum Dots to Tetracyanoquinodimethane. *J. Am. Chem. Soc.* **135**, 7264–7271 (2013).

206. Castillo-Lora, J., Delley, M. F., Laga, S. M. & Mayer, J. M. Two-Electron–Two-Proton Transfer from Colloidal ZnO and TiO2 Nanoparticles to Molecular Substrates. *J. Phys. Chem. Lett.* **11**, 7687–7691 (2020).

207. Jawad, A. H., Mubarak, N. S. A., Ishak, M. A. M., Ismail, K. & Nawawi, W. I. Kinetics of photocatalytic decolourization of cationic dye using porous TiO2 film. *J. Taibah Univ. Sci.* **10**, 352–362 (2016).

208. Robert, D. Photosensitization of TiO2 by MxOy and MxSy nanoparticles for heterogeneous photocatalysis applications. *Catal. Today* **122**, 20–26 (2007).

209. Tyagi, P., Tuli, S. & Srivastava, R. Study of fluorescence quenching due to 2 , 3 , 5 , diffusion analysis using photoluminescence spectroscopy. *J. Chem. Phys.* **142**, 1–9 (2015).

210. Yu, Z. *et al.* High-efficiency perovskite solar cells employing a conjugated donor-acceptor co-polymer as a hole-transporting material. *RSC Adv.* **7**, 27189–27197 (2017).

211. Kiefer, D. *et al.* Double doping of conjugated polymers with monomer molecular dopants. *Nat. Mater.* **18**, 149–155 (2019).

212. Panja, S. *et al.* Dianions of 7,7,8,8-tetracyano-p-quinodimethane and perfluorinated tetracyanoquinodimethane: Information on excited states from lifetime measurements in an electrostatic storage ring and optical absorption spectroscopy. *J. Chem. Phys.* **127**, 1–7 (2007).

213. Kroon, R. *et al.* Polar Side Chains Enhance Processability, Electrical Conductivity, and Thermal Stability of a Molecularly p-Doped Polythiophene. *Adv. Mater.* **29**, 1–7 (2017).

214. Lüssem, B. Beyond 100% doping efficiency. *Nat. Mater.* **18**, 93–94 (2019).

215. Goings, J. J. *et al.* Theoretical characterization of conduction-band electrons in photodoped and Aluminum-Doped Zinc Oxide (AZO) quantum dots. *J. Phys. Chem. C* **118**, 26584–26590 (2014).

216. Theurer, C. P. *et al.* Photophysics of Charge Transfer Complexes Formed by Tetracene and Strong Acceptors. *J. Phys. Chem. C* **125**, 6313–6323 (2021).

217. Stanfield, D. A., Wu, Y., Tolbert, S. H. & Schwartz, B. J. Controlling the Formation of Charge Transfer Complexes in Chemically Doped Semiconducting Polymers. *Chem. Mater.* **33**, 2343–2356 (2021).

218. Ma, L. *et al.* Single photon triggered dianion formation in TCNQ and F 4 TCNQ crystals. *Sci. Rep.* **6**, 1–7 (2016).

219. Faulques, E. *et al.* Monomer, dimer, and tetramer states in molybdenum complexes of tetracyanoquinodimethane. *J. Phys. Chem. B* **101**, 1561–1568 (1997).

220. Yao, K. *et al.* Optically Discriminating Carrier-Induced Quasiparticle Band Gap and Exciton Energy Renormalization in Monolayer MoS2. *Phys. Rev. Lett.* **119**, 87401 (2017).

221. Chernikov, A. *et al.* Electrical Tuning of Exciton Binding Energies in Monolayer WS2. *Phys. Rev. Lett.* **115**, 126802 (2015).

222. Kastl, C. *et al.* The important role of water in growth of monolayer transition metal dichalcogenides. *2D Mater.* **4**, 21024 (2017).

223. van der Zande, A. M. *et al.* Grains and grain boundaries in highly crystalline monolayer molybdenum disulphide. *Nat. Mater.* **12**, 554–561 (2013).

224. Kastl, C. *et al.* Effects of Defects on Band Structure and Excitons in WS2 Revealed by Nanoscale Photoemission Spectroscopy. *ACS Nano* **13**, 1284–1291 (2019).

225. Smithe, K. K. H., English, C. D., Suryavanshi, S. V. & Pop, E. Intrinsic electrical transport and performance projections of synthetic monolayer MoS2 devices. *2D Mater.* **4**, 0–19 (2017).

226. Jariwala, D. *et al.* Band-like transport in high mobility unencapsulated single-layer MoS2 transistors. *Appl. Phys. Lett.* **102**, 173107 (2013).

227. Salihoglu, O., Kakenov, N., Balci, O., Balci, S. & Kocabas, C. Graphene-Quantum Dot Hybrid Optoelectronics at Visible Wavelengths. *ACS Photonics* **5**, 2384–2390 (2018).

228. Goodman, A. J., Dahod, N. S. & Tisdale, W. A. Ultrafast Charge Transfer at a Quantum Dot/2D Materials Interface Probed by Second Harmonic Generation. *J. Phys. Chem. Lett.* **9**, 4227–4232 (2018).

229. Raja, A. *et al.* Energy Transfer from Quantum Dots to Graphene and MoS2: The Role of Absorption and Screening in Two-Dimensional Materials. *Nano Lett.* **16**, 2328–2333 (2016).

230. Cheng, Y. & Liu, J. Carbon Nanomaterials for Flexible Energy Storage. *Mater. Res. Lett.* **1**, 175–192 (2013).

231. Gandhi, K. S. Storage of Electrical Energy. *Indian Chem. Eng.* **52**, 57–75 (2010).

232. Liu, C., Li, F., Ma, L.-P. & Cheng, H.-M. Advanced Materials for Energy Storage. *Adv. Mater.* **22**, (2010).

233. Koohi-Fayegh, S. & Rosen, M. A. A review of energy storage types, applications and recent developments. *J. Energy Storage* **27**, 101047 (2020).

234. Evans, A., Strezov, V. & Evans, T. J. Assessment of utility energy storage options for increased renewable energy penetration. *Renew. Sustain. Energy Rev.* **16**, 4141–4147 (2012).

235. Tarascon, J.-M. Key challenges in future Li-battery research. *Philos. Trans. R. Soc. A Math. Phys. Eng. Sci.* **368**, 3227–3241 (2010).

236. Gogotsi, Y. & Simon, P. True Performance Metrics in Electrochemical Energy Storage. *Science (80-.).* **334**, 917–918 (2011).

237. Chen, H. *et al.* Progress in electrical energy storage system: A critical review. *Prog. Nat. Sci.* **19**, 291–312 (2009).

238. Wang, W. *et al.* Recent progress in redox flow battery research and development. *Adv. Funct. Mater.* **23**, 970–986 (2013).

239. Sabihuddin, S., Kiprakis, A. E. & Mueller, M. A Numerical and Graphical Review of Energy Storage Technologies. 46 (2015).

240. Huang, Y.-X., Wu, F. & Chen, R.-J. Thermodynamic analysis and kinetic optimization of high-energy batteries based on multi-electron reactions. *Natl. Sci. Rev.* **7**, 1367–1386 (2020).

241. Bellani, S. *et al.* ITO nanoparticles break optical transparency/high-areal capacitance trade-off for advanced aqueous supercapacitors. *J. Mater. Chem. A* **5**, 25177–25186 (2017).

242. Li, W., Fu, H.-C., Zhao, Y., He, J.-H. & Jin, S. 14.1% Efficient Monolithically Integrated Solar Flow Battery. *Chem* **4**, 2644–2657 (2018).

243. Acarón Ledesma, H. *et al.* An atlas of nano-enabled neural interfaces. *Nat. Nanotechnol.* **14**, 645–657 (2019).

244. Gao, X. D., Fei, G. T., Zhang, Y., Zhang, L. De & Hu, Z. M. All-Optical-Input Transistors: Light-Controlled Enhancement of Plasmon-Induced Photocurrent. *Adv. Funct. Mater.* **28**, 1–8 (2018).

245. Palomaki, P. K. B., Miller, E. M. & Neale, N. R. Control of Plasmonic and Interband Transitions in Colloidal Indium Nitride Nanocrystals. *J. Am. Chem. Soc.* **135**, 14142–14150 (2013).

246. Chen, Y., Landes, N. T., Little, D. J. & Beaulac, R. Conversion Mechanism of Soluble

Alkylamide Precursors for the Synthesis of Colloidal Nitride Nanomaterials. *J. Am. Chem. Soc.* **140**, 10421–10424 (2018).

247. Marin, B. C. *et al.* Plasmon-Enhanced Two-Photon Absorption in Photoluminescent Semiconductor Nanocrystals. *ACS Photonics* **3**, 526–531 (2016).

248. Dixon, S. C., Scanlon, D. O., Carmalt, C. J. & Parkin, I. P. n-Type doped transparent conducting binary oxides: an overview. *J. Mater. Chem. C* **4**, 6946–6961 (2016).

249. Thirumoorthi, M. & Thomas Joseph Prakash, J. Structure, optical and electrical properties of indium tin oxide ultra thin films prepared by jet nebulizer spray pyrolysis technique. *J. Asian Ceram. Soc.* **4**, 124–132 (2016).

250. Li, Y., Bu, Y., Liu, Q., Zhang, X. & Xu, J. High photocatalytic activities of zinc oxide nanotube arrays modified with tungsten trioxide nanoparticles. *Chinese J. Catal.* **39**, 54–62 (2018).

251. Geva, N., Shepherd, J. J., Nienhaus, L., Bawendi, M. G. & Voorhis, T. Van. Morphology of Passivating Organic Ligands around a Nanocrystal. *J. Phys. Chem. C* (2018).

252. Minami, T., Miyata, T. & Yamamoto, T. Work function of transparent conducting multicomponent oxide thin films prepared by magnetron sputtering. *Surf. Coatings Technol.* **108**–**109**, 583–587 (1998).

253. Kang, J., Tongay, S., Zhou, J., Li, J. & Wu, J. Band offsets and heterostructures of two-dimensional semiconductors. *Appl. Phys. Lett.* **102**, 12111 (2013).

XII. Acknowledgements

This PhD thesis would have not been possible without the priceless support of many scientists, colleagues, and friends who accompanied me on this journey. I am deeply grateful to all of them. I take this opportunity to acknowledge and say thank you once again to:

Dr. Ilka Kriegel (IIT), my supervisor and the Principal Investigator of the Functional nanosystems group, who guided and motivated me during every stage of my PhD with energy, wisdom, and kindness. I was fortunate enough to be able to learn from an extraordinarily talented and creative scientist, who truly believed in this research project, shared with me profound academic knowledge, and supported me to pursue countless opportunities. I am most grateful to her, both on a professional and personal level, for the unwavering trust she granted me, the endless scientific conversations, her unique approach and the multiple lessons she taught me by her example and that will significantly influence me in my future career.

Prof. Liberato Manna (IIT), my supervisor and the Head of the Nanochemistry Department. I would like to express my special thanks to him for his unfailing support and his patience, as well as for the invaluable advice and insights he continuously provided during these three years of doctoral research. I had the privilege to work in his modern and well-equipped lab on a daily basis and I was honored to be part of the scientific environment he created, sharing his extraordinarily vast expertise in chemistry and materials science.

Prof. Francesco Buatier De Mongeot (University of Genova), my supervisor from the University of Genova, for his guidance and encouragement to pursue meaningful scientific results for my doctoral thesis. I would like to extend my sincere appreciation to him for his kindness, his suggestions, and for granting me the scientific freedom to follow research ideas both within Italy and abroad, which was particularly important for my scientific plans.

Prof. P. James Schuck (Columbia University), who hosted me in his research group at Columbia University in 2019. I would like to express my genuine gratitude to him and to all his research group for making this unique opportunity possible, allowing me to investigate 2D materials with cutting-edge spectroscopy techniques. This experience abroad had a significant impact on my academic and personal development. Many thanks also for the aperitivi we had in Milan and New York, and for the friendly and generous support he always demonstrated.

The *Functional Nanosystems group*, who have been my closest colleagues and companions in this adventure. I started my PhD being the only member of Dr. Kriegel's research group and I am concluding it as part of a flourishing team, I am sure they will achieve incredible results and I wish them the best for their future. Many thanks to Nicola Curreli, Andrea Camellini, Andrea Rubino, Aswin Asaithambi, Nicolò Petrini, Luca Rebecchi, Nastaran Tofighi, and the new entries Ivet Albo, Anjana Muraleedharan. In particular, I would like to express my deepest gratitude to Nicola, over the last 2 years we have worked tirelessly side by side as colleagues and friends on many projects and most of what I have achieved would have not been possible without his brilliant contributions and motivation. A special thank also to Nicolò for his kindness and the endless hours spent on simulations, Luca for synthesizing liters of NCs, Aswin for his insights on the review, and to Andrea R. and Andrea C. for their bright ideas and the analysis of titration data.

The *Nanochemistry group*, the lab technicians for their extremely precious support, and all IIT researchers who embarked on collaborative projects with me. From the first day, I was welcomed in a friendly environment, their enthusiasm, curiosity, and sincere willingness to help and work together significantly improved my experience in IIT. I want to express my gratitude to Baowei Zhang, Gabriele Bianca, Marilena Zappia, Mengjiao Wang, Angela Melcherts. Many thanks to Mirko Prato for the analysis of XPS data, Luca De Trizio for his suggestions on MO NCs, Dmitry Baranov for the support during the beginning of my PhD.

The *Schuck research group*, and *all scientists* I had the opportunity to work with. I am particularly thankful to Emanuil Sashev Yanev (Columbia University) for his help with nanofabrication techniques, to Chiara Trovatello (Politecnico di Milano) and Michele Guizzardi (Politecnico di Milano) for their knowledge and expertise on ultrafast spectroscopy. Special thanks to Prof. Alessandro Fanti (University of Cagliari) and Matteo B. Lodi (University of Cagliari) for the many hours spent working with COMSOL on numerical calculations.

Finally, many thanks to all my friends, from Genova, Forlì, from all over Europe and from many corners of this World. Thank you for our evenings together, for the beautiful hikes in Liguria, the swims in Bergeggi, and the endless and sometimes surreal conversations. Thanks to 'Middle Earth' and our 'Simposio' gatherings. I had a wonderful time in Genova during these years and if I managed to appreciate the beauty of these lands I owe it also to you. You helped me to become a better scientist and, I hope, a better person. Above all, thanks to those who decided to be close

to me regardless of the distance and thanks to my family and parents, for being a certainty in my life. Thank you for the guidance, for the invaluable help and constant love that I always felt. Grazie.